TYPE IA SUPERNOVAE: THEIR PROGENITORS AND USE AS COSMOLOGICAL PROBES

By

BRANDON PATEL

A dissertation submitted to the

Graduate School–New Brunswick

Rutgers, The State University of New Jersey

In partial fulfillment of the requirements

For the degree of

Doctor of Philosophy

Graduate Program in Physics and Astronomy

Written under the direction of

Dr. Saurabh W. Jha

And approved by

_____

_____

_____

_____

_____

New Brunswick, New Jersey

May, 2015

ABSTRACT OF THE DISSERTATION

Type Ia Supernovae: Their Progenitors and Use as Cosmological Probes

By BRANDON PATEL

Dissertation Director:

Dr. Saurabh W. Jha

Type Ia supernovae (SNe Ia) are important cosmological probes, but we are uncertain how they explode. There are two progenitor channels for SNe Ia: single and double degenerate white dwarf (WD) systems. In either model, we expect the system to be detectable as a Supersoft X-ray Source (SSS) for a significant amount of time before the explosion. By studying these SSSs, we hope to improve our understanding of SNe Ia. In Chapter 2, we analyze an interesting source (r1-25) in M31. We found that the source exhibited spectral changes to harder X-ray states. r1-25 is the first source of its kind, and we require unique physical models to fit its behavior. We find that existing WD models are inconsistent with the spectra of the source. We explore new black hole and neutron star models, and find that they can model the unusual behavior of r1-25.

In Chapter 3, we study three gravitationally lensed SNe from the Cluster Lensing And Supernova survey with Hubble (CLASH). Based on photometric classification, we found that two SNe (SN CLO12Car and CLN12Did) are likely to be SNe Ia, while the classification of the third is inconclusive. Using multi-color light-curve fits to determine a standardized

SN Ia luminosity distance, we infer that SN CLO12Car was $\sim 1.0 \pm 0.2$ mag brighter than field SNe Ia at a similar redshift and ascribe this to gravitational lens magnification. Similarly, SN CLN12Did is $\sim 0.2 \pm 0.2$ mag brighter than field SNe Ia. From independent CLASH strong+weak lensing maps of the clusters , we derived similar magnifications for the two SNe Ia. The two SNe Ia provide a new test of the cluster lens model predictions: we find that the magnifications based on the SN Ia brightness and those predicted by the lens maps are consistent.

Finally, in Chapter 4 we discuss a new light curve fitter for SNe Ia, which we call Multi-color Light Curve Shapes 3 (MLCS3). The project has not been completed, but we discuss some of the features, and the expected improvements from MLCS3 in the chapter. With nearly 1000 SNe Ia usable for cosmology, we are currently systematics, not statistics, limited for constraining cosmology. MLCS3 will provide more accurate distance measurements for the SNe Ia using a variety of improvements that have been suggested in the literature.

Acknowledgments

I would like the thank my adviser, Dr. Saurabh W. Jha, for all of his support during my time at Rutgers. He has provided me with GA funding for nearly my entire graduate career. Additionally, he provided me the opportunity to work on the project of my dreams: discovering and studying very distant Type Ia Supernovae. He has been a fantastic mentor and a true pleasure to work with.

I would like to thank all of my collaborators, at Rutgers and other institutions, who have helped me during my time at as a graduate student. I had the pleasure of working with three large collaborations, which has been instrumental in my thesis. Specifically, I would like to thank those I worked closely with; Curtis McCully, Steve Rodney, and Or Graur. We made many scientific discoveries together, and I am grateful for the opportunity to work with them. I would like to thank the students who worked with me as undergraduate researchers: Samia Bouzid, Tom Holoien, Viraj Pandya, and Yssavo Camacho.

I would also like to thank my thesis committee; Rachel Somerville, Terry Matilsky, Eva Andrei, and Adam Riess for their guidance and support.

I would like to thank the Rutgers astronomy group. The department has fostered a professional, but friendly working environment. I have found the graduate astronomy classes to be very informative, and the professors very approachable. I enjoyed working with my fellow graduate students through many difficult and thought provoking homework assignments.

Most of my thesis is published or will be published in the near future. Chapter 2 has been accepted by ApJ and is posted at Patel et al. (2013). Chapter 3 has been accepted by ApJ and is posted at Patel et al. (2014). Much of Chapter 4 is still in preparation, but it does include some published work (Jones et al. 2013; Rodney et al. 2012). I would like

to thank my collaborators on these works: Rosanne Di Stefano, Thomas Nelson, Francis A. Primini, Jifeng Liu, Sarah Scoles, Curtis McCully, Saurabh W. Jha, Steven A. Rodney, David O. Jones, Or Graur, Julian Merten, Adi Zitrin, Adam G. Riess, Thomas Matheson, Masao Sako, Thomas W.-S. Holoien, Marc Postman, Dan Coe, Matthias Bartelmann, Italo Balestra, Narciso Benítez, Rychard Bouwens, Larry Bradley, Tom Broadhurst, S. Bradley Cenko, Megan Donahue, Alexei V. Filippenko, Holland Ford, Peter Garnavich, Claudio Grillo, Leopoldo Infante, Stéphanie Jouvel Daniel Kelson, Anton Koekemoer, Ofer Lahav, Doron Lemze, Dan Maoz, Elinor Medezinski, Peter Melchior, Massimo Meneghetti, Alberto Molino, John Moustakas, Leonidas A. Moustakas, Mario Nonino, Piero Rosati, Stella Seitz, Louis G. Strolger, Keiichi Umetsu, Wei Zheng, and Daniel, Scolnic.

This work has been primarily supported through National Science Foundation (NSF) CAREER award AST-0847157 and NASA Keck PI Data Awards, administered by the NASA Exoplanet Science Institute.

Dedication

For George RR Martin, who has provided endless office conversation. Winter is here, but where is book six?

Table of Contents

List of Tables

List of Figures

Chapter 1

Introduction

Dark energy, which makes up ∼70% of the energy density of the Universe (Planck Collaboration et al. 2014), remains the biggest unsolved problem in astrophysics. Using SNe Ia to measure cosmological distances, two groups independently discovered the accelerated expansion of the Universe by dark energy, and were awarded the Nobel Prize in physics in 2011 (Riess et al. 1998; Perlmutter et al. 1999). Since the discovery, other astronomical observations have confirmed the existence of dark energy (e.g., Planck Collaboration et al. 2014, references therein). Despite our strong observational constraints, the physical nature of dark energy is still a mystery. SNe Ia continue to to be one of our best methods for studying this perplexing problem. This work will focus on the use of SNe Ia to measure cosmological distances.

1.1 Supernovae

SNe represent the explosion of stars. They can broadly be classified into two different types: core-collapse (CC) and thermonuclear (SNe Ia). CC SNe arise from the death of massive stars (with masses of $\sim 8M_{\odot}$ or larger, where $M_{\odot}$ is the mass of the Sun). The process differs slightly for each type of CC SN (see §1.1.3), but the general process is similar. The core of the massive star continues to fuse elements until it reaches iron. As iron is one of the most stable elements, fusing larger elements require endothermic reactions. The core, which can no longer balance the gravitational pressure, begins to collapse which leads to a SN. The remnant of the explosion is either a neutron star (NS, for initial masses of 8-25 $M_{\odot}$) or a black hole (BH, for initial masses greater than 25 $M_{\odot}$) (Carroll & Ostlie 2006).

This work will focus on SNe Ia, which represent the thermonuclear runaway explosions of white dwarf (WD) stars. Low mass stars do not produce CC SNe, and instead end their lives as WDs. WDs are small in size, having radii comparable to that of the Earth. They do not undergo fusion, and are supported by electron degeneracy pressure. Isolated WDs are remarkably stable, slowly cooling over billions of years (Kilic et al. 2012). However, WDs that have close binary companions can become unstable and explode as SNe Ia. The exact nature of the binary systems leading to SNe Ia is an open question.

1.1.1 SN Ia Progenitors

Despite their fundamental role in cosmology, we do not know the exact progenitor systems of SNe Ia. As will be discussed in §1.1.4, the use of SNe Ia for cosmology is systematics, not statistics, limited. As a result, a complete understanding of the progenitor systems of SNe Ia would be helpful. There are two classes of progenitor channels for SNe Ia: single degenerate (SD) and double degenerate (DD) models. In the SD model, a carbon-oxygen (CO) WD increases in mass through accretion from a non-degenerate stellar companion (Whelan & Iben 1973). The WD would have an initial mass of $\sim 1.3\ M_{\odot}$ and would accrete mass until it reaches the Chandrasekhar (M_{CH}, $1.39\ M_{\odot}$) limit (though see Di Stefano et al. 2011, which describes a SD model producing super-M_{CH} explosions). At this critical mass, carbon in the core ignites in a thermonuclear runaway and the star explodes. The companion star could be a main sequence star, a subgiant, or a red giant (e.g., Di Stefano 2010a; Shen & Bildsten 2008). Moreover, the SD model has been extended to include a helium star (e.g., Yoon & Langer 2003; Wang et al. 2009a) or even an M dwarf companion (Wheeler 2012). In the SD model, the accretion occurs by the companion filling its Roche Lobe. In the case of a red giant star, stellar winds alone could cause the WD companion to gain mass (Di Stefano 2010a).

The double degenerate model for SN Ia involves the merging of two WDs (Iben & Tutukov 1984; Webbink 1984). In this scenario, the two WDs merge after losing energy and

angular momentum to gravitational waves. There are fewer constraints on the explosions in this scenario; the total mass of the SN Ia could be below, near, or above the M_{CH} (see review by Maoz et al. 2014). Simulations predict different methods for the build up of mass and subsequent explosion. The most common models have unequal masses for the two WDs (see Maoz et al. 2014). In this case, the more massive WD can tidally disrupt and accrete matter from the lower mass star, causing an explosion.

Both SD and DD models have serious problems matching observations of SNe Ia (e.g., see Maoz et al. 2014). In order to better understand both models, we need to identify progenitor systems in nature. One method for doing so is by studying Supersoft X-ray Sources (SSSs).

1.1.2 SSSs

Luminous supersoft x-ray sources (SSSs) were first detected observationally by the Einstein Observatory in the early 1980s (Long et al. 1981). SSSs were established as a class by the *ROSAT* Observatory which discovered roughly 30 of these interesting sources in the Magellanic Clouds, the Andromeda galaxy (M31), and the Milky Way (Greiner 2000). Subsequent observations by *Chandra* and *XMM-Newton* observatories of the Galaxy and external galaxies have discovered hundreds of soft X-ray sources with properties that both exemplify and extend the class of SSSs (e.g., Orio et al. 2010; Di Stefano et al. 2010b, references therein). SSSs are quite luminous, having luminosities greater than 10^{36} ergs s^{-1}. They are characterized by soft X-ray emission, with little to no emission above 1 keV in energy. This is unusual because the spectra of most X-ray sources are dominated by harder emission (i.e., most of the emission is above 2 keV). Astronomers who study SSSs break down the emission into three energy bins: the "soft" bin (denoted S, 0.1-1.1 keV photons), "medium" bin (denoted M, 1.1-2 keV photons), and "hard" bin (denoted H, 2-7 keV photons). A source is classified as an SSS by two strict ratios of these bands (Di Stefano et al. 2004a). For a source to be considered an SSS, it must satisfy:

$$HR1 = \frac{M - S}{M + S} < -0.8 \; and \tag{1.1}$$

$$HR2 = \frac{H - S}{H + S} < -0.8 \tag{1.2}$$

Furthermore, these sources seem to be best modeled by a thermal, black body spectrum. The formula for black body radiation is Planck's function:

$$B_\nu(T) = c^{-2} \frac{2h\nu}{e^{h\nu/kT} - 1} \tag{1.3}$$

where k is Boltzmann's constant , h is Planck's constant, T is the effective temperature, ν is the frequency, B_ν is the power per unit area per unit frequency per unit steradian. From equation (1.3), we can see that for higher temperatures, the power is emitted at larger frequencies (higher energies). Di Stefano et al. (2003b) examined a series of simulated spectra to determine which temperatures corresponded to SSSs. The simulations revealed that sources with black body temperatures as low as $kT = 25$ eV (T $\sim 3{\times}10^5$ K) and as high as $kT = 175$ eV (T $\sim 2{\times}10^6$ K) are detectable as SSSs. This result held for several different values of column density of neutral hydrogen atoms (N_H) along the line of sight. Neutral hydrogen between a source and the Earth absorbs part of the emission and reduces the number of photons detected. The larger the value of N_H, the greater the absorption. In fact, this is why only a handful of SSSs have been found in the Galaxy; as the column densities can be quite large and block emission from the SSS. Absorption is particularly a problem for SSSs, as low energy X-ray photons are preferentially blocked relative to higher energy X-ray photons as the value of N_H increases (Di Stefano et al. 2003b). It is this reason that many searches for SSSs occur in nearby galaxies, as absorption is often smaller (see Di Stefano et al. 2004a, 2010a; Orio et al. 2010; Stiele et al. 2010).

Several astronomical systems can produce supersoft emission including WD binaries (e.g.

Pietsch et al. 2007; Orio et al. 2010; Stiele et al. 2010; Di Stefano et al. 2010b, references therein). Accreting WDs leading to SSSs can broadly be divided into two groups based on the rate of accretion. If the accretion rate onto a WD from a massive companion is low (10^{-8} - 10^{-9} $M_{\odot}$/yr), the WD cannot retain the transferred material (Carroll & Ostlie 2006). In this case, the WD will expel the mass as a nova after building up $\sim 10^{-4}$ $M_{\odot}$ (note, novae differ from SNe Ia, as they are much less luminous and do not destroy the WD). WDs that have recently experienced novae have temperatures and luminosities that can make them detectable as SSSs (e.g., Sala & Hernanz 2005). Although novae do not spend much time as SSSs, many SSSs detected in M31 were recent novae (Pietsch et al. 2005, 2007; Stiele et al. 2010, references therein). Novae in a supersoft state are detected with $kT \sim 50$ eV and L_X of $10^{37} - 10^{38}$ ergs s^{-1} (e.g., Stiele et al. 2010, references therein). These WD systems do not lead to SNe Ia; they do not represent the SD WDs described in 1.1.1.

If the accretion rate onto a CO WD is high ($\sim 10^{-7}$ $M_{\odot}$/yr), the WD can grow in mass leading to a SN Ia (Iben 1982; Fujimoto 1982; Shen & Bildsten 2008; Di Stefano 2010a). In this model, the hydrogen donated from the companion undergoes nuclear burning (NB) into He on the WD, leading to the mass increase. While the WD is gaining mass, the system should be observable as a SSS, as in the case of Cal 83 (van den Heuvel et al. 1992). Although this SSS model assumes a massive companion star (~ 1.2 $M_{\odot}$ or greater), this is not a strict requirement. As long as the accretion rate of hydrogen is high enough, NB will occur and the WD should be detectable as a SSS. As noted above, Wheeler (2012) has proposed a M dwarf SD model, which also produces the necessary rate of accretion for nuclear burning to occur.[1]

Figure 1.1 (Di Stefano 2010a) shows the progression of a nuclear burning WD to the M_{CH}. The top panel shows the accretion rate required for NB for a given mass of the WD. As the WD increases in mass, so does the rate of accretion required to sustain NB. The two

[1]However, in one of the SD models described above, the companion star does not fit the NB model. If the companion is a He star, the donated material will be helium. However, several studies (Wang et al. 2009a; Yoon & Langer 2003) have shown that the He accretion will also produce SSSs, albeit for a short duration and at different values of kT than the model presented here.

black curves represent the maximum and minimum accretion rates for the model. Note, the upper bound exists due to the Eddington limit. This limit is derived by setting the gravitational pressure gradient equal to the radiation pressure gradient (assuming hydrostatic equilibrium). This leads to a maximum luminosity (L_{Ed}) that can be sustained in hydrostatic equilibrium (Carroll & Ostlie 2006):

$$L_{Ed} = \frac{4\pi GMc}{\kappa} \approx 1.46 \times 10^{38} M/M_{\odot} \text{ ergs s}^{-1} \tag{1.4}$$

where M is the mass of the WD and κ is the mean opacity. Accretion above this maximum reduces the amount of incoming matter that is burned. The middle panel show the luminosity of the WD. For nuclear burning, the luminosity is in the plot is:

$$L_{NB} = 2.4 \times 10^{38} \text{ erg s}^{-1} \left(\frac{\eta}{0.007}\right) \left(\frac{f}{0.75}\right) \left(\frac{\beta \dot{M}_{in}}{8 \times 10^{-7} M_{\odot} \text{ yr}^{-1}}\right) \tag{1.5}$$

where η is the efficiency (set to 0.007), f is the fraction of material that is burned (set to 0.75), and β represents the retention factor for the WD (set to unity) Just below the nuclear burning curves (in red points), the luminosity is from accretion ($L_{acc} = \dot{M}_{in} M_{WD} G / R_{WD}$). The plot shows that high mass WDs accreting below the NB rate are still very luminous. The bottom panel shows the temperature of the NB WDs. As the WD nears explosion, the source increases to the edge of the SSS regime ($\sim$150 $k\,T$, $\sim 10^{38}$ ergs s^{-1}). At these temperatures and luminosities, SSSs sources should be easy to find.

Although Figure 1.1 was calculated for SD models, it is applicable to DD models as well. As mentioned earlier, the most common DD models require unequal masses for the two WDs (see Maoz et al. 2014). Thus, the two WDs form at different times, due to the difference in mass of their progenitor stars (Carroll & Ostlie 2006). When the first WD forms, the companion will still be in its red giant phase (Di Stefano 2010b). During this time, Di Stefano (2010b) shows that the WD would accrete matter from the red giant. Moreover, the accretion should be large enough for NB to occur. The accreting WD does

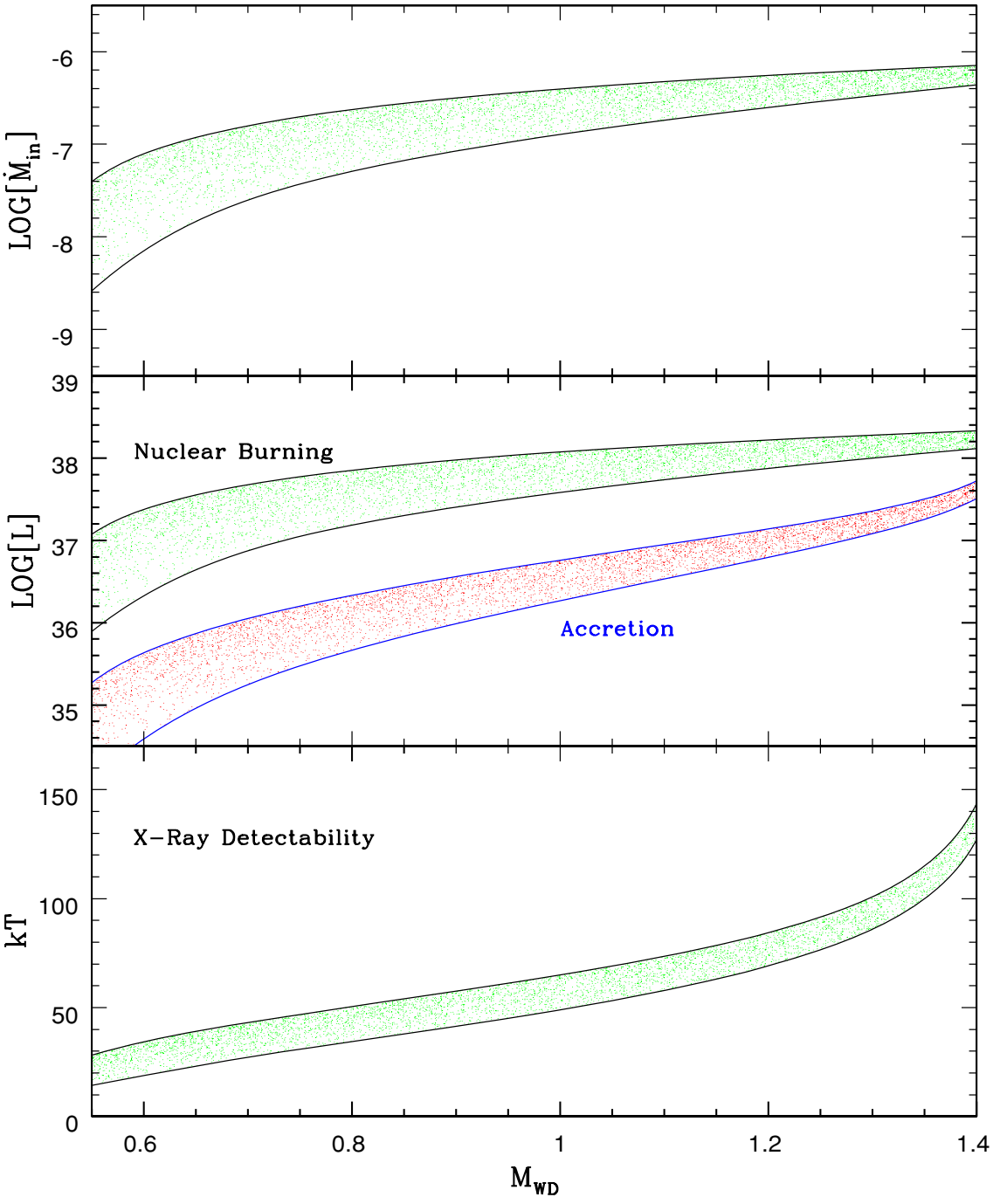

Figure 1.1 Figure taken from Di Stefano (2010a) showing a nuclear burning CO WD. The green points represent nuclear burning, while the red points represent accretion only (just below the nuclear burning rate, with $L_{acc} = \dot{M}_{in} M_{WD} G / R_{WD}$). The top panel shows the accretion nuclear burning accretion rate, middle panel shows the luminosity, and the bottom panel shows the blackbody temperature of the WD.

not reach the M_{CH}, and would not be as bright as the SD WD. However, these systems should be luminous enough to be detected by current X-ray telescopes.

Since NB WDs are luminous, they should be easy to find in nearby galaxies (e.g., Di Stefano 2010a). The easiest place to look for them is in pre-explosion imaging of SNe Ia. These images are taken serendipitously; that is, we do not know when SNe Ia will explode and cannot plan to observe them ahead of time. In a few cases, we have been able to place constraints on the progenitor system of a SN Ia. One such case is SN 2011fe. SN 2011fe, located in M101 (6.4 Mpc away), was the closest SN Ia in decades. Figure 1.2 (Li et al. 2011a) shows an Hubble Space Telescope (*HST*) image of the location of the SN prior to the explosion. We did not detect any stars within the 1σ positional error of SN 2011fe. The closest stars (labeled as star 1 and 2 on the image), are located 9σ away and are not associated with the SN. From the optical image, we were able to rule out a red giant and He star companion to the WD. This result was confirmed by other groups (Nugent et al. 2011; Bloom et al. 2012).

In 2012, two other SNe Ia progenitor systems were constrained. Dilday et al. (2012) analyzed the spectra of PTF 11kx, and found it to be consistent with a red giant companion. Schaefer & Pagnotta (2012) looked at SNR 0509-67.5, and determined the position of the explosion. From HST imaging of the region, they were able to rule out all SD companions except a M dwarf.

Although these discoveries have been informative, there are too few nearby SNe Ia to statistically determine which progenitor model or models are correct. One way to study a large number of SNe Ia progenitors is by searching for SSSs in nearby galaxies. As mentioned earlier, these systems should be easy to find due to their high luminosities. Unfortunately, several studies have concluded that there are not enough SSSs in nearby galaxies to account for the rate of SNe Ia found in the Universe (Di Stefano et al. 2010b; Di Stefano 2010a,b; Gilfanov & Bogdán 2010). The most exhaustive study was done by Di Stefano (2010a,b). Assuming that SD models produce the majority of SNe Ia, we should expect several hundred

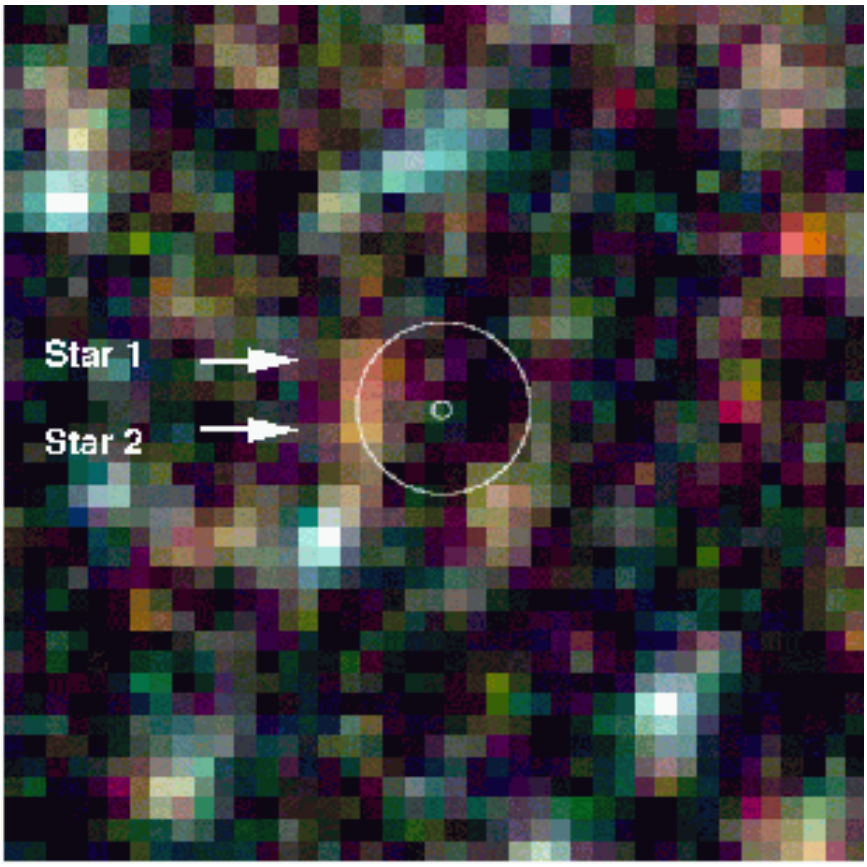

Figure 1.2 Figure taken from Li et al. (2011a) showing an HST image ($2''$x $2''$) of SN 2011fe before the explosion. Note that the smaller circle represents the 1σ error on the position of the SN. The two stars labeled on the image are red giants, at 9σ from the explosion. We determined that these two stars are not associated with SN 2011fe.

NB WDs in a galaxy similar to the Milky Way (Di Stefano 2010a). If we assume that DD models produces the majority of SNe Ia, the number actually increases to about one thousand SSSs (Di Stefano 2010b). Surveys of the Local Group and other nearby galaxies find far fewer SSSs (on the order of tens of SSSs per galaxy) than the predicted number. Two groups (Wheeler & Pooley 2013; Nielsen et al. 2013) have suggested that the supersoft radiation is absorbed by the circumstellar matter in a progenitor system and is re-radiated in the UV. However, detecting this radiation would be hard and very few (less than 100 sources) would be detectable in the UV (Wheeler & Pooley 2013).

Quasisoft X-ray sources

An additional problem arises in regards to the number of NB WDs: not all the SSSs found in nearby galaxies are SNe Ia progenitors. Some SSSs are attributed to novae, as mentioned earlier. Others are associated with non-WD systems. As more SSSs were discovered, the class extended to include slightly hotter systems which produce soft X-ray emission. These sources have more emission above 1 keV than SSSs, but little to no emission above 2 keV. These sources, dubbed quasisoft X-ray sources (QSSs), are classified using a different set of ratios than for SSSs (Di Stefano et al. 2003b). QSSs have similar luminosities as SSSs, but they are generally hotter, with temperatures of 175 eV $< kT <$ 350 eV. Like SSSs, QSSs have been discovered in the Galaxy and external galaxies. However, they differ in their physical nature, as QSSs generally come from NS and BH systems.

NSs often have strong magnetic fields associated with them (Carroll & Ostlie 2006). In a binary system, the magnetic field tends to channel accreting gas towards the poles at a distance known as the Alfven radius. The Alfven radius is defined when the magnetic energy density is equal to the kinetic energy density of the accreting material. The equation for r_A is (in SI units) (Carroll & Ostlie 2006):

$$r_A^7 = \frac{8\pi B_s^4 R^{12}}{\mu_0^2 G M \dot{M}^2} \tag{1.6}$$

where B_s is the magnetic field at the surface of the NS, R is the radius of the NS, M is the mass of the NS, and $\dot{M}$ is the accretion rate.

BHs have also been considered as possible SSSs and QSSs. A general property of black holes is their event horizon; the point at which light can not escape the black hole. The event horizon is defined at the Schwarzchild radius, which is: $r_s = 2GM/c^2$. The effective potential of a non-rotating black hole allows a stable circular orbit of matter to occur at $3r_s$=$6GM/c^2$ (Carroll & Ostlie 2006). Accreting black holes can exhibit blackbody (thermal-dominant) states in which the emission is dominated by a component emanating from the inner portion

of the accretion disk (e.g., Remillard & McClintock 2006). SSSs and QSSs have both been suggested as possible black holes. For example, M101-ULX-1 is almost certainly a black hole and has exhibited both supersoft and quasisoft states (e.g., Kong et al. 2004; Kong & Di Stefano 2005; Mukai et al. 2005). M101-ULX-1, however, is an ultraluminous source, with a luminosity greater than 10^{39} ergs/s and not typical for the SSS or QSS classes. Its mass could be either in the range typical of Galactic stellar-mass BHs or else in the higher range $(50 - 10^4\,M_{\odot})$ suggested for intermediate-mass BHs. Cowley et al. (1990) has suggested that Cal 87 (located in the Large Magellanic Cloud), one of the first SSSs ever discovered, is a stellar mass BH.

In Chapter 2, we explore WD, NS, and BH models to fit r1-25, an interesting X-ray source in M31 that changed state between SSS and QSS.

1.1.3 SNe Classification

We now look at how CC SNe are distinguished from SNe Ia; an important distinction as SNe Ia are a crucial probe of dark energy. SNe are observationally classified into two broad types based on their spectral properties (Minkowski 1941). Type II SNe have significant hydrogen emission features, whereas Type I SNe do not. Type I SNe are further classified into three important subcategories: Type Ia, Type Ib, and Type Ic. Figure 1.3 (Filippenko 1997) shows examples of each type of SN. As mentioned earlier, SNe Ia are distinct from all other SNe as they do not involve CC. Although part of the same type, SNe Ia differ from Type Ib and Ic SNe, as they show a deep absorption of Si II at about 6150 Å(Wheeler & Harkness 1990). Moreover, SNe Ia light-curves are powered by the decay of ^{56}Ni to ^{56}Co to ^{56}Fe (Arnett 1996). Although SNe Ia spectra are not homogeneous (see Blondin et al. 2012), this Si II feature is almost always seen. Type Ib and Type Ic SNe are hard to distinguish, and are often considered together as class (Type Ibc SNe; Filippenko 1997).

Another important method for distinguishing between the SN types is through the host galaxy environment. CC SNe (Type II, Type Ib, and Type Ic) are not found in elliptical

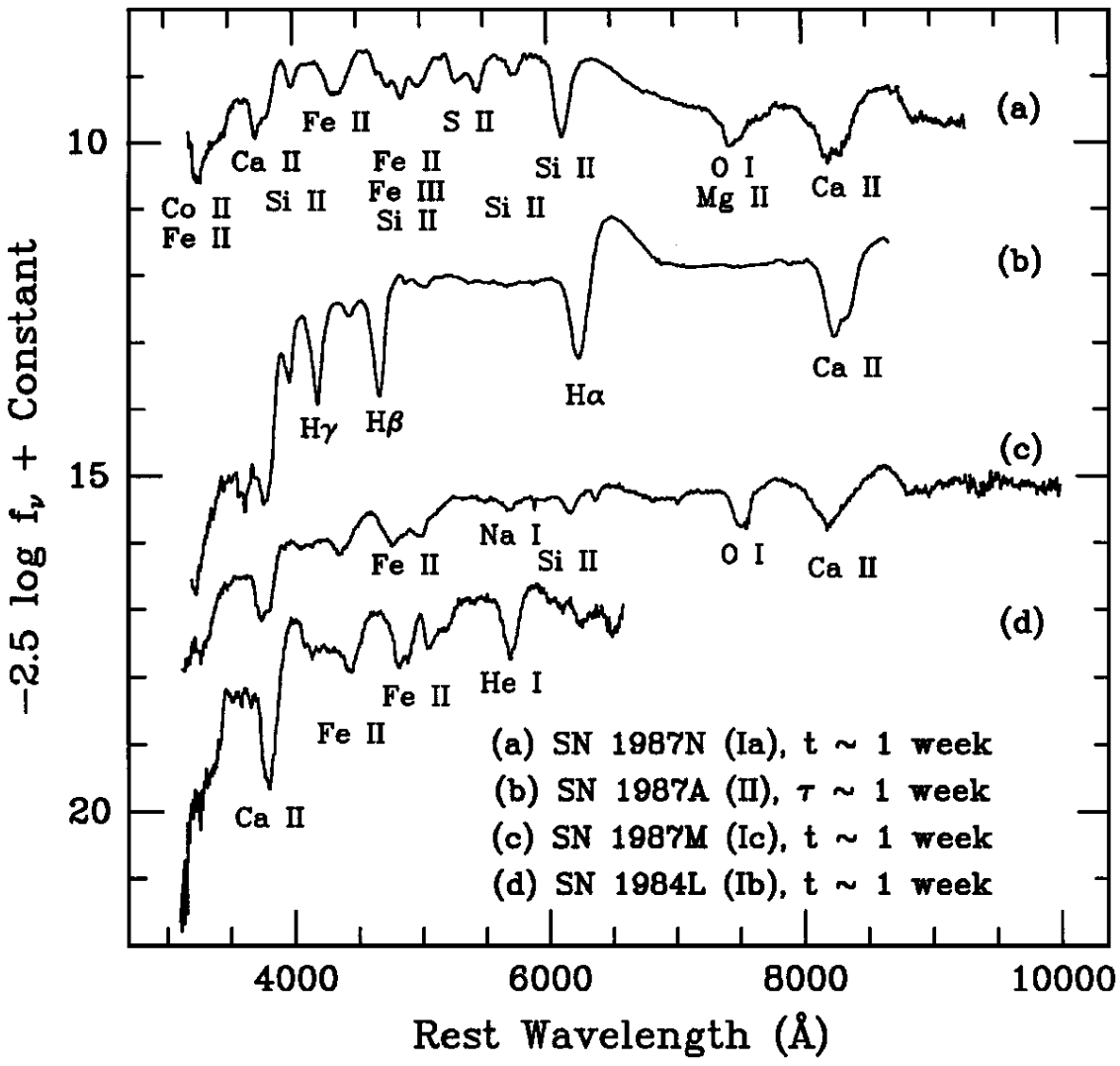

Figure 1.3 Figure taken from Filippenko (1997) showing the different types of SNe

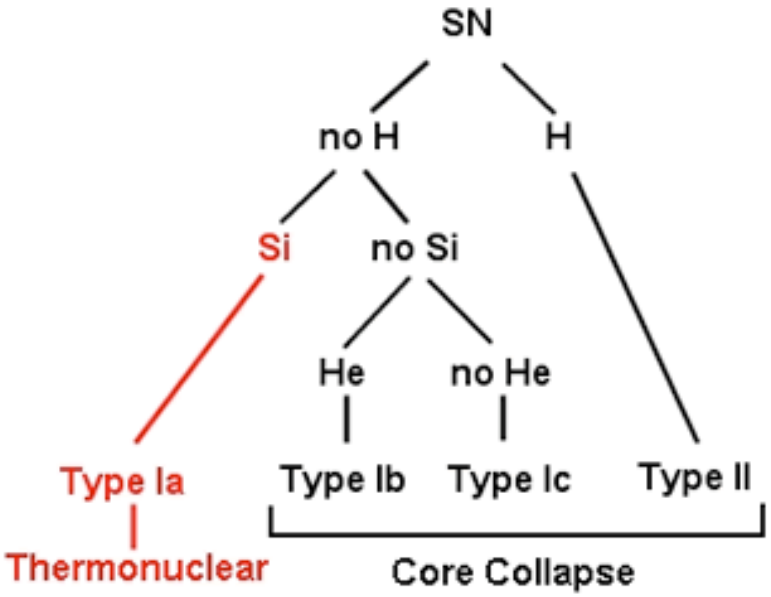

Figure 1.4 Diagram showing the classification and explosion mechanisms for each type of SNe. Figure from http://astronomy.swin.edu.au/cosmos/S/supernova+classification.

galaxies and very rarely found in S0 galaxies (Filippenko 1997; Cappellaro et al. 1999; Mannucci 2005; Foley & Mandel 2013). In contrast, SNe Ia are found in elliptical galaxies and do not have a preference for star forming regions (van Dyk 1992). Figure 1.4 shows a diagram summarizing SNe classifcation and explosion mechanisms (figure courtesy of Curtis McCully).

Modern SNe surveys are very efficient, discovering hundreds of SNe Ia over a 2-3 year period (e.g., Guy et al. 2010; Sako et al. 2014). These SNe are discovered photometrically, and sometimes cannot be spectroscopically classified. This is due to a lack of resources to follow the SNe. Distant SNe are particularly hard to classify, requiring vast amounts of telescope time to definitively classify (see Jones et al. 2013).

Thankfully, SNe can also be distinguished by their light-curves. Figure 1.5 shows light-curves for different SNe in the B filter. Qualitatively, we can clearly see that SNe Ia are the

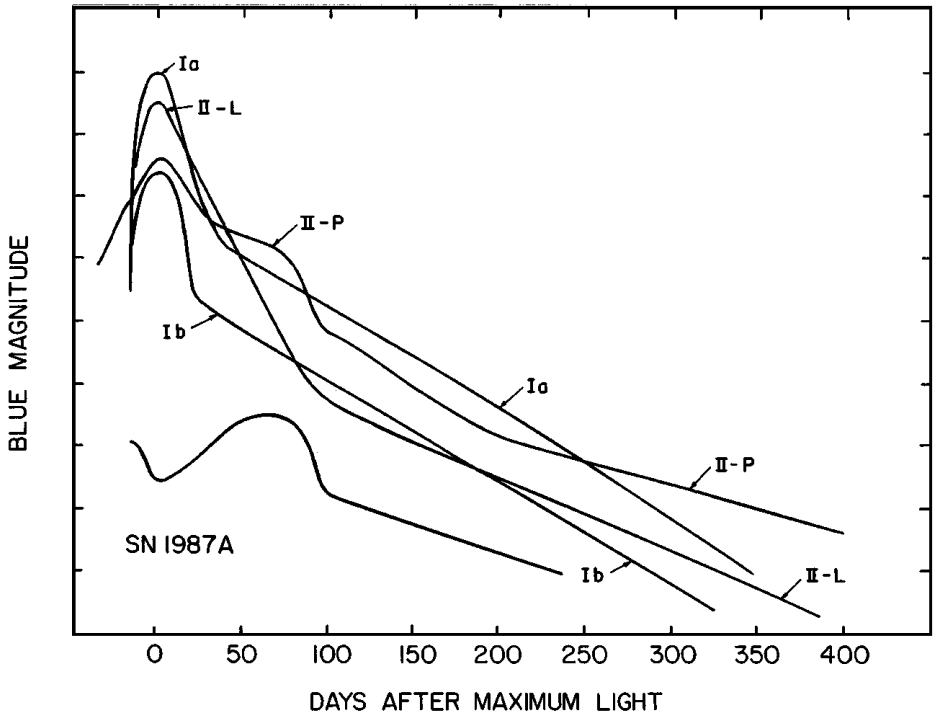

Figure 1.5 Light-curves for different SNe types.

most luminous type.[2] Moreover, the figure indicates that classification should be possible, provided the light-curve of the SN is well sampled. The process of classification is aided by obtaining photometry in different filters. Each SN type has distinct colors, and will evolve differently in each photometric band. SNe classification by their light-curves is further explored in Chapter 3.

1.1.4 SNe Ia Light-Curves

We now take a closer look at SNe Ia light-curves. SNe Ia can be used to measure cosmological distances because they are good standard candles and very bright. Standard candles have a known intrinsic luminosity, which can be used to determine distances:

$$F_{observed} = \frac{L_{intrinsic}}{4\pi D_L^2} \tag{1.7}$$

[2]Super luminous CC SNe can be brighter than SNe Ia, but they are very rare (see Cooke et al. 2012).

In this equation, F is the observed flux, L is the intrinsic luminosity, and D_L is the luminosity distance of the source. We can measure the flux of the source using telescopes, and with a known luminosity, we can solve for the distance. Using distance and redshift measurements, we can constrain dark energy, as well as other cosmological parameters. The redshift can be determined through SNe Ia spectra or host galaxy spectra. If we assume a flat Universe, which we find from measurement of the cosmic microwave background (Planck Collaboration et al. 2014, references therein), then the luminosity distance can be expressed as:

$$D_L = \frac{c}{H_0}(1+z)\int_0^z \frac{dz}{[\Omega_{\rm M}(1+z)^3 + \Omega_\Lambda(1+z)^{3(1+w)}]^{\frac{1}{2}}} \tag{1.8}$$

where c is the speed of light, H_0 is Hubble's Constant, z is the redshift of the SN Ia, $\Omega_{\rm M}$ is the matter density of the Universe at present time, Ω_Λ is the dark energy density of the Universe today at present time, and w is the equation of state of dark energy ($w = P/(\rho c^2)$). Standard ΛCDM cosmology assumes w = -1 always, which is an assumption that can be tested with SNe Ia. Using equation 1.8, astronomers have been able to place strong constraints on Ω_Λ, $\Omega_{\rm M}$, and w (e.g. Suzuki et al. 2012; Riess et al. 2007; Kessler et al. 2009a; Sullivan et al. 2011).

The discussion so far has assumed that SNe Ia are perfect standard candles. In the early 1990s, astronomers realized this was not exactly the case (Phillips 1993; Filippenko 1997). SNe Ia have a range of or intrinsic luminosities, with peak absolute magnitudes (M) varying by $\sim$ 1 mag in optical filters (see Figure 1.6).

However, SNe Ia are considered standardizable candles, as their light-curves can be calibrated to the same luminosity. This was first noted by Phillips (1993), who found that the faster a SN Ia declined, the lower its $M_{\rm max}$ (absolute magnitude at peak). Similarly, slow declining SNe Ia correspond to more luminous explosions. Moreover, he found that the decline rate from peak to 15 days past peak in the B filter was linearly related to the $M_{\rm max}$. This relationship is demonstrated in Figure 1.6.

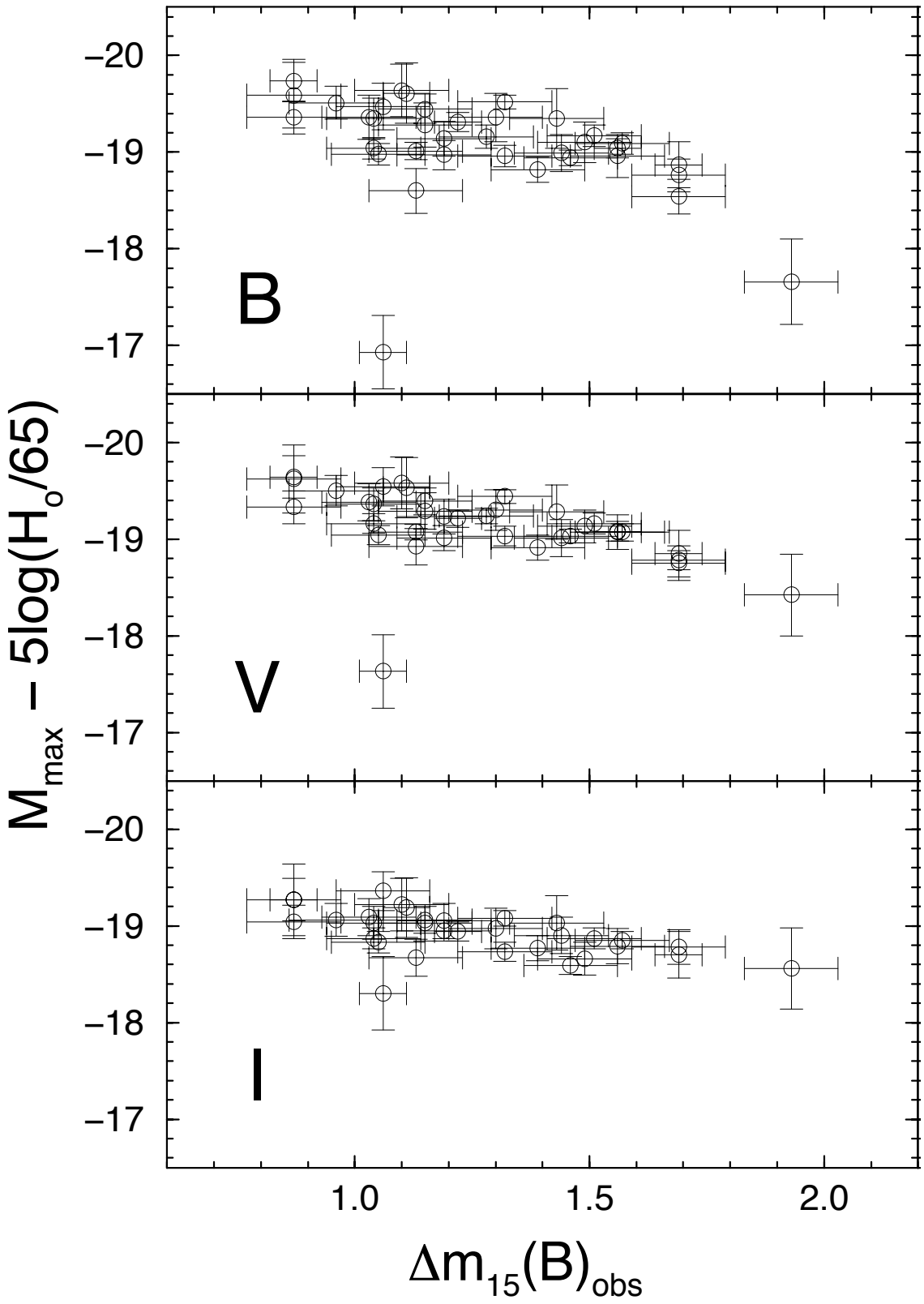

Figure 1.6 Figure taken from Phillips et al. (1999) showing the peak absolute magnitudes of 41 SNe Ia in the B, V, and I bands. The plot shows considerable variation in the peak brightness of the SNe. The x-axis, $\Delta m_{15}(B)$, indicates how much the SN has faded from peak to fifteen days past peak. The $\Delta m_{15}(B)$ parameter is one method used to standardize SNe Ia light-curves.

The model presented in Phillips (1993) has been extended to encompass the full light-curve in every available filter (these models are called SNe Ia light-curve fitters). The process of light-curve fitting involves determining the best fit parameters, and using the parameters to determine the distance to the SN. This process is quite complex, and plagued with systematic uncertainties (e.g., Kessler et al. 2009a; Scolnic et al. 2014a; Conley et al. 2011). In fact, with $\sim$ 1000 SNe Ia usable for cosmology, systematical uncertainties dominate over statistical ones. In Chapter 3, we make use of two light-curve fitters in analyzing SNe Ia. In Chapter 4, we explore the systematic uncertainties associated with light-curve fitters. We also present our initial work on a new light-curve fitter in this chapter.

1.1.5 SNe Ia and Gravitational Lensing

In this section, we explore the use of SNe Ia to constrain Gravitational lensing. Einstein's General Theory of Relativity interprets gravity as the curvature of spacetime (Carroll 2004). A prediction from the theory is that light must also follow this curvature. Intervening mass between an astronomical source and the Earth can change the appearance of the source. With the correct mass and the geometric configuration, the source can be magnified and its shape distorted. This process, called gravitational lensing, occurs when light that would ordinarily not reach us is bent toward us. The exact location and flux of this light can inform us about the mass distribution of the lens.

In the case of strong lensing, the effects can be pronounced. If the source and the lens are perfectly aligned, an Einstein ring can form around the lens (Massey et al. 2010). Otherwise, if the alignment is not perfect, several images of the source will appear around the lens (Massey et al. 2010). Galaxies that are lensed can become elongated and magnified. Near galaxy clusters, we see many strong lensing features(Massey et al. 2010). Figure 1.7 shows a color image of a galaxy cluster, MACS1206.2-0847, taken as part of the Cluster Lensing and Supernova survey with Hubble (CLASH). Several elongated background galaxies can be seen, which form arcs around the cluster. Gravitational lensing is responsible for these

Figure 1.7 False color image of MACS1206.2-0847 taken as part of CLASH. The elongated galaxies near the center of the image show the effects of lensing.

distortions.

The equations that govern gravitational lensing are as follows. From Fermat's Principle, the excess travel time is given by (Treu 2010):

$$t = \frac{D_d D_s (1+z_i)}{c D_{ds}} \left[\frac{1}{2} |\boldsymbol{\theta} - \boldsymbol{\beta}|^2 - \phi(\theta) \right] \tag{1.9}$$

The angular diameter distances and angles in equation 1.9 are shown in Figure 1.8. In the equation, ϕ is the lensing potential which satisfies:

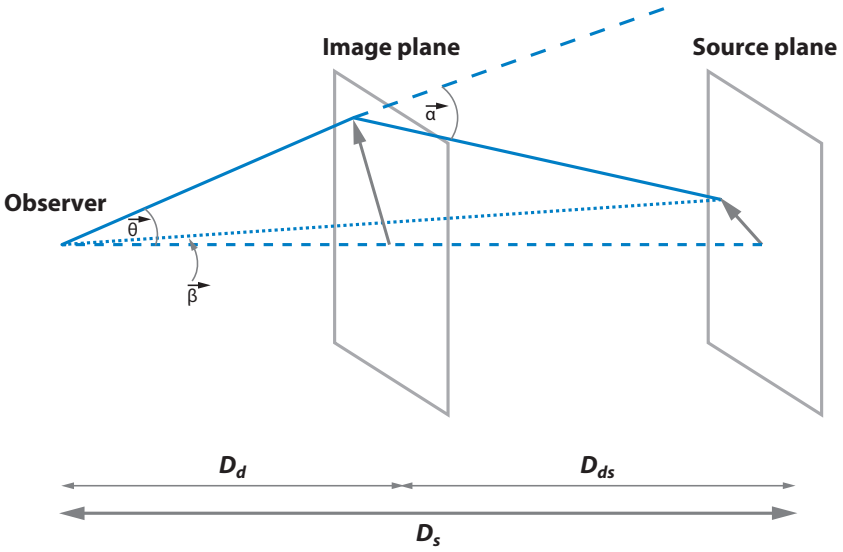

Figure 1.8 Figure taken from Treu (2010) showing the standard gravitational lensing geometry.

$$\nabla^2\phi = 2\kappa \tag{1.10}$$

where κ is the convergence (Treu 2010). Additionally, the projected surface mass density of the lens in terms of critical surface mass density (Treu 2010):

$$\Sigma_c = \frac{c^2 D_s}{4\pi D_d D_{ds}} \tag{1.11}$$

From the equations above, we can define the Einstein radius. This radius is defined as the region where the average surface mass density of a circular lens mass distribution is equal to the critical surface mass density (Equation 1.11) (Treu 2010). The Einstein radius defines the area where strong lensing can occur (i.e., Einstein rings and multiple images). The exact equation for the Einstein radius, will depend on mass distribution of the lens. For a point mass lens, it is:

$$\Theta_E = \frac{4GM}{c^2}\frac{D_s}{D_d D_{ds}} \tag{1.12}$$

The last two terms in equation 1.9(in the brackets) deal with the time delays associated with the images (Refsdal 1964). The first term comes from the altered path of the light from the source (geometric time delay), which adds to the delay time between images. The relativistic Shapiro Delay time accounts for the second term; that is, time dilation occurs from the massive potential (gravitational time delay). The two delays cause the time delay in observing the images (Massey et al. 2010; Treu 2010).

From equation 1.9, the lens equation can be derived (Treu 2010):

$$\boldsymbol{\beta} = \boldsymbol{\theta} - \nabla\phi = \boldsymbol{\theta} - \boldsymbol{\alpha} \tag{1.13}$$

The Jacobian of the transformation between the source and the observed image is:

$$\frac{\partial\boldsymbol{\beta}}{\partial\boldsymbol{\theta}} = \delta_{ij} - \frac{\partial^2\phi}{\partial\theta_i\partial\theta_j} = \begin{pmatrix} 1-\kappa-\gamma_1 & -\gamma_2 \\ -\gamma_2 & 1-\kappa+\gamma_1 \end{pmatrix} \tag{1.14}$$

where where κ is the convergence, and γ_1 and γ_2 are the cartesian coordinates of the shear (Treu 2010). Finally, the magnification, μ, of an image is equal to the determinant, so:

$$\mu = \frac{1}{(1-\kappa)^2 - \gamma_1^2 - \gamma_2^2} \tag{1.15}$$

In strong lensing systems, which are generally present near galaxy clusters, the lensing constraints on the mass distribution come from the relative positions and fluxes of images. This leads to the mass sheet degeneracy problem, which was first noted by Falco et al. (1985). Falco et al. (1985) showed, for a system with two images, that the mass distribution of the lens could be transformed by a uniform mass sheet without changing the

observable quantities (relative magnifications, relative fluxes, and image positions). This transformation would only require a change in the intrinsic luminosity of the source. For most astronomical sources, such as galaxies and quasars, we do not know their intrinsic luminosity. For this reason, the mass sheet degeneracy is a significant part of the uncertainties of lensing mass reconstructions (Treu 2010; Schneider & Sluse 2013).

SNe Ia provide a clear solution to the mass sheet degeneracy (Kolatt & Bartelmann 1998). As standarizable candles, their luminosities are well constrained ($\sim$ 10%; Wood-Vasey et al. 2007a). The ideal location to look for these SNe Ia is behind galaxy clusters. Most SNe Ia surveys, however, exclude regions of the sky that contain galaxy clusters (i.e., Graham et al. 2008; Dilday et al. 2010). Moreover, due to their transient nature, very few strongly lensed SNe have been found. Even when lensed SNe are found behind galaxy clusters, some will be CC (Amanullah et al. 2011), which cannot be used to break the degeneracy.

The CLASH survey provided an opportunity to find lensed SNe Ia. The survey observed 25 galaxy clusters in 16 HST broadband filters covering the near-ultraviolet to the near-IR with the Advanced Camera for Surveys and the Wide Field Camera 3. In Chapter 3, we investigate three lensed SNe found behind three CLASH galaxy clusters.

Chapter 2

Analysis of a State Changing Supersoft X-Ray Source in M31

ABSTRACT

We report on observations of a luminous supersoft X-ray source (SSS) in M31, r1-25, that has exhibited spectral changes to harder X-ray states. We document these spectral changes. In addition, we show that they have important implications for modeling the source. Quasisoft states in a source that has been observed as an SSS represent a newly-discovered phenomenon. We show how such state changers could prove to be examples of unusual black hole or neutron star accretors. Future observations of this and other state changers can provide the information needed to determine the nature(s) of these intriguing new sources.

2.1 INTRODUCTION

Luminous supersoft X-ray sources (SSSs) were established as a class by *ROSAT* observations of roughly 30 sources in the Magellanic Clouds, Milky Way, and M31 (Greiner 2000). *Chandra* and *XMM-Newton* observations of external galaxies have now discovered hundreds of soft X-ray sources with properties that both exemplify and extend the class of SSSs (e.g., Di Stefano et al. 2003b; Kong & Di Stefano 2003; Di Stefano et al. 2003a; Di Stefano & Kong 2004; Greiner et al. 2004; Di Stefano et al. 2006, 2010a; Orio et al. 2010; Liu 2011). Even though they are bright, with luminosities higher than 10^{36} erg s^{-1}, we know of only a handful in the Galaxy, because the radiation they emit is readily absorbed by the interstellar medium. In fact, the SSSs used to define the class display little or no emission above

1 keV. Roughly a dozen SSSs are known in the Magellanic Clouds (Greiner 2000). Some of these are associated with novae, and are clearly hot white dwarfs (see Greiner 2000). In M31, some SSSs have been shown to be associated with supernova remnants and novae (Orio et al. 2010; Pietsch et al. 2005, 2007; Stiele et al. 2010).

The most mysterious component of the class is comprised of X-ray binaries, most with orbital periods of a day or less. A promising model for these sources is one in which their prodigious luminosities are produced by the nuclear burning of matter accreted by a white dwarf (van den Heuvel et al. 1992; Rappaport et al. 1994). Nuclear burning should allow the white dwarf to retain accreted matter and increase in mass. Binary SSSs have therefore been suggested as progenitors of accretion-induced collapse (van den Heuvel et al. 1992) and of Type Ia supernovae (Rappaport et al. 1994). Nuclear-burning white dwarfs in wider orbits are also expected (Hachisu et al. 1996; Di Stefano & Nelson 1996). Indeed, symbiotic binaries have been observed as SSSs (e.g., Greiner 2000; Orio et al. 2007).

Because it is difficult to detect SSSs in the Milky Way, and the Magellanic Clouds are too small to host a large population, it is important to search for SSSs in external galaxies. The advent of *Chandra* and *XMM-Newton* has made such searches possible. Hundreds of SSSs have now been discovered, some in galaxies as far from us as the Virgo cluster (Liu 2011). As the numbers of SSSs has increased, we have begun to find evidence of sources that have properties different from those of the SSSs that established the class. Some SSSs are hundreds of times more luminous than the Eddington limit for a Chandrasekhar-mass white dwarf. Several of these ultraluminous supersoft sources are candidates for accreting black holes (Di Stefano et al. 2004a; Kong et al. 2004; Kong & Di Stefano 2005; Mukai et al. 2005; Liu & Di Stefano 2008). In addition, the search for the softest sources has identified a class of sources that are significantly harder than SSSs, yet also significantly softer than canonical X-ray sources: quasisoft X-ray sources (QSS; Di Stefano et al. 2004b; Di Stefano & Kong 2003; Di Stefano et al. 2004a). QSSs have luminosities above 10^{36} ergs s^{-1}, but emit few or no photons with energy above 2 keV. Some could be hot white dwarfs in which

there is an additional hard component and/or which are highly absorbed. Those fitting this model are good candidates for progenitors of Type Ia supernovae, because they would likely correspond to the most massive nuclear-burning white dwarfs (e.g., Rappaport et al. 1994; Di Stefano 2010a, references). Others are too hot to be white dwarfs and may correspond to either black holes or neutron stars.

In this paper we report on a source (r1-25) that has been observed to switch between SSS and QSS states (Stiele et al. 2008, 2010; Di Stefano et al. 2010b; Orio et al. 2010). Unlike M101-ULX-1 (e.g., Kong et al. 2004; Kong & Di Stefano 2005; Mukai et al. 2005), a well known state changing source, r1-25 is not ultraluminous. r1-25 is unique in that no such sources are known in the Galaxy or Magellanic Clouds. We examined all available *Chandra*, *Swift*, and optical data from Hubble Space Telescope (HST) and the Local Group Survey (LGS) for this source. We also checked the literature for *XMM-Newton* observations and analysis of the source. The question we want to answer is: what is the physical nature of this unique source?

We analyze the X-ray data for the source in §2.2. In §2.3, we present evidence that the source changes state. In §2.4, we analyze the optical data. We discuss the possible models that fit this source in §2.5.

2.2 X-ray Observations and Analysis

The source r1-25 has been discussed in the literature (Kong et al. 2002; Williams et al. 2004; Di Stefano et al. 2004a; Kaaret 2002; Voss & Gilfanov 2007; Stiele et al. 2010; Di Stefano et al. 2010b; Orio et al. 2010). It is located in the central region of M31 approximately $0.4'$ (about 91 parsecs) from the nucleus. The coordinates of the source are (J2000.0) RA = 00:42:47.90, DEC = +41:15:49.99. This region of M31 has been well sampled over the past 13 years. For this paper, we searched the *Chandra* archive for all public observations of r1-25 through June 2, 2009. There were 86 observations that covered the source. r1-25 was detected in 45 observations (28 ACIS-I, 2 ACIS-S, and 15 HRC-I observations) from

August 8, 2000 to March 11, 2009. We note that the source position was the same in all detections, and we are confident that r1-25 is one source. We supplemented the *Chandra* data with *Swift* observations of the region in 2009. However, the source was off during the *Swift* observations, which are not included in this paper.

Liu (2011) presented the photometry for the ACIS observations of r1-25 taken between 2000 and 2004. We analyzed the ACIS data taken between 2004 and 2009 using the method presented in that paper. We used CIAO version 4.1.2 (Fruscione et al. 2006) to analyze the recent data. For source detection, we used CIAO tool `wavdetect` (Freeman et al. 2002; Fruscione et al. 2006). Only photons between 0.3-7 keV were considered and the following bands were used to classify them: Soft, 0.3-1.1 keV; Medium, 1.1-2 keV; and Hard, 2-7 keV. We note that there were no photons detected below 0.3 keV. The total count rate, as well as the rate in each band, were corrected by a vignetting factor. The vignetting factor was derived from the exposure map as the ratio between the local and the maximum map values.

For HRC-I observations, we used the CIAO tool `dmextract` (Fruscione et al. 2006) to extract raw counts in source and background apertures, as shown in Figure 2.1, and to compute net counts. We defined aperture sizes so that the source aperture encircled energy fraction was $\sim$1 and the background aperture fraction 0. We also used the CIAO `aprates` (Fruscione et al. 2006) tool to compute the background-marginalized posterior probability distribution for the source rates, assuming non-informative prior distributions for source and background rates (Kashyap et al. 2009). We note that the HRC data were not corrected for vignetting. Thus, the rates are lower than the ACIS counterparts by 10% or less. For observations with low flux significance, we used the posterior probability distributions to estimate the 3σ upper limits to the rate. The upper limits were calculated using `aprates` and the same method was applied to both HRC and ACIS observations.

Table 2.1 shows the photometry results for r1-25. Columns 4, 5, and 6 show the Soft, Medium, and Hard count rates, respectively. The uncertainties are 1σ in size and calculated

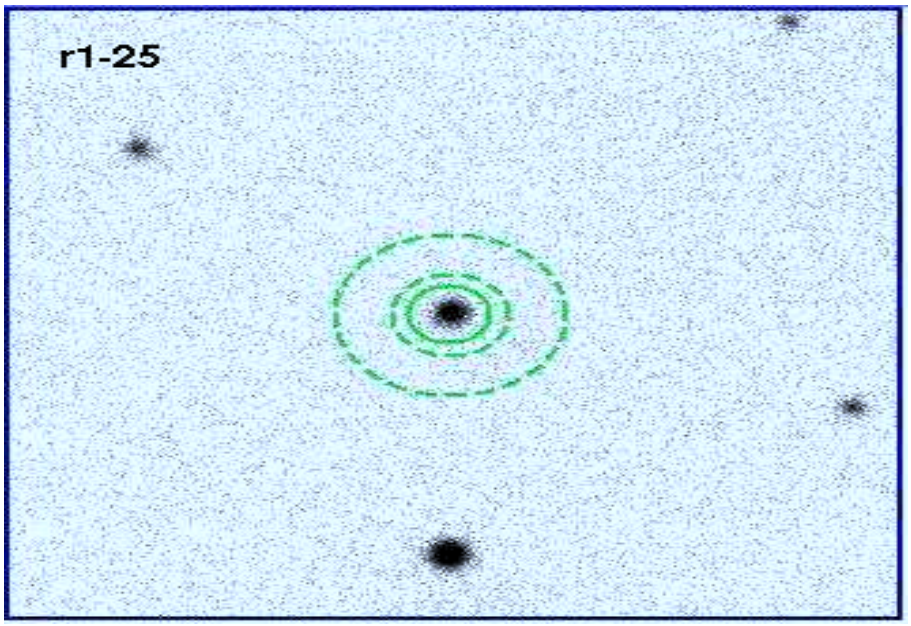

Figure 2.1 Source (solid) and background (dashed) apertures for r1-25, displayed on a ∼432 kilosecond merged Chandra HRC-I observation of M31.

using Poisson statistics. Figure 2.2 shows the light-curve for r1-25. The top panel shows the count rate in each band (soft, medium, and hard) vs. obsdate for the ACIS-I detections; it demonstrates that the relative count rates change over time for the source. The bottom panel of Figure 2.2 shows the total count rate in the ACIS-I band vs. obsdate. We used the `pimms` (Mukai 1993) to convert ACIS-S and HRC-I count rates to ACIS-I units. We choose ACIS-I units because most of the detections of the source were in this instrument. We indicate ACIS-S and HRC-I observations as a range of values, and assumed $N_H = 1.1 \times 10^{21}$ cm^{-2} for the conversion. For OBSID 1854, we assumed a thermal blackbody model with temperatures of 75 and 83 eV to determine the lower and upper limits of the range, respectively. For OBSID 1575, we used $kT = 120$ eV and $kT = 150$ eV to determine the range with the same column. For HRC-I detections and upper limits, as well as ACIS-S upper limits, we converted to ACIS-I units using $kT = 75$ eV and $kT = 300$ eV.

2.3 Evidence for State Change

We used the CIAO tool *dmextract* to create source spectra for all observations where more than 60 source counts were collected. Source spectra were extracted from a circular region with radius 6 pixels centered on the source. Associated background spectra were extracted from an annular region (also centered on the source) with inner and outer radii of 10 and 25 pixels, respectively. For all observations, we created spectral response files using the CIAO tasks *mkacisrmf* and *mkarf* (Fruscione et al. 2006).

We modeled the resulting spectra using the XSPEC package (Arnaud 1996). Since the number of source counts is small, we fit the spectra (binned to have one count per bin, as suggested in the XSPEC documentation) using the C-statistic (Cash 1979) rather than the χ^2 statistic, which has been shown to introduce a systematic bias in parameter estimation in low count rate spectra. The C-statistic as implemented in Xspec models the source and background spectrum simultaneously, scaling the background spectrum channel

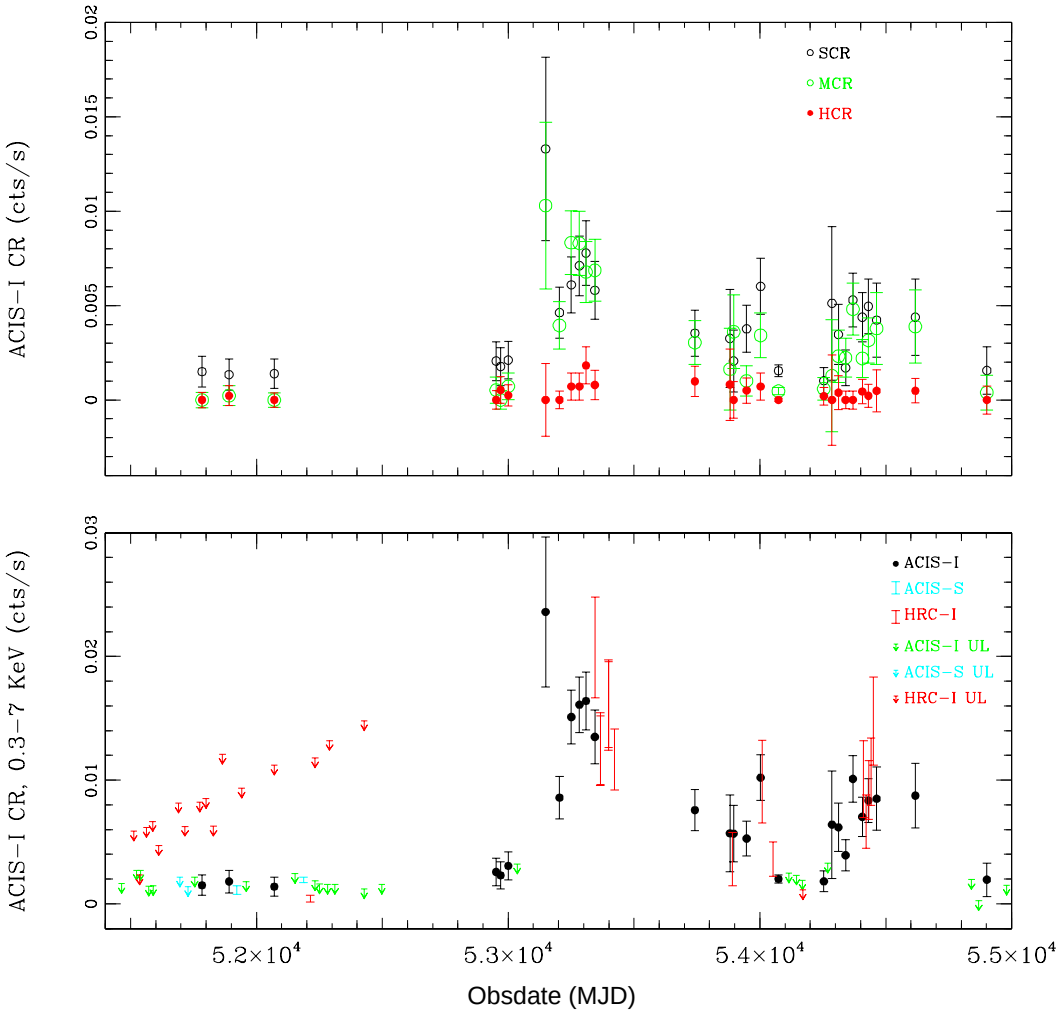

Figure 2.2 Light-curve for r1-25. *Top Panel:* Count Rate in the Soft (0.3-1.1 keV), Medium (1.1-2 keV), and Hard (2-7 keV) bands vs. Obsdate. *Bottom Panel*: Total count rate in ACIS-I units (in the energy range of 0.3-7 keV) vs. Obsdate. See text for how we converted ACIS-S and HRC-I observations to ACIS-I units.

by channel to the size of the source region [1]. One σ uncertainties were estimated using the error command. We found that model fits to observations with less than 60 counts were not constrained; for this reason, we do not include them in our spectral analysis of r1-25. The four Obs-IDs with more than 60 counts were: 1575 (ACIS-S, 183 source counts), 4720 (ACIS-I, 61 source counts), 4721 (ACIS-I, 65 source counts) and 4722 (ACIS-I, 62 source counts).

We fit a simple absorbed blackbody model to each spectrum in the energy range 0.3-8.0 keV, using the wabs model for the interstellar absorption (Morrison & McCammon 1983). None of the spectra had enough counts below 1 keV to place a tight constraint on the interstellar column density (in several cases the fits were consistent with no absorption), so we fixed N_H at two values representative of the range expected towards an X-ray source in M31 (1.1×10^{21} and 6.4×10^{21} cm^{-2}). The lower limit was taken from Di Stefano et al. (2004a). The upper limit is shown for completeness; it is very unlikely that the source has such a large column density. The resulting parameter values and their 1 σ uncertainties are presented in Table 2.2. We note that our results for ObsID 1575 (we found 0.110 keV $\leq kT \leq$ 0.130 keV) are consistent with those reported in Di Stefano et al. (2004a) (they found that $kT = 0.122$ keV). Examining the temperatures found for r1-25, a clear increase in the later observations can be seen, independent of the choice of absorbing column. Furthermore, r1-25 significantly changes in luminosity when it changes state. At the 90% confidence level, the temperature found for the ACIS-S spectrum is $\sim$0.1 keV lower than the ACIS-I values. The blackbody temperature returned by the model fitting is constrained primarily by the high energy cut off. Although ACIS-I has poorer low energy sensitivity, the fact that significantly harder counts are detected in such short exposures indicates that the increase in model temperature is real and independent of the differences between the two ACIS instruments.

[1] See http://heasarc.nasa.gov/xanadu/xspec/manual/XSappendixStatistics.html

2.4 Optical Observations and Analysis

The location of r1-25 has been observed with the ACS camera onboard *HST*. The source has been observed 4 times: on 2004-01-23 (observation j8vp03010) for 2200 seconds, 2004-08-15 (observation j8vp05010) for 2200 seconds, 2006-02-10 (observation j9ju01010) for 4360 seconds, and 2007-01-10 (observation j9ju06010) for 4672 seconds. Images are only available in the F435W filter (approximately equal to the B filter in ground based systems). Only one *Chandra* observation (ObsID 8183) was taken within a week of an ACS observation (j9ju06010) of the source. However, the source was not detected in ObsID 8183.

All data were obtained using the Wide Field Channel (WFC), which has a $202'' \times 202''$ field of view (Maybhate 2010). Each observation was carried out in the standard four pointing dither pattern (Maybhate 2010). These individual images were then combined using the PyRAF task MultiDrizzle (Fruchter & et al. 2009), which also removes cosmic rays and corrects the geometrical distortion which results from the orientation of the ACS with respect to the HST focal plane. We chose not to apply an automatic background subtraction in order to perform photometry, since there is a steep gradient in the diffuse light this close to the center of M31 making background estimation unreliable. Finally, we utilized the ability of MultiDrizzle to resample the spatial scale of the image, resulting in a final pixel scale of $0.025''$/pix.

The World Coordinate System (WCS) in HST images can be offset from standard reference frames by as much as one arcsecond (Maybhate 2010). To improve the astrometry, we registered the final drizzled images to the WCS of the Local Group Survey (LGS) images of M31 (Massey et al. 2006). Stars common to both images were identified, and their centroid positions calculated using the IRAF task imcentroid. We then used the task ccmap in IRAF to update the WCS of the HST images. The final rms (1σ) errors in the alignment were of order $0.006''$ in RA, and $0.002''$ in declination. We note that the RMS errors on the alignment of the HST images to the WCS of the LGS survey were always smaller than

$0.01''$ (which is smaller than one pixel in the rescaled images).

We also aligned the deepest *Chandra* observation (ObsID 1575) with the WCS of the LGS images using the same procedure applied to the HST images. We found an alignment error of $0.109''$ in RA and $0.149''$ in DEC. The centroid position in the corrected WCS for the source is RA:00:42:47.90, DEC:+41:15:49.99, with errors of $0.08''$ (RA) and $0.07''$ (DEC). To get the final positional error, we added the alignment and centroid errors in quadrature. The final RA error is $0.13''$ and final DEC error is $0.17''$ (these are 1σ errors).

Since the WFC images cover such a large area and contain so many stars, we extracted subimages 1000 pixels on a side centered on our source of interest and performed photometry on those. We used the DAOPHOT II and ALLSTAR routines (Stetson et al. 1990) to find and photometer stars in the images. Stars suitable for calculating a point spread functions (PSFs) were identified by hand to avoid problems due to crowding. The final measured counts for each star were converted first to count rate by dividing by the exposure time of each observation, and then to AB system magnitudes using the conversion factors in the ACS users handbook (Maybhate 2010).

We show the final reduced image for the source in Figure 2.3, superimposed with the X-ray 3σ positional error ellipse. The ellipse is drawn using the 3σ RA error ($0.39''$) as the semi-major axis and the 3σ DEC error ($0.51''$) as the semi-minor axis. The location of r1-25 is extremely crowded, and being so close to the core is subject to a high background of diffuse light. In our series of four images, two (j9ju01010 and j9ju06010) are also significantly deeper, which affects the completeness of the stars we can detect. The small size of the Chandra error circle does however simplify the analysis of the photometry, since very few sources are inside the X-ray 3σ error ellipse. Examining the images, a number of sources are detected inside the error circle, although most are unresolved. We note that there are no catalog stars within the *Chandra* error ellipse. In fact, only one source is resolved inside the error ellipse in all four images by the photometry source detection algorithm. We have marked this source with a red circle in Figure 2.3.

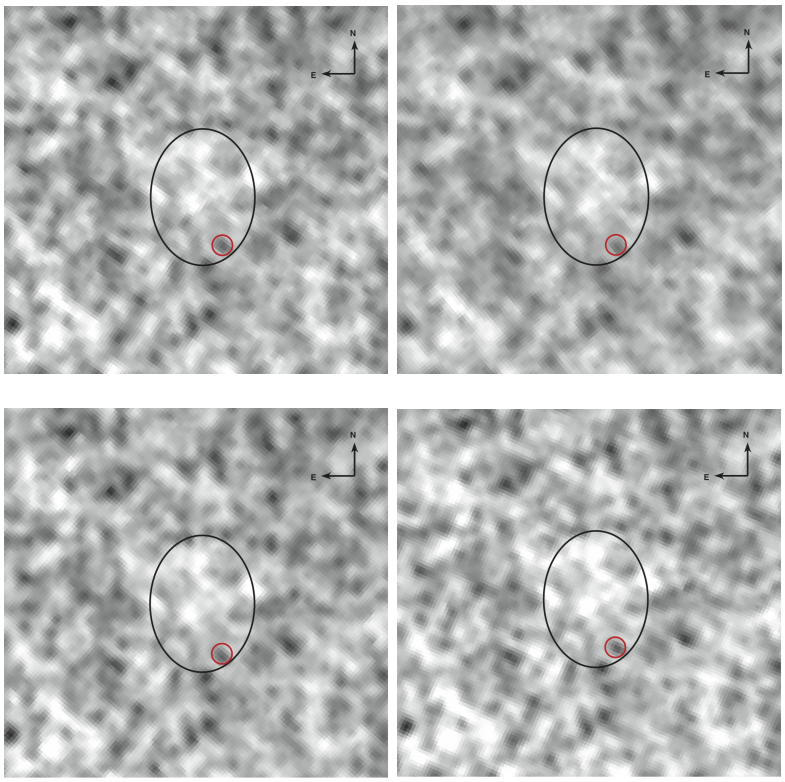

Figure 2.3 HST ACS images of the location of r1-25, obtained in the F435W filter on four separate dates. *Top Left:* Observation j8vp03010, *Top Right:* observation j8vp05010, *Bottom Left:* Observation j9ju01010, *Bottom Right:* Observation j9ju06010. Each image is $3''$ on a side. The black ellipse denotes the 3σ X-ray positional error ellipse of r1-25. The ellipse has a semi-major axis (3σ RA error) = $0.39''$ and a semi-minor axis (3σ DEC error) = $0.51\ ''$. The red circle shows the only consistently detected, resolved source found by DAOphot.

The single resolved source in Figure 2.3 has observed magnitudes of 24.45 ± 0.06, 24.27 ± 0.05, 24.31 ± 0.04 and 24.41 ± 0.04 in each of the four images, where the uncertainties are 1σ in size. Using the standard $E(B-V) = 0.062$ for M31 (Schlegel et al. 1998), the extinction in the F435W filter is 0.785 magnitudes. Thus, the star's M_B is between -0.80 and -0.98 in the four observations, assuming $(m - M)_0 = 24.47$ (Holland 1998). This demonstrates that, within the uncertainties, there is no evidence of variability in this object. Although other sources are picked up by the DAOphot detection algorithm inside the error ellipse in some images, these additional detections can be accounted for by the longer exposure time, or are unreliable due to crowding.

Grupe et al. (2010) looked at the spectral energy distribution of 92 active galactic nuclei that had soft X-ray spectra. The AGN they studied had comparable X-ray count rates to r1-25. However, the AGN were much brighter in the B band ($14 < m_B < 18$) than any source in Figure 2.3. For this reason, we are confident that r1-25 is not an AGN.

With no color information, we cannot determine what the object marked in Figure 2.3 is for certain. If it is a star, it would correspond to a late B type with bolometric luminosity of 10^{36} ergs s^{-1}. We note that it is too luminous in the B band to be a red giant, and too dim to be a red supergiant.

2.5 Models

The state changes observed in r1-25 are extremely unusual for an SSS. In this section, we consider a number of physical models with the goal of uncovering the nature of the X-ray emitting source. In order for any model of r1-25 to be successful, it must be able to explain all of the observed features of the source. These features include the source's appearance as an SSS-HR source in observation 1575 with ACIS-S, with kT $\sim$ 130 eV and a 0.3–8 keV luminosity of 4×10^{36} erg s^{-1}. We wish to emphasize once again that even though r1-25 had an effective temperature in excess of 100 eV when detected as an SSS (much higher than most SSSs), it satisfied the strictest SSS criterion as defined in Di Stefano et al.

(2004a). That is, the detection in observation 1575 (when the source was an SSS) had no hard counts, medium counts consistent with zero, and at least 3σ detection in the soft band.

Furthermore, the model must explain the subsequent detections of the source as a ∼250 eV source, *with higher luminosity* than in the soft state (∼10^{37} erg s^{-1}). Lastly, the model must be consistent with an optical counterpart with F435W magnitude fainter than ∼24.3 (M_B fainter than ∼ -1). We note that white dwarf, neutron star, and black hole SSSs are consistent with this optical constraint. The following subsections outline white dwarf, neutron star and black hole models, and compare their features to the observed properties of r1-25.

2.5.1 White Dwarfs

White dwarfs that have recently experienced novae have temperatures and luminosities that can make them detectable as SSSs.[2] Many SSSs detected in M31 were recent novae (e.g., Pietsch et al. 2005, 2007; Stiele et al. 2010, references therein). When the white dwarf cools, some novae are detected as harder X-ray sources, but the X-ray luminosity is around $10^{32} - 10^{33}$ ergs s^{-1} (Sala et al. 2010). In contrast, novae in a supersoft state are detected with $kT \sim 50$ eV and L_X of $10^{37} - 10^{38}$ ergs s^{-1} (e.g., Stiele et al. 2010, references therein). Thus r1-25, even in its softest state (with kT ∼130 eV and L_X of 4×10^{36} erg s^{-1}), is too hard to be consistent with the very soft emission detected in typical supersoft novae. Also, the source is not consistent with the harder states of novae. That is r1-25 in its hardest state (∼250 eV and L_X of 1.1×10^{37} erg s^{-1}) is softer and more luminous than novae in their hard states. Moreover, unlike novae, the harder states of r1-25 are more luminous than its soft state. We therefore turn to models in which a white dwarf accretes matter at high rates.

When a white dwarf accretes mass at a high enough rate that the incoming matter can

[2] A specific post-nova system will be detectable as an SSS only if the white dwarf stays hot enough to be emitting as an SSS until after the optical depth has decreased enough to let radiation escape (e.g., Sala & Hernanz 2005).

experience nuclear burning, the white dwarf can appear as an SSS. In this case, the source will not be in a hard state. The copious energy we receive from such sources is provided by nuclear burning, rather than accretion. The effective radii are comparable to the white dwarf radii, so the emission can be characterized by values of kT in the range of tens of eV for low-mass white dwarfs, and ~ 100 eV for white dwarfs approaching the Chandrasekhar mass (M_C). For each white dwarf mass, nuclear burning can occur only within a narrow range of accretion rates (Nomoto 1982; Iben 1982; Fujimoto 1982; Shen & Bildsten 2008, references therein). These rates are very high: $\sim 10^{-7} M_\odot$ for a solar-mass white dwarf, ten times higher for a white dwarf with mass near M_C (Di Stefano 2010a). At such rates of infall, accretion alone produces luminosities in the range of $10^{36} - 10^{37}$ ergs s^{-1}, typically a few percent of the total energy of the system.

Consider a case, when its accretion rate places a white dwarf near the lower end of the steady-burning region, or just below it. In this case, nuclear burning may be episodic. During and just after nuclear-burning episodes, the emission is dominated by soft emission. As the white dwarf cools, however, it becomes less luminous and the emission is dominated by accretion. Although at high rates of accretion, the emission is expected to be softer than typical for low-accretion-rate white dwarfs, such as cataclysmic variables, it can nevertheless be harder than typical of SSSs (e.g., Popham & Narayan 1995; Patterson & Raymond 1985). Thus, the source could appear to be quasisoft or hard. If the donor is a giant or a Roche-lobe filling star in a circular orbit, the accretion rate should could continue to be high. The source will continue to be detected as a harder source. Nuclear burning episodes occurring at intervals ranging from months to decades would make the source more luminous and detectable as an SSS.

The points made above about the quasi-steady nuclear burning white dwarf model are illustrated in Figure 2.4. The figure is a plot of kT vs. the logarithm of bolometric luminosity, LOG[L] for various quasi-steady nuclear burning white dwarfs (green points) along with the r1-25 spectra (black and blue points). The points represent the XSPEC

spectral fits of r1-25 shown in Table 2.2. The solid black points represent the fits where we assume L_X = L. The X-ray luminosity, however, is not equivalent to the bolometric luminosity. We assume that the X-ray luminosity represents, at least a quarter of the bolometric luminosity. Thus, we plot the open blue circles which represent XSPEC fits assuming $L_X = 0.25L$. The plot clearly indicates that the quasi-steady nuclear burning white dwarf model does not fit r1-25, as the data are too hard and/or dim to fit the model. That is, none of the XSPEC points fall in the range of quasi-steady nuclear burning white dwarf.

2.5.2 Neutron Stars

Isolated neutron stars and neutron stars in quiescent low-mass X-ray binaries (qLMXBs) have been observed with spectra in the SSS or QSS range, but they are typically 3-5 orders of magnitude less luminous than the "classical" SSSs and QSSs (e.g., Haberl 2007; Pires et al. 2009). Neutron stars accreting at high rates, however, have luminosities in the range (above 10^{36} erg s^{-1}) observed for SSSs and QSSs. But, at the time SSSs were discovered, all known accreting neutron stars emitted hard x-rays. The lack of hard emission from SSSs therefore seemed to be more easily accommodated in white dwarf models.

Nevertheless, Kylafis & Xilouris (1993) showed that accreting neutron stars can be observed as SSSs under the right circumstances. They considered near-Eddington accretion through a disk. Radiation pressure from the inner disk can push some plasma into an "extensive outer disk corona." If the corona extends to large enough radii, and if it is optically thick, the neutron star will radiate as an SSS. Indeed, there is observational support for the idea that neutron stars can produce very soft spectra. For example, Hughes (1994) discovered a transient pulsar in the Small Magellanic Cloud that has an unpulsed, highly luminous (near Eddington) soft $\sim$ 35 eV component. If such a system were to be viewed from an angle at which the hard radiation is not detected, it would have the properties associated with the "classical" SSSs first discovered in the Magellanic Clouds (Long et al.

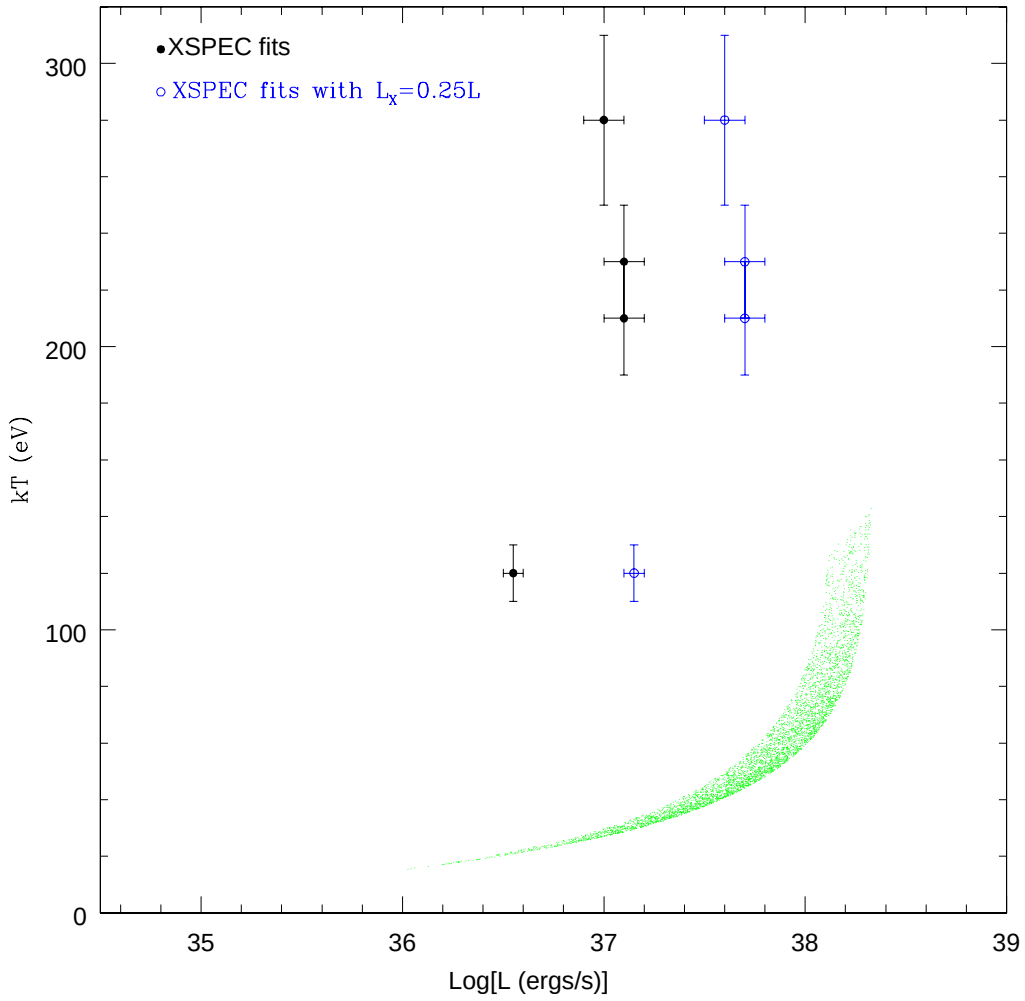

Figure 2.4 Plot of kT vs. the logarithm of the bolometric luminosity, LOG[L]. The black and blue points show the observations with XSPEC fits from Table 2.2 (assuming $N_H = 1 \times 10^{21}$ cm^{-2}). The solid black points represent XSPEC fits assuming $L_X = L$, and the open blue points assume $L_X = 0.25L$. The green points represent the kT and LOG[L] for various quasi-steady nuclear burning white dwarfs.

1981).

Although the details of the model considered by Kylafis & Xilouris (1993) may not apply to all systems, their work, combined with observations, indicates that neutron star models must be considered. Yet, beyond the success of the white-dwarf models, there is another reason that neutron star models have not been popular, and that was alluded to by Kylafis & Xilouris (1993). This can be simply stated by saying that the physics determining the size of the photosphere was put in by hand. Thus, the solutions for radial flows that extend out to *at least* a few thousand neutron star radii produce SSS-like behavior, and radial flows that extend out to *at most* a few hundred neutron star radii produce more standard LMXB-like behavior. The range of photospheric radii between these two extremes would be associated with luminous emitters of thermal radiation with kT in the range between roughly 100 eV and a few hundred eV; that is, the sources would be QSSs, which had not yet been discovered.

Here we point out that the discovery of QSSs provides reasons to revisit neutron star models, eliminating the need for fine tuning problem that Kylafis & Xilouris (1993) encountered. The key issue to address is what determines the size of the photosphere. It is likely to be linked to accretion rate, with higher rates capable of producing larger photospheres, as in the Kylafis & Xilouris (1993) model. Here we suggest that in some cases, the edge of the magnetosphere could roughly correspond to the photosphere. If this is the case, then, given that the mass, radius, and magnetic field of the accretor are all roughly constant over time scales of months to years, the photospheric radius would be driven primarily by changes in the accretion rate. Equation (1) and Figure 2.5 show the relationship that would be predicted between the temperature and luminosity.

Consider a neutron star producing near-Eddington soft emission. If this emission emanates from a nearly spherical photosphere with radius equal to the Alfven radius, then

$$kT = 100.4\,\mathrm{eV}\left(\frac{10^{11}\mathrm{G}}{B_s}\right)^{\frac{2}{7}}\left(\frac{10\,\mathrm{km}}{R_{NS}}\right)^{\frac{5}{7}}\left(\frac{M_\odot}{M}\right)^{\frac{1}{14}}\left(\frac{L}{10^{37}\mathrm{ergs\,s^{-1}}}\right)^{\frac{11}{28}} \qquad (2.1)$$

In this expression, R_{NS} is the radius of the neutron star, B_s is the value of magnetic field on the surface, and M and L represent the neutron star's mass and luminosity, respectively. We derive this expression from equation 11 in Ostriker & Davidson (1973).[3] An interesting feature of this expression is that there are ranges of reasonable values of the physical parameters in which the kT is in the range expected for SSSs or QSSs. Furthermore, for a specific neutron star, the effective temperature depends on L which can change as the accretion rate changes. Since changes in accretion rate are common, we may therefore expect the effective temperatures of some neutron stars to change. Depending on the physical parameters, these changes could produce transitions from SSS to QSS states.

Figure 2.5 shows two plots of kT vs. LOG[L]. The top panel shows several curves which differ from each other in the value of B_s, which changes by a factor of ten between curves, as shown. The bottom plot shows the r1-25 spectra along with the $B_s = 10^{10}$ G curve. The black points represent the XSPEC fits shown in Table 2.2. The plots were made in the same manner as in Figure 2.4 (see §2.5.1), except that we assumed neutron star models have L $\approx$ L_X. Figure 2.5 shows that the distribution of points is roughly consistent with what is expected for the neutron star model discussed above. The XSPEC points seem to follow the same trend as the curve, with some variation.

The general agreement between the trend of increasing kT with increasing luminosity is promising, and neutron-star models in which the photospheric radius is not governed by the size of the Alfven radius may follow similar trends, with kT increasing with luminosity. Nevertheless, this general trend is not unique to neutron star models, as we will see in §2.5.3, where black hole models are considered. It is therefore important to develop observational criteria that can identify the nature of the compact accretor.

For example, the neutron-star natures of LMXBs in the Galaxy's globular clusters have been verified through the detections of both bursts (e.g., Lewin et al. 1993) and pulsed (e.g.,

[3]The form we show in equation 2.1 uses the equation for the mass accretion rate, $\dot{M}_{acc} = \frac{L_{acc} R_{NS}}{GM}$, and the blackbody luminosity equation, $L = 4\pi\sigma(r_a)^2 T^4$. In these equations, r_a is the Alfven radius and T is the blackbody temperature.

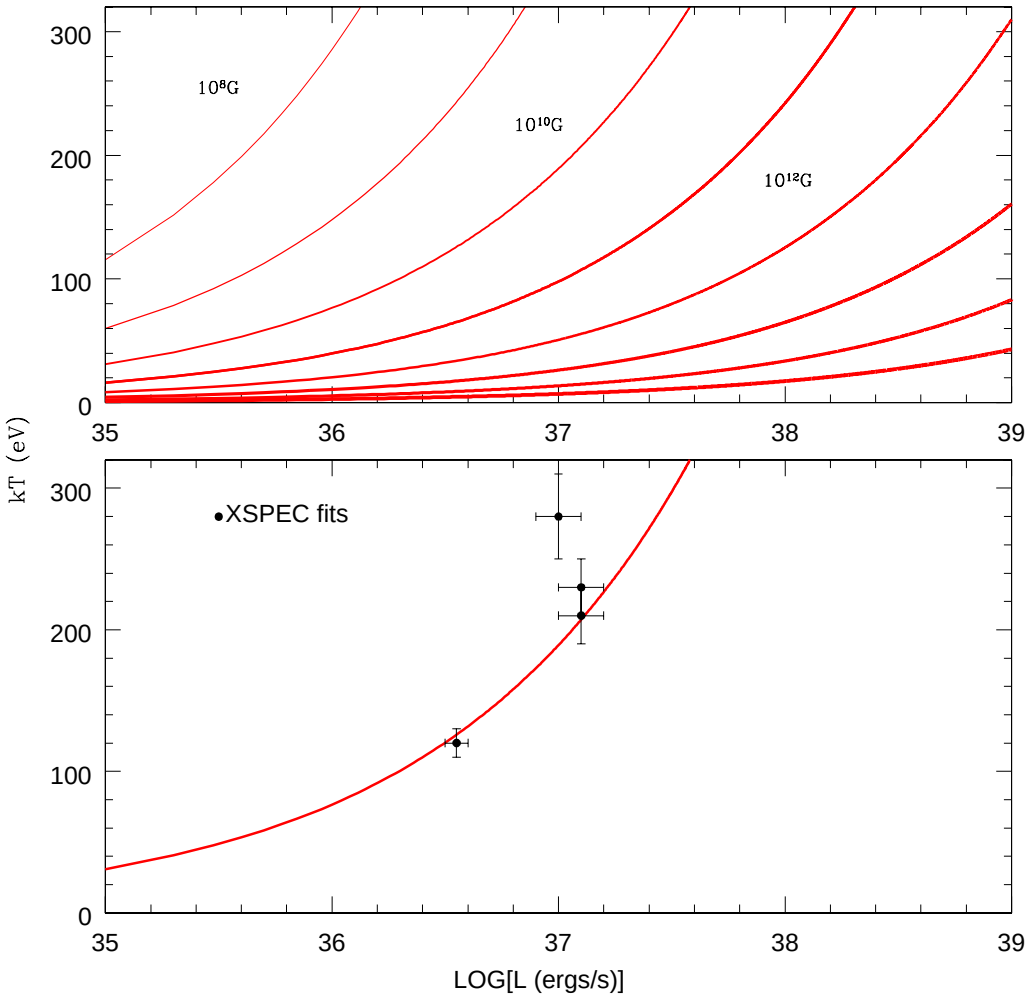

Figure 2.5 Plot of kT versus L for the neutron star model described by Equation 1. *Top Panel:* Each curve corresponds to a fixed value of the magnetic field on the surface of the neutron star; B_s changes by a factor of ten between curves. Since the field is not expected to vary this much over short times, the system should evolve *along* the curves. Thus, if the luminosity increases or decreases, so does the temperature. *Bottom Panel:* The $B_s = 10^{10}$ G curve is plotted with the r1-25 spectra. The black points represent XSPEC fits from Table 2.2 (assuming $N_H = 1 \times 10^{21}$ cm^{-2}).

Zhelezniakov 1981) radiation. Both types of variable components are expected to be harder than the dominant softer radiation from an extended photosphere. Thus, for example in an x-ray pulsar, the diagnostic for the neutron star model would be periodicity in the arrival times of the harder photons. If, therefore, we can identify QSSs and state changers in the Milky Way or in the Magellanic Clouds, we can test models by searching for evidence of hard bursts or pulses. Detecting these in state changers, or in QSSs, would be possible if the system is close enough, and would verify the neutron-star nature of the accretor.

2.5.3 Black Holes

Accreting black holes can exhibit thermal-dominant states in which the emission is dominated by a component emanating from the inner portion of the accretion disk (e.g., Remillard & McClintock 2006). SSSs and QSSs have therefore both been suggested as possible black holes. In fact, the most well-known state changer is M101-ULX-1, an ultraluminous SSS that has been detected also in high QSS and low-hard states (e.g., Kong et al. 2004; Kong & Di Stefano 2005; Mukai et al. 2005). M101-ULX-1 is almost certainly a black hole. Its mass could be either in the range typical of Galactic stellar-mass black holes or else in the higher range ($50 - 10^4\,M_\odot$) suggested for intermediate-mass black holes.

The luminosity of r1-25 is 1-3 orders of magnitude smaller than the luminosities measured for M101-ULS-1 when it is in a soft state. It is therefore highly unlikely to be an intermediate-mass black hole. In fact, if the luminosity is less than roughly a percent of the Eddington luminosity, then the inner disk will not be optically thick and the emission will not be thermal. This suggests that, if this source is a black hole, it is more likely to be of stellar mass. The top panel of Figure 2.6, first shown in Di Stefano et al. (2010b), shows that QSS emission is expected in the thermal-dominant state of black holes with mass below $\sim 100\,M_\odot$. The radius of the inner disk would determine the value of the effective temperatures; the spectrum could be either QSS or SSS. At lower rates of accretion, the emission would be hard. Note that there are two curves for each mass; the top curve assumes the

inner portion of the accretion disk is at $6MG/c^2$ ($3r_s$, where r_s is the Schwarzschild radius) and the bottom assumes $18MG/c^2$ ($9r_s$). Note that that the top curve (at $3r_s$) represents the maximum luminosity and temperature for this model in which the radiation comes from the inner disk.

Figure 2.6 shows the r1-25 spectra along with the $10M_\odot$ and $100M_\odot$ curves. The black points representing the XSPEC fits shown in Table 2.2 were plotted in the same manner as in Figure 2.5 (see §2.5.2). The distribution of the points with XSPEC fits is roughly consistent with what is expected for a black hole of roughly $10M_\odot$.

2.6 Conclusion

We have tracked the long-term behavior of the M31 X-ray source r1-25. First observed by ROSAT on 1990-07-24, then by both *Chandra* and *XMM-Newton*and most recently by Swift, r1-25 is one of the best-studies soft X-ray sources. There are 86 public *Chandra* observations of the source through June 2, 2009, with 45 detections. For *XMM-Newton*, there are 26 public observations of the source, with Stiele et al. (2010) reporting detections in only the 2004 data. The detections of the source start in 1999 and continue through 2009.

By doing this we have documented the fact that r1-25 has transitioned from an SSS to a harder, QSS state. In the SSS state its estimated X-ray luminosity is a few times 10^{36} ergs s^{-1}, and the luminosity appears to be higher, but not much over 10^{37} ergs s^{-1} in the harder state. Only one other X-ray source, M101-ULX-1, has well-studied state changes (e.g., Kong et al. 2004; Kong & Di Stefano 2005; Mukai et al. 2005). While M101-ULX-1, which has been observed with X-ray luminosity as high as $10^{40} - 10^{41}$ ergs s^{-1}, is almost certainly a black hole, the nature of r1-25 is more difficult to establish, because its luminosity range is consistent with white dwarf, neutron star, or black hole accretors.

Whatever its nature, its behavior is different from anything we have observed. We have shown that the observed behavior is consistent with a black hole accretor with a mass

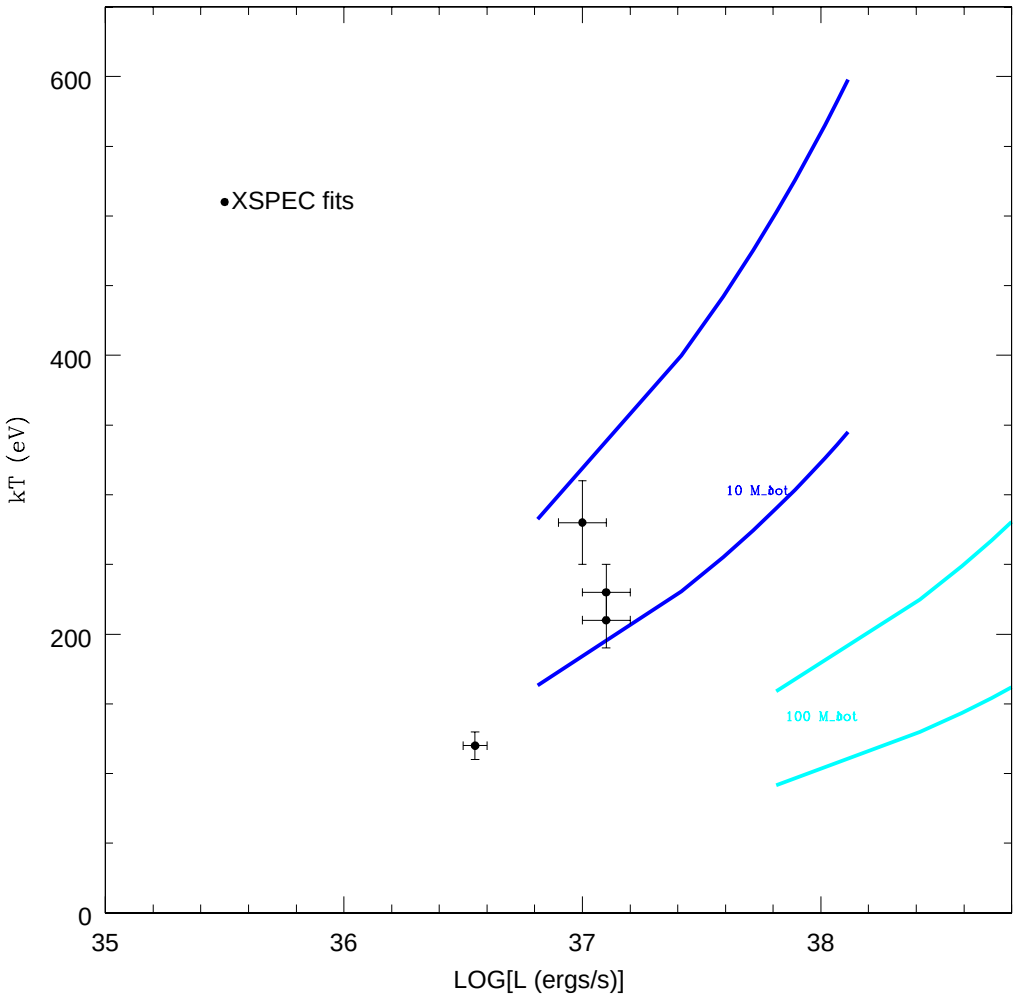

Figure 2.6 Figure taken from Di Stefano et al. (2010b). It is a plot of kT versus LOG[L] for the inner portion of the accretion disk around black holes. Each pair of two curves of a single color corresponds to a fixed black hole mass which labels the regions between the curves. The upper curve of each color corresponds to a disk with inner radius $6M_{BH}G/c^2$ ($3\mathrm{r}_s$), while the lower curve corresponds to an inner disk with $9\mathrm{r}_s$. The point at the bottom (top) of each curve corresponds to the luminosity of the inner disk being $1\%L_{Eddington}$ ($10\%L_{Eddington}$). The curves are plotted with the r1-25 spectra. The black points represent the XSPEC fits from Table 2.2 (assuming $N_H = 1.1 \times 10^{21}$ cm^{-2})

in the $10M_{\odot}$ range. In this case, our observations of r1-25 have all found it to be in a thermal-dominant state. The inner disk radius would have been larger in the SSS state. If r1-25 is a black hole with a mass of approximately $10M_{\odot}$, it could be more luminous in future observations, if the donor star is able to contribute mass at a higher rate. Should the luminosity approach the Eddington luminosity, the system would be unlikely to remain in the thermal dominant state, and hard emission could be detected. Similarly, if the luminosity falls below $\sim 1\%$ of the Eddington value, the spectrum would likely be hard.

We have also shown that the observed behavior of r1-25 is consistent with a neutron star accretor with $B_s = 10^{10}$ G. We assume that the magnetic field should be constant over the short interval of observations of the source. The model suggests that the harder states are more luminous than the softer ones, which is consistent with the r1-25 spectra. We note that neutron star models are testable if we can find state changers and QSSs in the Milky Way or Magellanic Clouds, as both bursts and pulsed radiation would be detectable in nearby neutron stars.

White dwarf models are the least likely fit for r1-25. The source does not seem to exhibit behavior of a post-nova system, as its spectrum is harder than novae that are SSSs (even when r1-25 is in its soft state). The source is also too luminous and soft to be consistent with novae in their harder states. Furthermore, quasi-steady nuclear burning white dwarf models do not fit the data. We have shown that quasi-steady nuclear burning models can produce both supersoft and quasisoft radiation, but the model is too soft and/or luminous to fit the r1-25 spectra.

We note that there are other state-changing sources in external galaxies.[4] For example, there are nine state changing sources in nearby spiral galaxy M33. If we study a large enough sample of state-changers, we are likely to find examples of all three (white dwarf, neutron star, and black hole) models. Continued monitoring of these sources will play an important role in testing these models. It is also important to identify QSSs and state-changers in

[4]see http://www.cfa.harvard.edu/∼jfliu/ for a list of state changing sources

the Magellanic Clouds and Galaxy, where many test of the nature of the accretors can be conducted.

We would like to thank the *Swift* team for approving our ToO request (Target ID: 35336). This research has made use of the NASA/IPAC Extragalactic Database (NED) which is operated by the Jet Propulsion Laboratory, Caltech, under contract with the National Aeronautics and Space Administration. This research was supported by HST Grant AR-10948.01-A-0 and the Smithsonian Institution IR & D award. BP is supported at Rutgers University in part by NSF award AST-0847157. We would like to thank the anonymous referee for comments that have helped to improve the paper.

Table 2.1: Photometry for r1-25

ObsID	Date (MJD)	Exposure Time (s)	SCR $10^{-3}s^{-1}$	MCR $10^{-3}s^{-1}$	HCR $10^{-3}s^{-1}$	TCR $10^{-3}s^{-1}$	Total Counts
ACIS-I Observations							
312	51783.8	4666	1.5 ± 0.8	0.0 ± 0.4	0.0 ± 0.4	1.5 ± 0.8	7 ± 4
1581	51891.1	4404	1.3 ± 0.8	0.2 ± 0.5	0.2 ± 0.5	1.8 ± 0.9	8 ± 4
1583	52070.8	4903	1.4 ± 0.8	0.0 ± 0.4	0.0 ± 0.4	1.4 ± 0.8	7 ± 4
4678	52952.3	3894	2.1 ± 1.0	0.5 ± 0.7	0.0 ± 0.5	2.6 ± 1.1	10 ± 4
4679	52969.9	3820	1.8 ± 1.0	0.0 ± 0.5	0.5 ± 0.7	2.3 ± 1.1	9 ± 4
4680	53000.3	4198	2.1 ± 1.0	0.7 ± 0.7	0.2 ± 0.6	3.1 ± 1.1	13 ± 5
4682	53148.7	3945	13.3 ± 4.9	10.3 ± 4.4	0.0 ± 1.9	23.6 ± 6.1	23 ± 6
4719	53203.9	4123	4.6 ± 1.4	3.9 ± 1.3	0.0 ± 0.5	8.6 ± 1.7	35 ± 7
4720	53250.6	4108	6.1 ± 1.5	8.3 ± 1.7	0.7 ± 0.7	15.1 ± 2.2	62 ± 9
4721	53282.9	4132	7.1 ± 1.6	8.3 ± 1.7	0.7 ± 0.7	16.1 ± 2.2	66 ± 9
4722	53309.1	3894	7.8 ± 1.7	6.8 ± 1.6	1.8 ± 1.0	16.4 ± 2.3	63 ± 9
4723	53344.4	4035	5.8 ± 1.5	6.9 ± 1.6	0.8 ± 0.8	13.5 ± 2.2	51 ± 8
7136	53741.8	3991	3.5 ± 1.2	3.0 ± 1.2	1.0 ± 0.8	7.6 ± 1.7	30 ± 7
7137	53881.2	3952	3.3 ± 2.6	1.6 ± 2.2	0.8 ± 1.9	5.7 ± 3.1	7 ± 4
7138	53895.7	4107	2.1 ± 1.6	3.6 ± 1.9	0.0 ± 1.0	5.7 ± 2.3	11 ± 4
7139	53947.0	3987	3.8 ± 1.2	1.0 ± 0.8	0.5 ± 0.7	5.3 ± 1.4	21 ± 6
7140	54002.8	4117	6.0 ± 1.5	3.4 ± 1.2	0.7 ± 0.7	10.2 ± 1.9	42 ± 8
7064	54073.9	23238	1.5 ± 0.3	0.5 ± 0.2	0.0 ± 0.1	2.0 ± 0.3	46 ± 8
7068	54253.9	7693	1.0 ± 0.7	0.6 ± 0.6	0.2 ± 0.5	1.8 ± 0.8	9 ± 4
8192	54286.5	4073	5.1 ± 4.1	1.28 ± 3.0	0.0 ± 2.4	6.4 ± 4.4	5 ± 3
8193	54312.1	4129	3.5 ± 1.6	2.3 ± 1.4	0.4 ± 0.9	6.2 ± 2.0	16 ± 5
8194	54340.5	4033	1.7 ± 0.9	2.2 ± 1.0	0.0 ± 0.5	3.9 ± 1.3	16 ± 5

Table 2.1: Photometry for r1-25

ObsID	Date (MJD)	Exposure Time (s)	SCR $10^{-3}s^{-1}$	MCR $10^{-3}s^{-1}$	HCR $10^{-3}s^{-1}$	TCR $10^{-3}s^{-1}$	Total Counts
8195	54369.6	3965	5.3 ± 1.4	4.8 ± 1.4	0.0 ± 0.5	10.1 ± 1.9	40 ± 7
8186	54407.2	4134	4.4 ± 1.3	2.2 ± 1.0	0.5 ± 0.7	7.0 ± 1.6	29 ± 6
8187	54431.2	3837	5.0 ± 1.4	3.2 ± 1.2	0.2 ± 0.6	8.3 ± 1.8	32 ± 7
9520	54463.7	3962	4.2 ± 2.0	3.8 ± 1.9	0.5 ± 1.1	8.5 ± 2.6	18 ± 5
9529	54617.5	4113	4.4 ± 2.0	3.9 ± 1.9	0.5 ± 0.7	8.8 ± 2.6	18 ± 5
10553	54901.6	4104	1.6 ± 1.3	0.4 ± 0.9	0.0 ± 0.7	2.0 ± 1.3	5 ± 3
ACIS-S Observations							
1854	51922.4	4694	4.3 ± 1.2	0.7 ± 0.6	0.0 ± 0.4	4.9 ± 1.3	23 ± 6
1575	52187.0	37664	4.6 ± 0.4	0.4 ± 0.1	0.0 ± 0.1	4.9 ± 0.4	184 ± 15
HRC-I Observations							
1912	52214.0	46732	···	···	···	0.5 ± 0.1	21 ± 6
5925	53345.8	46311	···	···	···	14.6 ± 0.6	678 ± 28
6177	53366.3	20038	···	···	···	8.8 ± 0.7	176 ± 13
5926	53366.8	28268	···	···	···	8.7 ± 0.6	246 ± 16
6202	53398.1	18046	···	···	···	11.3 ± 0.8	204 ± 14
5927	53398.8	27000	···	···	···	11.4 ± 0.7	308 ± 18
5928	53422.7	44856	···	···	···	8.2 ± 0.4	369 ± 20
7283	53891.3	19942	···	···	···	3.4 ± 0.4	67 ± 9
7284	54008.9	20002	···	···	···	10.6 ± 0.7	212 ± 14
7285	54052.3	18517	···	···	···	3.8 ± 0.5	70 ± 9
8526	54411.6	19944	···	···	···	9.6 ± 0.7	191 ± 14
8527	54421.8	19981	···	···	···	6.3 ± 0.6	126 ± 12
8528	54432.8	19975	···	···	···	7.7 ± 0.6	154 ± 13

Table 2.1: Photometry for r1-25

	Date	Exposure	SCR	MCR	HCR	TCR	Total
ObsID	(MJD)	Time (s)	$10^{-3}s^{-1}$	$10^{-3}s^{-1}$	$10^{-3}s^{-1}$	$10^{-3}s^{-1}$	Counts
8529	54441.6	18923	···	···	···	8.9 ± 0.7	168 ± 13
8530	54451.5	19915	···	···	···	12.4 ± 0.8	247 ± 16

Columns 4, 5, and 6 are the count rates in the Soft (0.3-1.1 keV), Medium (1.1-2 keV), Hard (2-7 keV) bands, respectively. All rates are corrected by a vignetting factor.

Table 2.2: Spectral Fitting Results

	$N_H = 1.1 \times 10^{21}$ cm^{-2}			$N_H = 6.4 \times 10^{21}$ cm^{-2}		
Obs ID	kT (keV)	Normalization (10^{-6})	L_X (10^{37} ergs s^{-1})	kT (keV)	Normalization (10^{-6})	L_X (10^{37} ergs s^{-1})
1575	0.12 ± 0.01	$0.73^{+0.09}_{-0.08}$	0.40	0.065 ± 0.003	160^{+50}_{-40}	97
4720	0.28 ± 0.03	1.7 ± 0.3	1.0	0.19 ± 0.02	8^{+3}_{-2}	4.8
4721	0.23 ± 0.02	$2.0^{+0.4}_{-0.3}$	1.2	0.17 ± 0.01	10^{+4}_{-3}	6.0
4722	0.21 ± 0.02	$2.4^{+0.5}_{-0.4}$	1.4	0.11 ± 0.01	60^{+40}_{-20}	36

Spectral fits were carried out in the energy range 0.3-8.0 keV, using a simple absorbed blackbody model (wabs model was used for absorption). Luminosities are given for the same energy range and are corrected for assumed absorption. All uncertainties are 1σ in size.

Chapter 3

Three Gravitationally Lensed Supernovae behind CLASH Galaxy Clusters

ABSTRACT

We report observations of three gravitationally lensed supernovae (SNe) in the Cluster Lensing And Supernova survey with Hubble (CLASH) Multi-Cycle Treasury program. These objects, SN CLO12Car ($z = 1.28$), SN CLN12Did ($z = 0.85$), and SN CLA11Tib ($z = 1.14$), are located behind three different clusters, MACSJ1720.2+3536 ($z = 0.391$), RXJ1532.9+3021 ($z = 0.345$), and Abell 383 ($z = 0.187$), respectively. Each SN was detected in *Hubble Space Telescope (HST)* optical and infrared images. Based on photometric classification, we find that SNe CLO12Car and CLN12Did are likely to be Type Ia supernovae (SNe Ia), while the classification of SN CLA11Tib is inconclusive. Using multi-color light-curve fits to determine a standardized SN Ia luminosity distance, we infer that SN CLO12Car was $\sim 1.0 \pm 0.2$ mag brighter than field SNe Ia at a similar redshift and ascribe this to gravitational lens magnification. Similarly, SN CLN12Did is $\sim 0.2 \pm 0.2$ mag brighter than field SNe Ia. We derive independent estimates of the predicted magnification from CLASH strong+weak lensing maps of the clusters (in magnitude units, $2.5 \log_{10} \mu$): 0.83 ± 0.16 mag for SN CLO12Car, 0.28 ± 0.08 mag for SN CLN12Did, and 0.43 ± 0.11 mag for SN CLA11Tib. The two SNe Ia provide a new test of the cluster lens model predictions: we find that the magnifications based on the SN Ia brightness and those predicted by the lens maps are consistent. Our results herald the promise of future observations of

samples of cluster-lensed SNe Ia (from the ground or space) to help illuminate the dark-matter distribution in clusters of galaxies, through the direct determination of absolute magnifications.

3.1 Introduction

Supernovae have proven to be important tools for studying the Universe. Type Ia supernovae (SNe Ia) have been instrumental in the discovery that the expansion of the Universe is accelerating, and probing the dark energy driving the acceleration (e.g., Riess et al. 1998; Perlmutter et al. 1999; Wood-Vasey et al. 2007b; Kessler et al. 2009a; Hicken et al. 2009; Sullivan et al. 2011; Suzuki et al. 2012, and references therein). Core-collapse (CC) SNe trace the star-formation history of the Universe (e.g., Dahlen et al. 2004; Bazin et al. 2009; Botticella et al. 2012). Gravitational lensing of SNe can augment their cosmological utility, in both the strong and weak lensing regimes. The seminal paper of Refsdal (1964), which considered measuring galaxy masses and the Hubble parameter from lensed image time delays, in fact envisaged SNe as the background sources.[1] While no multiply imaged supernova (SN) has yet been discovered, several applications of lensed SNe are currently being explored.

Gravitational lensing allows massive galaxy clusters to be used as cosmic telescopes, increasing the apparent brightness of distant sources that would otherwise be too faint to detect (Sullivan et al. 2000; Kneib et al. 2004; Stanishev et al. 2009). Ground-based near-infrared (IR) surveys of galaxy clusters are being used to find lensed SNe, including a core-collapse SN with redshift $z = 1.7$ (Goobar et al. 2009; Amanullah et al. 2011, and references therein). Lensed SNe Ia are particularly useful, as their standardizable luminosities allow for a direct measurement of the absolute lensing magnification (Kolatt & Bartelmann 1998).

The Cluster Lensing And Supernova survey with Hubble (CLASH; Postman et al. 2012)

[1] Refsdal (1964) also presciently concluded with the idea that in addition to lensed SNe, "star-like objects with intense emission both in the radio range and optical range" that "have been recently discovered" may also be valuable lensed sources, "giving a possibility of testing the different [cosmological] models."

has observed 25 galaxy clusters in 16 *Hubble Space Telescope (HST)* broadband filters covering the near-ultraviolet (UV) to the near-IR with the Advanced Camera for Surveys (ACS) and the Wide Field Camera 3 (WFC3). The WFC3 infrared channel (WFC3/IR) is especially important for finding and studying high-redshift SNe, efficiently surveying large sky areas for SNe whose peak flux has redshifted from the optical to the infrared. The SN discoveries and follow-up observations from CLASH are discussed at length by Graur et al. (2014). Here we focus on SNe *behind* CLASH clusters (in the "prime" fields centered on the clusters); these have not been included in the Graur et al. (2014) "parallel" field sample.

All distant SNe are lensed (magnified, or more often, demagnified) to some extent by large-scale structure along the line of sight. This adds a statistical "nuisance" in cosmological inferences from SNe Ia that can be corrected either assuming an overall magnification distribution (e.g., Holz & Linder 2005; Martel & Premadi 2008) or with convergence estimates along each SN light of sight using simplified scaling relations applied to the nearby foreground galaxies observed (Kronborg et al. 2010; Jönsson et al. 2010; Smith et al. 2014, and references therein).

Individual SNe that are detectably magnified have been found only rarely in recent wide-field surveys. A gravitational lens has to be precisely aligned with the background source to produce large magnifications, and this is significantly rarer for SNe compared to background galaxies as sources. Their short-lived durations also make lensed SNe rarer than even lensed quasars (Oguri & Marshall 2010). Moreover, the survey footprints of the Supernova Legacy Survey (SNLS) and the SDSS-II Supernova Survey did not contain many massive galaxy clusters to act as lenses for background SNe (Graham et al. 2008; Dilday et al. 2010).

Kronborg et al. (2010) inferred that the most magnified SN Ia in SNLS had a magnification factor $\mu = 1.27$, corresponding to $\Delta m_\mu = 2.5 \log_{10} \mu = 0.26$ mag, calculated from the location and photometry of foreground galaxies along the line of sight. Jönsson et al. (2010) came to a similar conclusion, finding that the SNLS sample did not probe SNe Ia

with $\Delta m_\mu \gtrsim 0.25$ mag (however, see Karpenka et al. 2013, who find little to no lensing of the SNLS sample). Given the typical ~ 0.2 mag scatter in standardized SN Ia luminosities, a lensing signal at this level cannot be clearly ascertained for an individual object, although it can be detected statistically for a larger sample.

Lensing magnification by foreground galaxies is expected to play a larger role for more distant SNe. The Hubble Deep Field SN Ia 1997ff at $z \approx 1.7$ (Gilliland et al. 1999; Riess et al. 2001) is calculated to have a $\Delta m_\mu = 0.34 \pm 0.12$ mag from lens galaxies projected nearby (Benítez et al. 2002). The uncertainties in the SN light curve and cosmological model preclude a definitive detection of the expected magnification signal. Rather, in this case the estimated lensing magnification has been applied as a correction to the inferred SN luminosity distance to constrain cosmological parameters, though care should be taken that this is done self-consistently (Zitrin et al. 2013b).

Supernova properties were used by Quimby et al. (2013) to posit that the recent SN PS1-10afx at $z = 1.39$ was a SN Ia magnified by a factor of 30 ($\Delta m_\mu = 3.72 \pm 0.18$ mag)! However, there is no lens observed in this system, and the authors conclude that it must be dark. Chornock et al. (2013) offer an alternate model, that this SN is best explained as a superluminous core-collapse object, without significant magnification.

Ideally, we would like to confirm the detection of gravitational lensing magnification of a SN by independently checking the magnifications derived from the SN brightness and a lens-model prediction for consistency. In this paper, we discuss three gravitationally lensed SNe (SN CLO12Car, SN CLN12Did, and SN CLA11Tib) behind CLASH clusters. We present photometric observations of the SNe and spectroscopy of their host galaxies in §3.2. In §3.3 we discuss classification of the SNe and model light-curve fits. The gravitational magnifications from lens models are derived in §3.4, and we confront the models against the observations and discuss the results in 3.5. The following cosmological parameters are adopted throughout the paper (Sullivan et al. 2011): $H_0 = 71.6$ km s^{-1} Mpc^{-1}, $\Omega_M = 0.27$, $\Omega_\Lambda = 0.73$, and $\Omega_k = 0$.

3.2 Observations

3.2.1 SN CLO12Car

SN CLO12Car was discovered in the CLASH images of MACSJ1720.2+3536 (Ebeling et al. 2010). The SN was detected in June 2012 with both ACS and WFC3/IR. Figure 3.1 shows the location of the SN ($\alpha = 17^{\rm h}20^{\rm m}21.03^{\rm s}$, $\delta = +35°36'40\farcs9$, J2000), $0.35''$ from the center of its host galaxy. The host is relatively bright in the IR (F160W = 21.50 ± 0.01 AB mag), but is significantly fainter in the optical images (F606W = 24.21 ± 0.06 AB mag).

We present aperture photometry for SN CLO12Car in Table 3.1. These data include publicly available follow-up observations collected in July 2012 by *HST* program GO-12360 (PI S. Perlmutter). The flux from SN CLO12Car was measured in difference images, using templates constructed with CLASH observations from March and April 2012, more than 30 days before the first detection. For the ACS images, we used a fixed 4-pixel ($0\farcs20$) radius aperture, whereas for WFC3/IR, the photometry was measured in a 3-pixel radius ($0\farcs27$) aperture.

We used the DEep Imaging Multi-Object Spectrograph (DEIMOS; Faber et al. 2003) on the Keck-II 10 m telescope to obtain a $\sim$ 2 hr spectrum of the host galaxy of SN CLO12Car (2×1800 s, 1×1700 s, and 1×1500 s), with $\sim$ 4 Å resolution, covering the wavelength range 5000–9000 Å. The spectrum showed evidence of a weak emission line located between two night-sky lines near 8506 Å. For confirmation, we obtained a 2.5 hr (5×1800 s) Gemini North Multi-Object Spectrograph (GMOS; Hook et al. 2004) nod-and-shuffle spectrum of the host, spanning 7460–9570 Å with a resolution of $\sim$ 2.1 Å. The GMOS spectrum also shows evidence for the faint line (marginally resolved as a doublet), which we identify as [O II] $\lambda\lambda 3726, 3728$ emission at $z = 1.281 \pm 0.001$. A composite of the DEIMOS and GMOS spectra is shown in the top panel of Figure 3.2. The spectroscopic redshift for the CLO12Car host galaxy lies near the peak of its photometric redshift (photo-z) probability density function (PDF), but the photo-z PDF is broad, only limiting the

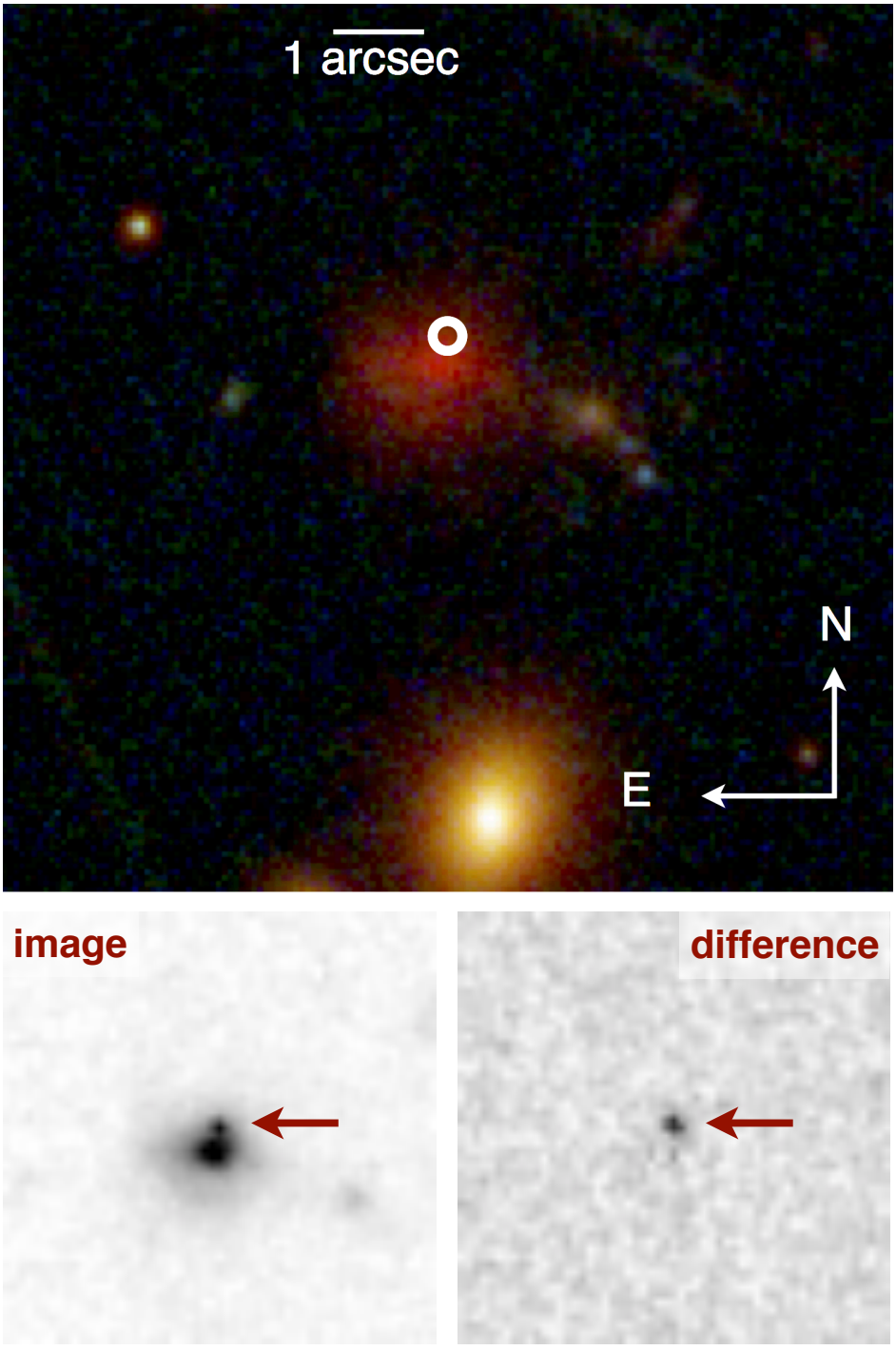

Figure 3.1 *Top:* CLASH *HST* composite false-color image of SN CLO12Car. In this image, the red channel is an average of the WFC3/IR F105W, F110W, F125W, F140W, and F160W data. The green channel combines ACS F606W, F625W, F775W, F814W, and F850LP observations, and the blue channel is from ACS F435W and F475W data. The location of the SN is marked with a white circle. *Bottom:* The left panel shows a 5″ square cutout of the WFC3/IR F160W image from 2012 June 17, with SN CLO12Car marked by the arrow; the right panel shows the difference image after template subtraction.

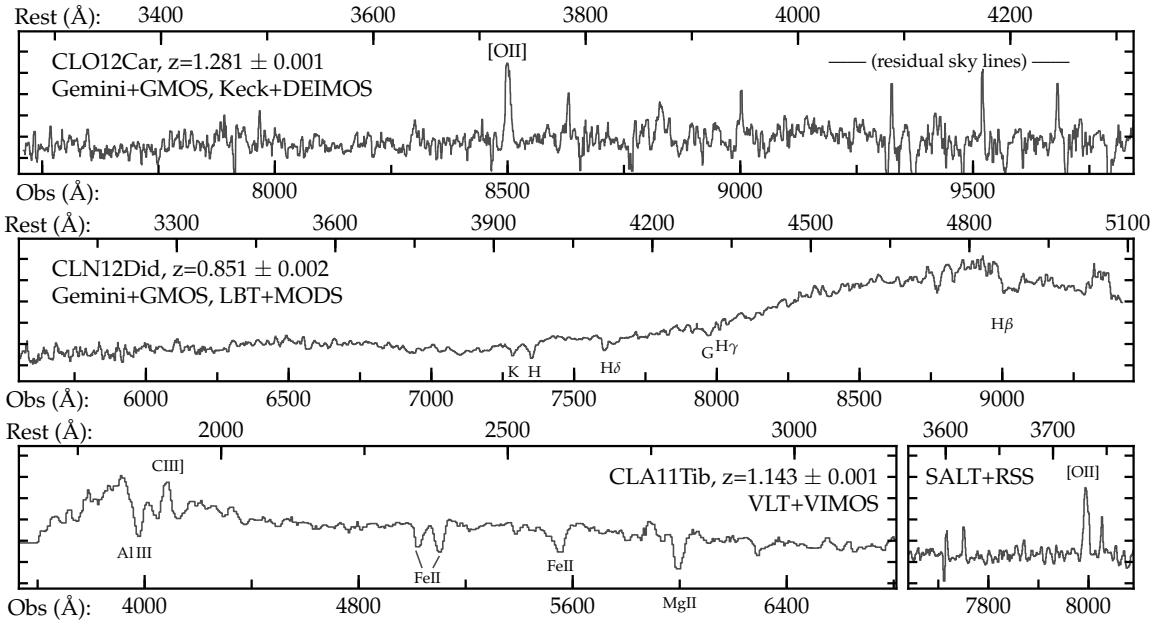

Figure 3.2 Spectra of the host galaxies of the three lensed SNe. Each panel shows observed wavelength along the bottom axis and rest wavelength on top. For display purposes, all spectra have been smoothed with a running 3-pixel median. *Top*: The host galaxy of SN CLO12Car, at $z = 1.281 \pm 0.001$. The plot shows the mean spectrum combining observations with Gemini+GMOS and Keck+DEIMOS. The single emission line at 8500 Å is identified as the [O II] $\lambda\lambda 3726, 3728$ doublet based on the photo-z and asymmetry of the line profile. *Middle*: The CLN12Did host galaxy, combining spectra from Gemini+GMOS and LBT+MODS. We derive $z = 0.851 \pm 0.002$ from cross-correlation with galaxy templates and identification of Ca and H absorption features, as indicated. *Bottom*: The left panel shows the spectrum of the SN CLA11Tib host galaxy, observed with VLT+VIMOS. We derive $z = 1.143 \pm 0.001$ from multiple absorption features and C III] $\lambda 1909$ emission. This confirms the [O II] emission-line redshift from the SALT+RSS spectrum shown on the right.

redshift to $0.9 \lesssim z \lesssim 1.9$. A full description of the CLASH photo-z estimation methods is given by Jouvel et al. (2014) and Molino et al. (in prep.). At $z = 1.281$, a separation of $0.35''$ from SN to host-galaxy center corresponds to a projected physical separation of ~ 3 kpc (modulo lensing magnification).

We also analyzed the follow-up *HST* WFC3/IR G102 and G141 grism (Dressel 2012) data for SN CLO12Car and its host galaxy (taken while the SN was still visible; program GO-12360, PI S. Perlmutter). The G102 spectrum has a dispersion of 25 Å pixel^{-1}, covering 8000–11,500 Å, while the G141 spectrum has a dispersion of 47 Å pixel^{-1}, covering 11,000–17,000 Å. The exposure time with each grating was about 1.3 hr, but this yielded only a

weak signal, and we were unable to extract a clear SN spectrum. In these slitless grism observations, spectral features are effectively convolved with the spatial profile of the source, making sharp emission lines broader and less pronounced. There is an emission line in the G141 grism spectrum at 14,963 Å, consistent with Hα λ6563 at $z \approx 1.28$, but this is only a marginal detection given the low resolution of the data.

3.2.2 SN CLN12Did

SN CLN12Did was discovered in early 2012 in CLASH ACS and WFC3/IR images of RXJ1532.9+3021 (Ebeling et al. 1998). Figure 3.3 shows the position of the SN (located at $\alpha = 15^{\rm h}32^{\rm m}59.25^{\rm s}$, $\delta = +30°21'42\farcs8$, J2000), and we present aperture photometry of the SN in Table 3.2. The SN was present in the first epoch of observations in each of the ACS and WFC3/IR filters, so we did not have a SN-free template for subtraction. Nonetheless, the SN is separated by $\sim 4''$ from its putative host galaxy, so we expect negligible host-galaxy contamination in the SN photometry.

Ground-based Sloan Digital Sky Survey (SDSS) DR7 images (Abazajian et al. 2009) of the CLN12Did host, along with the *HST* data, show the CLN12Did host to be an early-type, likely elliptical, galaxy. The CLASH data yield photometry for the host galaxy of F606W = 22.69 ± 0.03 AB mag and F160W = 19.434 ± 0.003 AB mag. We obtained a $\sim$ 5 hr spectrum (6×2700 s and 1×2500 s) of the host galaxy using the Multi-Object Double Spectrographs (MODS; Pogge et al. 2010) on the Large Binocular Telescope (LBT), covering 6300–9000 Å with 15–40 Å resolution. We also used Gemini North GMOS to obtain a 4.5 hr (9×1800 s) spectrum of the galaxy, covering 5220–9420 Å, with a resolution of $\sim$ 6 Å. A composite spectrum from the Gemini and LBT observations is shown in the middle panel of Figure 3.2. We derived respective redshifts of 0.851 ± 0.001 and 0.852 ± 0.002 from these data, via cross-correlation with absorption-line templates. This redshift is consistent with the photo-z derived for the galaxy ($z_{phot} = 0.92^{+0.05}_{-0.07}$). We adopt $z = 0.851 \pm 0.001$ for SN CLN12Did. At this redshift, the $4''$ separation from SN to host-galaxy center corresponds

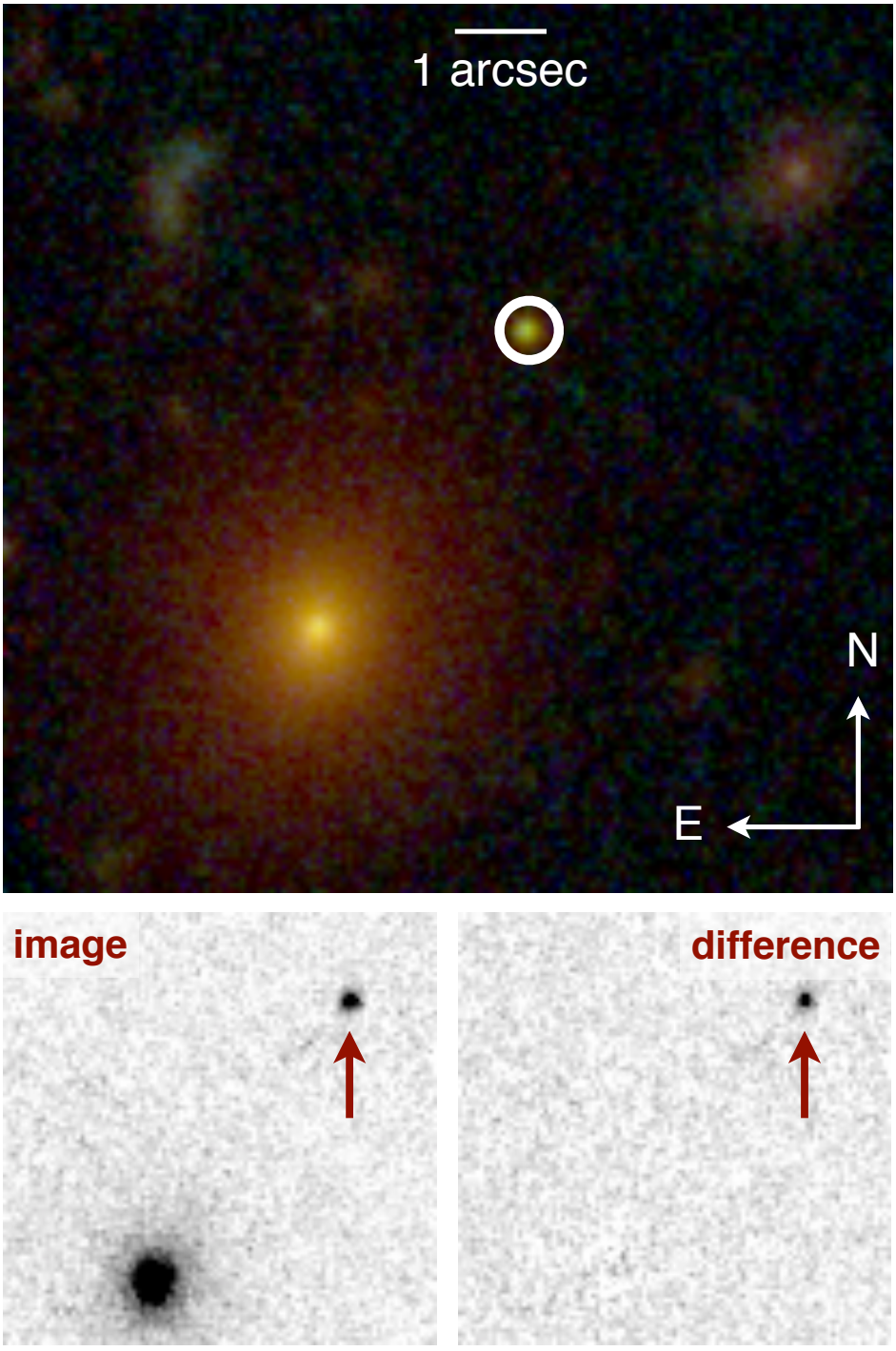

Figure 3.3 *Top: HST* composite false-color image of SN CLN12Did and surroundings. The red channel is an average of WFC3/IR F105W, F110W, F140W, and F160W data from the CLASH program, the green channel combines the ACS F606W, F625W, F775W, F814W, and F850LP observations, and the blue channel is from ACS F435W and F475W data. The SN position is marked with a white circle, in the outskirts of its early-type host galaxy to the southeast. *Bottom:* The left panel shows a 5″ square cutout of the ACS F850LP image from 2012 March 3, with SN CLN12Did marked by the arrow; the right panel shows the difference image after template subtraction.

to a projected physical separation of ~ 30 kpc (modulo lensing magnification).

3.2.3 SN CLA11Tib

SN CLA11Tib was discovered in CLASH ACS and WFC3/IR images of Abell 383 (Abell et al. 1989) in January 2011. Figure 3.4 shows the SN in a color image (located at $\alpha = 02^{\rm h}48^{\rm m}01.27^{\rm s}$, $\delta = -03°33'16\farcs9$, J2000). Aperture photometry for the ACS observations of SN CLA11Tib is presented in Table 3.3. The WFC3/IR observations of the SN were taken as part of the *HST* follow-up program GO-12360 (PI S. Perlmutter). The ACS photometry is from difference images with host-galaxy subtraction, but no template images are available for the WFC3/IR observations (F105W, F125W, and F160W), so the reported IR photometry is based on the direct images. As the SN is located in a spiral arm (see Figure 3.4), the host galaxy could contaminate aperture photometry for these observations. For this reason we report point-spread function (PSF) fitting photometry of the SN in the WFC3/IR observations from Dolphot (a modified version of HSTphot; Dolphin 2000). Photometry of the host galaxy gives F606W = 22.88 ± 0.01 AB mag and F160W = 21.51 ± 0.01 AB mag.

We obtained Southern African Large Telescope (SALT) + Robert Stobie Spectrograph (RSS; Nordsieck 2012; Crawford et al. 2010) spectroscopy of the host of SN CLA11Tib with a 1200 s exposure using the PG0900 grating (range 6300–9300 Å, resolution 6 Å), and detect a strong emission line (but close to a night-sky line) that we identify as [O II] at $z = 1.144 \pm 0.001$. We confirmed this identification with the VIsible MultiObject Spectrograph (VIMOS; Le Fèvre et al. 2003) on the Very Large Telescope (VLT) observations in a ~ 4 hr spectrum of the host galaxy (range 3900–6700 Å with 28 Å resolution). The spectrum shows Mg II and Fe II absorption, and C III] λ1909 emission, all at a consistent redshift of 1.143 ± 0.001, which we adopt for SN CLA11Tib. This redshift is consistent with the photo-z derived for the galaxy ($z_{phot} = 1.05 \pm 0.10$). At this redshift, SN CLA11Tib is projected ~ 25 kpc from the center of its host galaxy (uncorrected for lensing magnification).

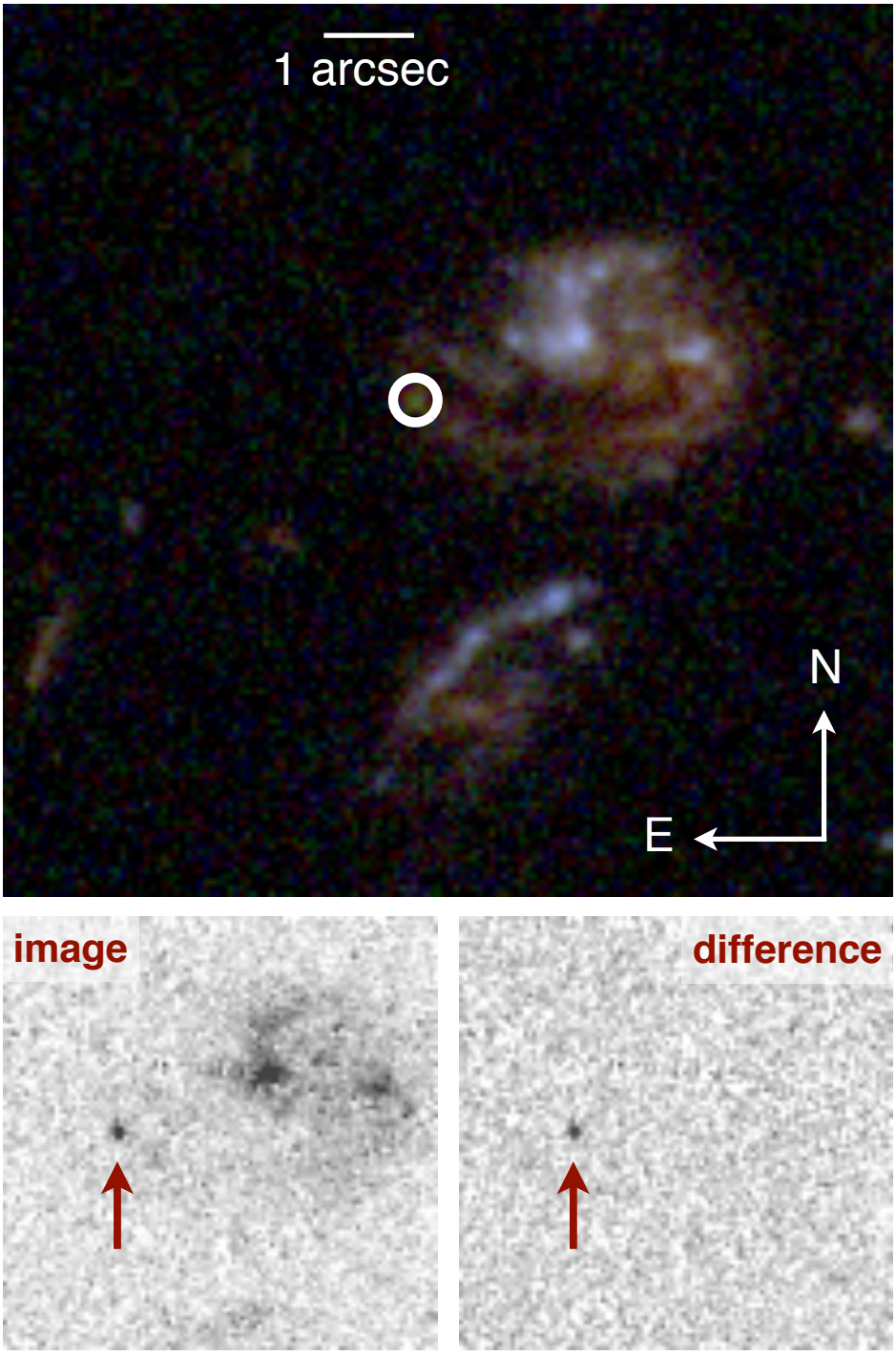

Figure 3.4 *Top: HST* composite false-color image of SN CLA11Tib from CLASH data. The red channel is an average of WFC3/IR F105W, F110W, F125W, F140W, and F160W data. The green channel combines ACS F606W, F625W, F775W, F814W, and F850LP observations, and the blue channel is from ACS F435W and F475W data. The location of the SN is marked with a white circle. *Bottom:* The left panel shows a 5″ square cutout of the ACS F850LP image taken on UT 2011 Jan. 4, with SN CLA11Tib indicated by the arrow; the right panel shows the difference image after template subtraction.

3.3 SN Classification and Light-Curve Fits

Classification of high-redshift ($z \gtrsim 1$) SNe is challenging (e.g., Rodney et al. 2012; Rubin et al. 2013; Jones et al. 2013). For example, a typical SN Ia has a peak luminosity in the rest-frame B band of $M_B \approx -19.4$ mag. At $z = 1.5$ this becomes a Y-band apparent magnitude of ~ 25.8. Key spectral absorption features at rest-frame optical wavelengths (such as the Si II feature observed in SN Ia at ~ 6150 Å) are redshifted into the IR, making them inaccessible to most ground-based spectrographs. With these constraints, definitive spectroscopic classification of high-z SNe requires prohibitively large investments of *HST* time (Jones et al. 2013).

For this reason, we rely on photometric classifications for these three lensed SNe. We utilize a Bayesian photometric SN classifier called STARDUST: Supernova Taxonomy And Redshift Determination Using SNANA Templates. An early version of this classifier was first introduced by Jones et al. (2013), and the complete version used for this work is presented in more detail by Graur et al. (2014) and Rodney et al. (in prep.). In brief, observations are compared against simulated SNe Ia and CC SNe, generated using version 10.27k of the SuperNova ANAlysis software package[2] (SNANA; Kessler et al. 2009b). For SNe Ia the STARDUST classifier uses the SALT2 light-curve model (Guy et al. 2010) extended to cover the rest-frame near-UV and IR wavelengths (see below), whereas for CC SNe, the classifier draws on the SNANA library of 16 SN Ib/c and 26 SN II templates, to be described in further detail by Sako et al. (2014). An important capability of STARDUST that we employ for this work is to allow an achromatic flux scaling factor for every model realization. This means that our STARDUST classifications rely only on the observed SN colors and light curve shape, and do not depend on the intrinsic SN luminosities or our choice of cosmological model. This is especially important for fitting lensed SNe, as it allows us to classify the SNe independent of the lensing magnification.

[2] http://sdssdp62.fnal.gov/sdsssn/SNANA-PUBLIC/

For additional verification of our photometric SN classifications, we turned to the Photometric SuperNova IDentification software (PSNID; Sako et al. 2008, 2011) to classify the three SNe. PSNID is similar to the STARDUST classifier, as both use SALT2 to simulate SNe Ia and rely on the same 16 SN Ib/c and 26 SN II templates to simulate CC SNe. However, PSNID has the advantage that it has been thoroughly tested, obtaining the highest figure of merit in the SN Photometric Classification Challenge (Kessler et al. 2010), and it is already publicly available as a component of SNANA. A downside of PSNID for this work is that it uses absolute magnitude priors in its classifications, which is not ideal for analyzing lensed SNe.

For SNe Ia, we also employed a modified version of the Guy et al. (2010) SALT2 model to fit light curves and derive standardized luminosity distances. The version of SALT2 presented by Guy et al. (2010) has been robustly tested, and was used in SNLS cosmology papers (Sullivan et al. 2011; Conley et al. 2011). To accommodate the wide wavelength range of our data, we extended the SALT2 model to cover rest-frame near-UV and IR wavelengths (by default, the SALT2 fitter can only fit rest wavelengths of 2800–7000 Å). For all three SNe, this extended SALT2 model produces similar results (within 1σ) to those of the original Guy et al. (2010) model. In deriving distances, we converted our SALT2 parameters representing light-curve shape and color excess ($x1$ and c) to their respective SiFTO (Conley et al. 2008) parameters (s and C), using the conversion equations from Guy et al. (2010). This was done in order to adopt the constants M, α, and β, from Sullivan et al. (2011) and also used by Jones et al. (2013). Specifically, the distance modulus was calculated using the following equation:[3]

$$\mathrm{dm}_{\mathrm{SALT2}} = m_B^* - M + \alpha(s-1) - \beta C, \tag{3.1}$$

with $M = -19.12 \pm 0.03$, $\alpha = 1.367 \pm 0.086$, and $\beta = 3.179 \pm 0.101$. To match the (for

[3]We use the notation "dm" for distance modulus, rather than the conventional μ, to avoid confusion with the lensing magnification μ. As usual, it is defined as $\mathrm{dm} = 5 \log_{10} d_L + 25$, where d_L is the luminosity distance in Mpc.

our purposes, arbitrary) normalization of the SALT2 fitter used by Guy et al. (2010) to our results from SNANA, we applied an offset of 0.27 mag to the value of m_B^* reported by SNANA.

We also used the Jha et al. (2007) version of MLCS2k2 included in SNANA to fit the SNe Ia. To check for consistency, we compared the best-fit light curve shape parameter Δ from MLCS2k2 to $x1$ from SALT2 using the relationship in Appendix G given by Kessler et al. (2009a). To compare the SALT2 color parameter c with MLCS2k2 A_V, we employ a linear relationship derived from Figure 42 of Kessler et al. (2009a), specifically

$$c = (0.464 \pm 0.021)A_V - (0.121 \pm 0.014). \tag{3.2}$$

Finally, to ensure a consistent zeropoint between the SALT2 and MLCS2k2 distance moduli, we applied both methods to a sample of SDSS Supernova Survey SNe Ia from Holtzman et al. (2008); Kessler et al. (2009a). We added a zeropoint correction of 0.20 mag to the distance moduli reported by SNANA in the MLCS2k2 fit ($\mathrm{dm_{MLCS2k2}}$), to put them on the same scale as the SALT2 distances ($\mathrm{dm_{SALT2}}$).

Although we report magnitudes in Tables 3.1, 3.2, and 3.3, both the classification and SN Ia light curve fitting were done in flux space. The upper limits for each SN were included in the fits with the measured flux and 1σ uncertainties.

3.3.1 SN CLO12Car

SN CLO12Car was located in a red disky galaxy, in which both SNe Ia and CC SNe could be expected. The STARDUST classifier prefers a SN Ia fit with probability (P_{Ia}) of 0.91. The probabilities for SN Ib/c ($P_{\mathrm{Ib/c}}$) and SN II (P_{II}) models are 10^{-8} and 0.09, respectively. The best-fit SN Ia, SN Ib/c, and SN II models had χ^2/ν ($\nu = 11$) of 1.12, 4.56, and 1.76, respectively. PSNID also favors a SN Ia fit at a high confidence, with $P_{\mathrm{Ia}} = 0.99$ and a

best-fit $\chi^2/\nu = 1.06$ ($\nu = 11$)[4]. We thus conclude that SN CLO12Car was a SN Ia.

Both MLCS2k2 and SALT2 produce good light-curve fits for SN CLO12Car. We show the SALT2 light-curve fit along with the 1σ model errors in Figure 3.5. The SALT2 fit had a $\chi^2/\nu = 13.3/11 = 1.21$, and the fit parameters ($x1 = 1.375 \pm 0.829$ and $c = 0.254 \pm 0.049$) are in the range of normal SNe Ia (Guy et al. 2010). From these parameters, we derive a distance modulus of $\mathrm{dm_{SALT2}} = 43.83 \pm 0.24$ mag for the SN.

The MLCS2k2 light-curve fit had a slightly worse, but still acceptable, goodness-of-fit ($\chi^2/\nu = 18.1/11 = 1.64$). The model parameters were $\Delta = 0.007 \pm 0.314$ and $A_V = 0.635 \pm 0.190$ mag. The light curve shape parameters from the two fitters agree at $< 1\sigma$; specifically, the SALT2 $x1$ value corresponds to $\Delta = -0.380 \pm 0.160$. The best-fit MLCS2k2 A_V corresponds to $c = 0.174 \pm 0.090$, which is also $< 1\sigma$ from the best-fit SALT2 color. Moreover, we find that $\mathrm{dm_{MLCS2k2}} = 43.71 \pm 0.16$ mag (after applying the zeropoint correction), again consistent with the inferred $\mathrm{dm_{SALT2}}$ at $< 1\sigma$.

For comparison, at $z = 1.281$, the distance modulus expected from ΛCDM with our adopted cosmological parameters is $\mathrm{dm_{\Lambda CDM}} = 44.76$ mag, significantly higher than what is measured from the SN light curve. We discuss the implications of this finding in §3.4.

3.3.2 SN CLN12Did

SN CLN12Did was located in an elliptical galaxy, already indicating it was most likely a SN Ia (Cappellaro et al. 1999; Mannucci 2005; Foley & Mandel 2013). The STARDUST classifier prefers a SN Ia fit at high confidence ($> 5\sigma$). PSNID also favors a SN Ia fit with high significance ($P_{\mathrm{Ia}} > 0.9999$), with best-fit $\chi^2/\nu = 0.5$ ($\nu = 20$). These consistent results yield the strong conclusion that SN CLN12Did was a SN Ia.

We show the SALT2 SN Ia light-curve fit for SN CLN12Did in Figure 3.6. Similar to Figure 3.5, we display the light-curve points and the model curves with 1σ errors. Upper

[4]PSNID uses a luminosity prior, as discussed above. Correcting the light curve for lensing, assuming reasonable values of magnification between 1 mag of demagnification and 3 mag of magnification, changes the P_{Ia} value slightly (ranging from 0.87 to 0.99).

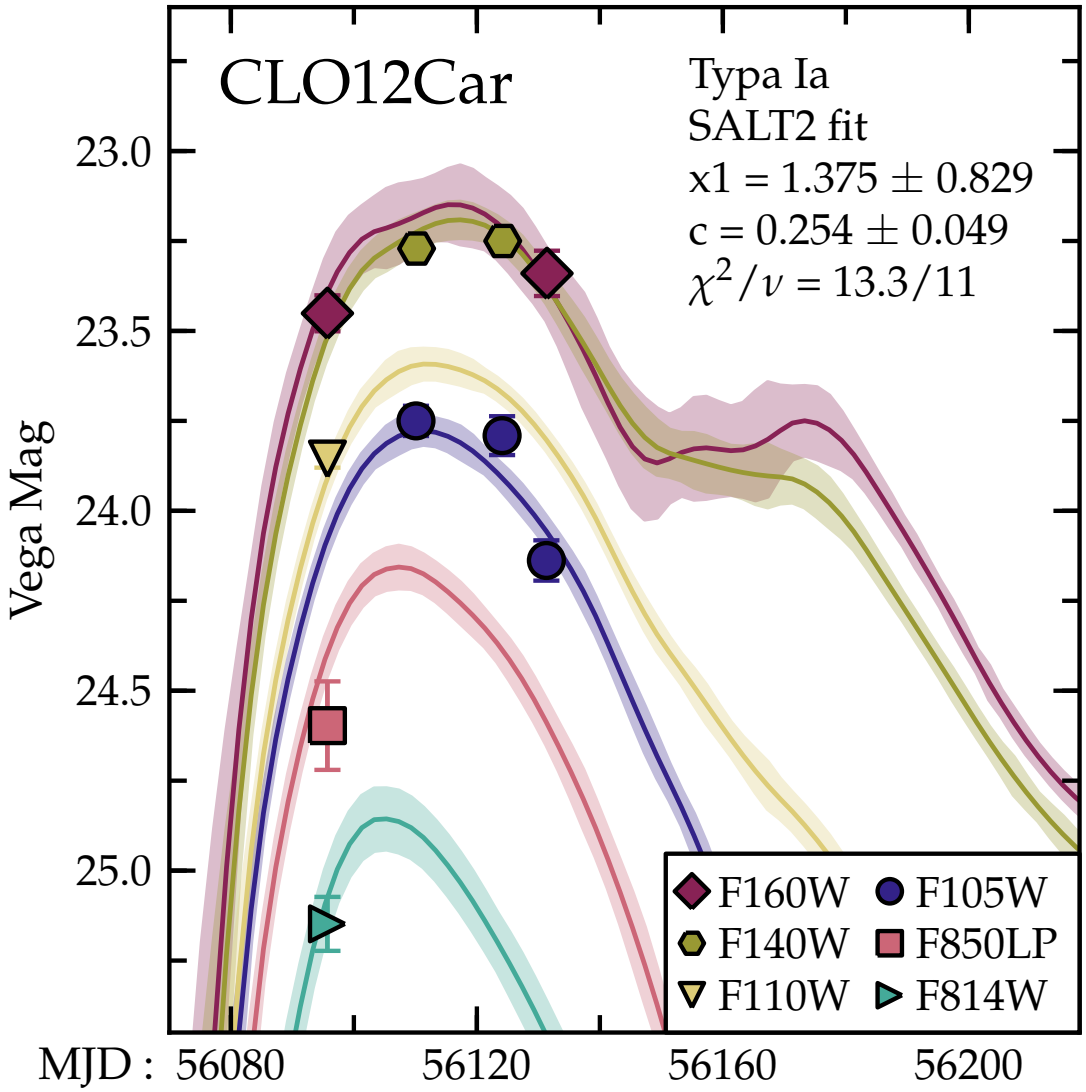

Figure 3.5 SALT2 light-curve fit of SN CLO12Car. The light-curve parameters $x1$ and c are typical of normal SNe Ia, and the data are well matched by the model, with $\chi^2/\nu = 13.3/11$.

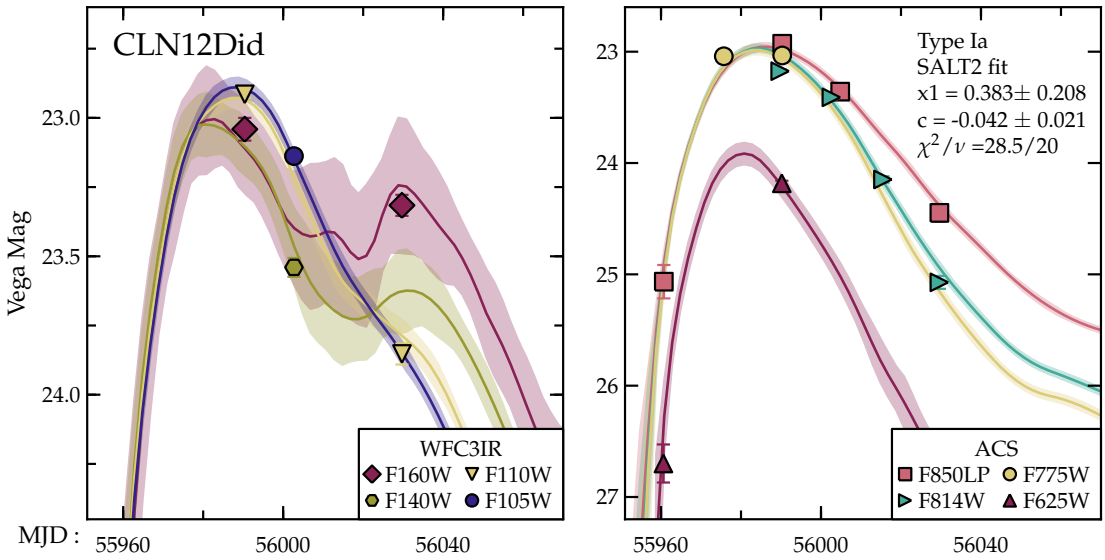

Figure 3.6 SALT2 light-curve fit of SN CLN12Did. Upper limits on F435W and F475W nondetections are excluded from the plot for clarity, but all of the observations listed in Table 3.2 are used in the light-curve fit. This model is a reasonably good match to the data, yielding $\chi^2/\nu = 1.4$. The best-fit light-curve parameters are typical for a normal SN Ia.

limits on F435W and F475W nondetections are excluded from the plot for clarity, but all of the observations listed in Table 3.2 are used in the light-curve fit. The SALT2 parameters fall within the normal SN Ia range, with $x1 = 0.383 \pm 0.208$, $c = -0.042 \pm 0.021$, and $\chi^2/\nu = 28.5/20 = 1.42$. From the light-curve parameters, we derive $\mathrm{dm}_{\mathrm{SALT2}} = 43.33 \pm 0.15$ mag.

MLCS2k2 produces a slightly better light-curve fit, with $\chi^2/\nu = 23.6/20 = 1.18$. The best-fit parameters are $A_V = 0.042 \pm 0.059$ mag and $\Delta = 0.055 \pm 0.098$. Using the conversion equations, the MLCS2k2 fit A_V corresponds to SALT2 $c = -0.102 \pm 0.031$, and the SALT2 $x1$ predicts MLCS2k2 $\Delta = -0.212 \pm 0.040$. This is good agreement in the color parameter, but a slight ($\sim 2.5\sigma$) discrepancy in light-curve shape. The inferred distance is $\mathrm{dm}_{\mathrm{MLCS2k2}} = 43.28 \pm 0.09$ mag, consistent with the SALT2 result. For comparison, at $z = 0.851$, the cosmological parameters yield $\mathrm{dm}_{\Lambda\mathrm{CDM}} = 43.65$ mag.

3.3.3 SN CLA11Tib

SN CLN12Tib is located in a spiral arm of its blue, late-type host galaxy, an environment in which all SN types can be found (Cappellaro et al. 1999; Mannucci 2005; Li et al. 2011b; Foley & Mandel 2013). The STARDUST classifier prefers a CC fit for this SN, returning probabilities $P_{\rm II} = 0.41$ and $P_{\rm Ib/c} = 0.52$, compared to the SN Ia fit probability $P_{\rm Ia} = 0.07$.

We show the light-curve fit for SN CLA11Tib in Figure 3.7, with each row giving the maximum-likelihood fit for a single SN subclass. The χ^2/ν ($\nu = 14$) values for the best-fit SN Ia, SN Ib/c, and SN II models are 3.81, 3.42, and 3.55, respectively. None of the three SN types are a good fit to the light-curve; moreover, none of the templates provide a good fit to all the WFC3/IR data. There are only 42 CC SNe templates, and we do not expect them to represent the full range of SNe II and SNe Ibc. The SN II template that provides the best match to the observations is SDSS-018793 (SN 2007og), a SN IIP at $z = 0.20$ (Sako et al. 2014). For the SNe Ib/c, the best match comes from SN SDSS-017548 (SN 2007ms), a SN Ic at $z = 0.0393$ (Östman et al. 2011). The sole *HST* WFC3/IR F125W observation of SN CLA11Tib is close to the peak for both the SN IIP and SN Ic models; at $z = 1.143$, the F125W filter corresponds to approximately the rest V band. To further highlight the difficulty in photometrically classifying SN CLA11Tib, in Figure 3.8 we show color-color diagrams from the ACS and WFC3/IR photometry taken during 2011 Jan. 22–24, where the SN straddles the typical colors of SNe Ia, Ib/c, and II, though favoring CC SN models. The full STARDUST classification uses these types of constraints with all available epochs.

Our PSNID results disagree with those from the STARDUST classifier. PSNID favors a SN Ia fit for SN CLA11Tib at greater than 4σ. However, the best-fit PSNID SN Ia model does not match the light curve well ($\chi^2/\nu = 2.83$, with $\nu = 14$). To check these results, we fit SN CLA11Tib with SALT2 and MLCS2k2 directly using SNANA. The best SALT2 fit has normal light-curve parameters, with $x1 = 0.114 \pm 0.486$ and $c = 0.048 \pm 0.037$, yielding $\mathrm{dm}_{\rm SALT2} = 44.07 \pm 0.19$ mag (for comparison, $\mathrm{dm}_{\Lambda\rm CDM} = 44.45$ mag). However, as with PSNID, the SNANA SALT2 fit requires an unacceptably large $\chi^2/\nu = 57.8/14 = 4.13$.

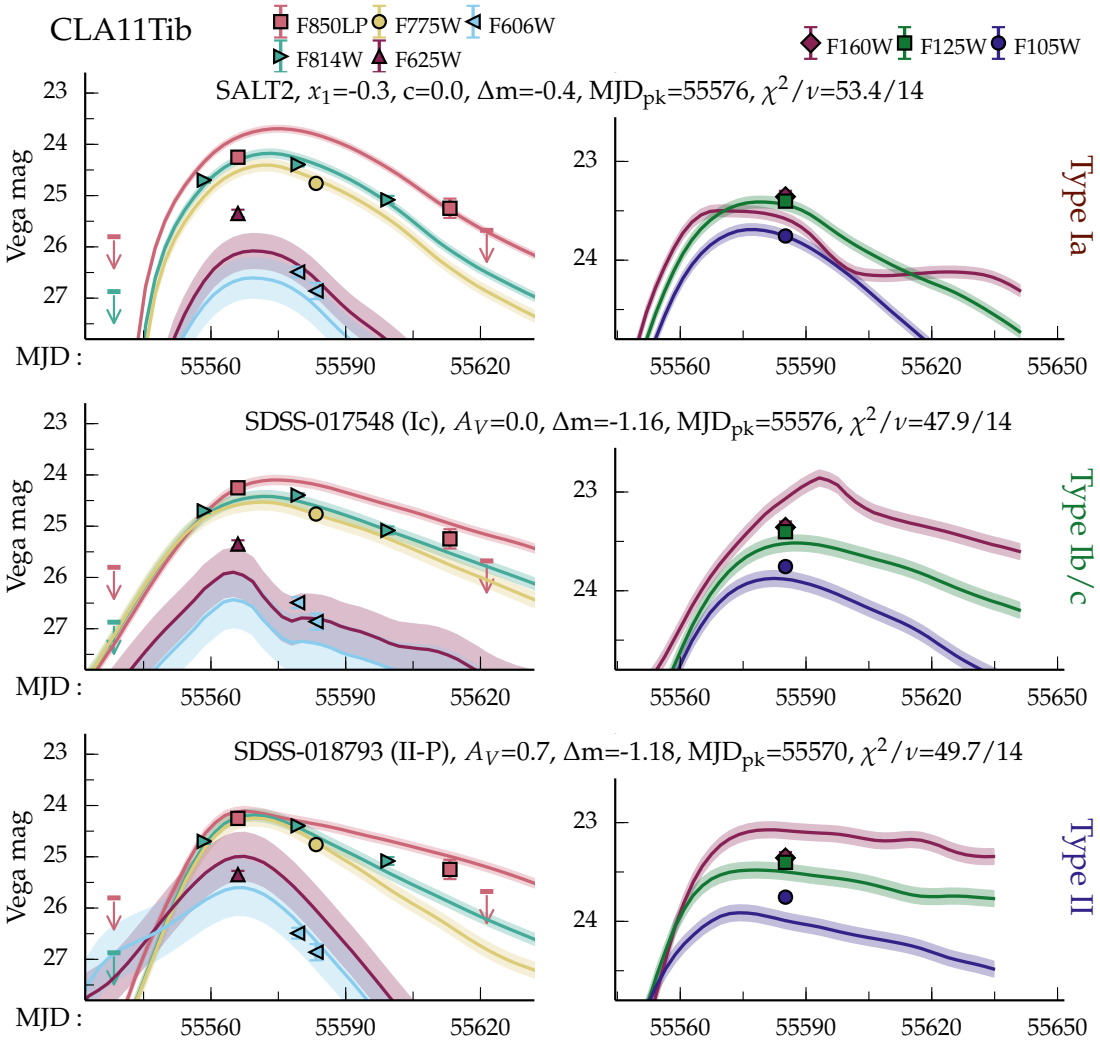

Figure 3.7 STARDUST light-curve fits to CLA11Tib for the three primary SN subclasses. The top row shows the maximum likelihood fit from a SN Ia (SALT2) model, the middle row displays the best-fit SN Ib/c model, and the bottom row shows the preferred SN II model. Optical data from ACS appear in the left column, while WFC3/IR observations are on the right. The CC SN models are labeled by the best-fit template SN, and all three models show the best-fit parameters. The downward pointing arrows indicate 3σ upper limits on the SN flux. The Δm term designates the offset (mag) needed to make the template match the data, discussed further in §3.4.3.

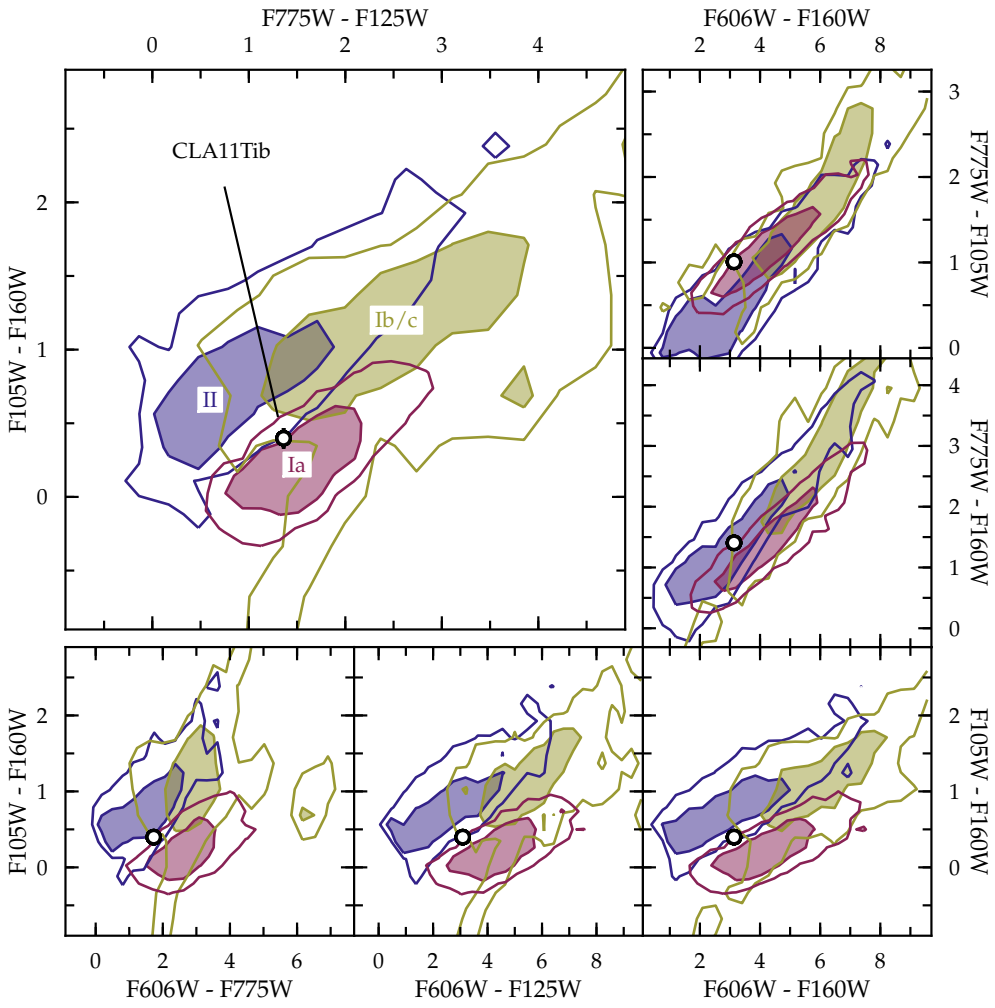

Figure 3.8 Color-color diagrams for SN CLA11Tib photometry from MJD 55583–55585, illustrating the difficulty in photometric classification of this object. We utilize color-based classification so as to be unaffected by achromatic gravitational lensing. The data favor a core-collapse origin for this SN (either SN Ib/c or SN II). The contours shown are derived from SNANA Monte Carlo simulations with 5000 simulated SNe for each of the 3 subclasses (so they do not reflect the relative frequency across classes). Shaded regions enclose 68% of each population and solid lines enclose 95%.

These results do not change substantially if we use the restricted-wavelength version of SALT2; the fit remains poor. The MLCS2k2 results were much better ($\chi^2/\nu = 29.8/14 = 2.13$), with best-fit light-curve parameters of $A_V = 0.389 \pm 0.193$ mag, $\Delta = -0.011 \pm 0.244$, and $\mathrm{dm}_{\mathrm{MLCS2k2}} = 43.97 \pm 0.14$ mag. Using the conversion equations, the MLCS2k2 fit A_V corresponds to SALT2 $c = 0.059 \pm 0.091$, and the SALT2 $x1$ predicts MLCS2k2 $\Delta = -0.201 \pm 0.093$. Interestingly, the MLCS2k2 and SALT2 parameters are similar, but the SALT2 fit is significantly worse.

To summarize, our classification analysis of SN CLA11Tib is inconclusive. The light curve was best fit by CC SN templates with STARDUST, while PSNID preferred a SN Ia fit. Similar to SN CLO12Car, we corrected the light curve for a varying amount of lensing (from 1 mag of demagnification to 3 mag of magnification) and fit with PSNID to see if the luminosity prior was driving the classification. The value of P_{Ia} varied greatly, with the probability dropping to 0 with magnifications > 1.5 mag. Because of these conflicting results, we further explore both CC SN and SN Ia models in our lensing analysis of SN CLA11Tib (§3.4.3).

3.4 Gravitational Lensing Magnification

In this section, we derive the magnification of each SN in two independent ways. First, we use the SNe themselves, from the observed SN brightness and light-curve fits described in §3.3. Second, we independently determine the expected magnification from cluster mass maps derived by the CLASH team from strong+weak lensing features.

One approach to inferring the SN magnification is simply measuring the offset between the inferred distance modulus and that predicted by the cosmological model ($\mathrm{dm}_{\Lambda\mathrm{CDM}}$). In that case, however, statistical and systematic uncertainties in the cosmological parameters (which are themselves derived in part from SNe Ia over a wide redshift range) need to be included in the analysis. A more direct approach is to compare the CLASH SNe directly to a "field" sample at similar redshifts. For a sufficiently small redshift range, the relation

between distance modulus and redshift can be taken to be linear. The field sample of SNe Ia define the zeropoint and slope of that relationship, and we derive the inferred magnification of our SN Ia relative to that locus, with all of these SNe analyzed in an identical way. This differential approach is insensitive to zeropoint offsets between the fitters and cosmological parameters, and only makes the assumption that all SNe Ia at nearly the same redshift are consistently standardizable (so it is less susceptible to evolution or other SN Ia systematics that vary with redshift).

For the predicted magnification from the CLASH cluster mass maps, we analyzed both the strong and weak lensing features in the clusters. The identification of multiple images in the cluster fields was done using the 16-band *HST* imaging obtained in the context of the CLASH campaign. The Zitrin et al. (2009) method revealed nine multiple image systems in the case of Abell 383 and seven systems in MACS J1720. Unfortunately, no multiple-image systems were found in the field of RX J1532, the cluster with the lowest total mass in this study. Where available, spectroscopic redshifts from the literature or the CLASH-VLT program (Balestra et al. 2013) determined the distance to the strong lensing features. The reliable 16-band photometric redshifts (Jouvel et al. 2014) from the CLASH pipeline delivered the redshifts of systems without spectroscopic confirmation. In the case of weak lensing, we used 5-band CLASH Subaru imaging to derive weak lensing shear catalogues. The underlying pipeline for image reduction, shape measurement, and background selection is thoroughly outlined by Umetsu et al. (2012) and Medezinski et al. (2013).

To combine the constraints from the weak and strong lensing regime into a consistent lens model, we used SaWLens (Merten et al. 2009; Meneghetti et al. 2010; Merten et al. 2011; Umetsu et al. 2012; Medezinski et al. 2013). This nonparametric method also reconstructs the mass distribution in the regime far away from the strong lensing features, or where no strong lensing features are available, and both cases apply in our study. By nonparametric, we mean that no *a priori* assumptions on the mass distribution of the lens were made. The method reconstructs the lensing potential, the rescaled and line-of-sight integrated

counterpart of the Newtonian potential, on an adaptively refined mesh using both weak and strong lensing inputs. In the case of RX J1532, where no strong lensing features were found, we use only the shear catalogues to constrain the lens mass distribution. From the lensing potential maps we directly derive the magnification (e.g., Bartelmann 2010) at the redshift of interest and read off its value at the position of each SN, as described individually below. In order to assign error bars to these values, we run 1500 realizations of each lens model by bootstrapping the weak lensing input catalogues and randomly sampling through the allowed redshift error range of each strong lensing feature (Merten et al. 2011).

The independent magnification estimates, from both methods above, are summarized in Table 3.4. We consider each object individually below. Because we could not conclusively classify SN CLA11Tib, we consider both the SN Ia and CC SN models for it (§3.4.3).

3.4.1 SN CLO12Car

We showed in §3.2.1 and §3.3.1 that SN CLO12Car was a SN Ia at $z = 1.281$. In Figure 3.9, we display two Hubble diagrams for the SN. The top plot contains SN Ia distances fit with SALT2 and the bottom plot with MLCS2k2. Both plots also show a comparison sample of 18 field SNe Ia from Riess et al. (2007) and Suzuki et al. (2012) in the range $1.14 \leq z \leq 1.41$, fit in exactly the same manner as SN CLO12Car. Consistently with either light-curve fitter, we find that SN CLO12Car was significantly brighter than the typical SNe Ia at a similar redshift. The solid black line in both panels represents the best linear fit to the field SN Ia sample, with the fit slope and intercept as shown.[5] From this analysis, we can estimate the lensing magnification as determined by the SN itself. The linear fits to the field sample predict $\mathrm{dm}_{\mathrm{SALT2}}(z = 1.281) = 44.74 \pm 0.07$ mag and $\mathrm{dm}_{\mathrm{MLCS2k2}}(z = 1.281) = 44.77 \pm 0.05$ mag. With these values, we derive that SN CLO12Car was magnified by $\Delta m_{\mu,\mathrm{SALT2}} = 0.91 \pm 0.25$ mag (corresponding to a magnification $\mu_{\mathrm{SALT2}} = 2.31 \pm 0.54$)

[5]Three of the Suzuki et al. (2012) SNe Ia plotted in Figure 3.9 were also behind galaxy clusters and potentially lensed. However, the object with the highest estimated magnification still only has $\mu = 1.07$, corresponding to $\Delta m_{\mu} = 0.07$ mag, well within the SN Ia scatter. Removing these three SNe Ia from the comparison sample has a negligible effect on our results.

in the SALT2 model, or $\Delta m_{\mu,\mathrm{MLCS2k2}} = 1.06 \pm 0.17$ mag ($\mu_{\mathrm{MLCS2k2}} = 2.65 \pm 0.42$) with MLCS2k2.

The cluster lensing magnification map (derived as described above) around MACS J1720 for a source at the SN redshift ($z = 1.281$) is shown in Figure 3.10. From the map, we derive a lensing magnification for SN CLO12Car of $\mu = 2.15 \pm 0.33$, which corresponds to $\Delta m_{\mu} = 0.83 \pm 0.16$ mag. The magnification from the light-curve fits and the lensing maps agree to well within 1σ. Moreover, SN CLO12Car is inconsistent with being unlensed; its SN Ia fit requires $\Delta m_{\mu} > 0$ at $\sim 4\sigma$.

3.4.2 SN CLN12Did

We showed in §3.2.2 and §3.3.2 that SN CLN12Did was a SN Ia at $z = 0.851$. In Figure 3.11, we display two Hubble diagrams for the SN, mirroring the analysis for SN CLO12Car (see §3.4.1 and Figure 3.9). The comparison field sample contains 63 SNe Ia from the SNLS sample (Guy et al. 2010) in the range $0.75 \leq z \leq 0.95$. Unlike the case for SN CLO12Car, we see that SN CLN12Did falls well within the normal scatter for typical SNe Ia in the redshift range. Both light-curve fitters do find SN CLN12Did to be brighter than expected compared to the field sample, but not significantly so ($\sim 1\sigma$). Our inferred magnification estimates for SN CLN12Did are $\Delta m_{\mu,\mathrm{SALT2}} = 0.24 \pm 0.15$ mag ($\mu_{\mathrm{SALT2}} = 1.25 \pm 0.18$) and $\Delta m_{\mu,\mathrm{MLCS2k2}} = 0.15 \pm 0.09$ mag ($\mu_{\mathrm{MLCS2k2}} = 1.15 \pm 0.10$).

The cluster lensing magnification map around RX J1532 for a source at $z = 0.851$ is shown in Figure 3.12. It predicts a lensing magnification for SN CLN12Did of $\Delta m_{\mu} = 0.28 \pm 0.08$ mag ($\mu = 1.29 \pm 0.09$). Just like in the case of SN CLO12Car, the lensing map prediction is consistent with the magnification inferred from the SN light curve, though for SN CLN12Did the magnification is only detected at low significance.

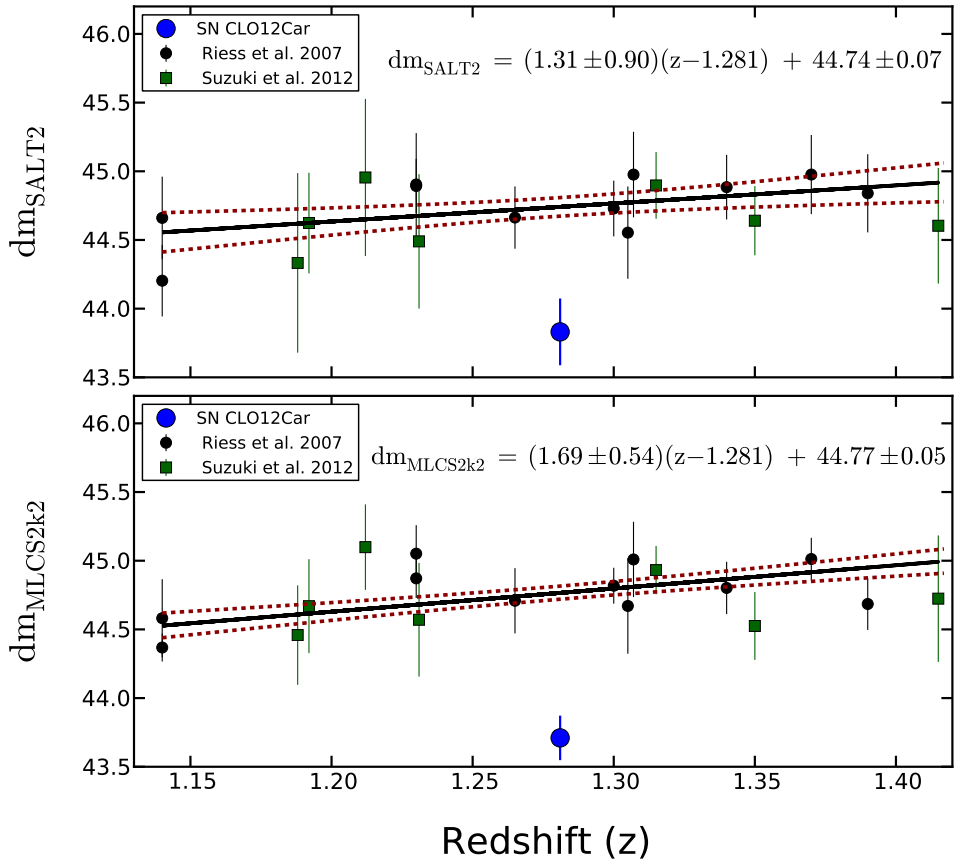

Figure 3.9 Hubble diagrams for SN CLO12Car. The top panel shows SN Ia distances fit with SALT2 and the bottom panel has MLCS2k2 fits. The plots contain 18 field SNe Ia from Riess et al. (2007, in black) and Suzuki et al. (2012, in green) as a comparison sample. Both light-curve fitters show that SN CLO12Car (the large blue point) was significantly brighter than typical SNe Ia at similar redshifts. The solid black lines with the displayed equations give the best-fit linear model to the comparison sample (empirically approximating a cosmological fit over this small redshift range without any dependence on cosmological parameters), with the red dashed lines representing the 1σ uncertainties. From these data, we predict that a typical unlensed SN Ia at $z = 1.281$ would have $\mathrm{dm_{SALT2}} = 44.74 \pm 0.07$ mag and $\mathrm{dm_{MLCS2k2}} = 44.77 \pm 0.05$ mag. Compared to the inferred distance modulus of SN CLO12Car, we find that it was magnified by $\Delta m_{\mu,\mathrm{SALT2}} = 0.91 \pm 0.25$ mag or $\Delta m_{\mu,\mathrm{MLCS2k2}} = 1.06 \pm 0.17$ mag. Both light-curve fitters give a consistent and significant magnification (greater than unity).

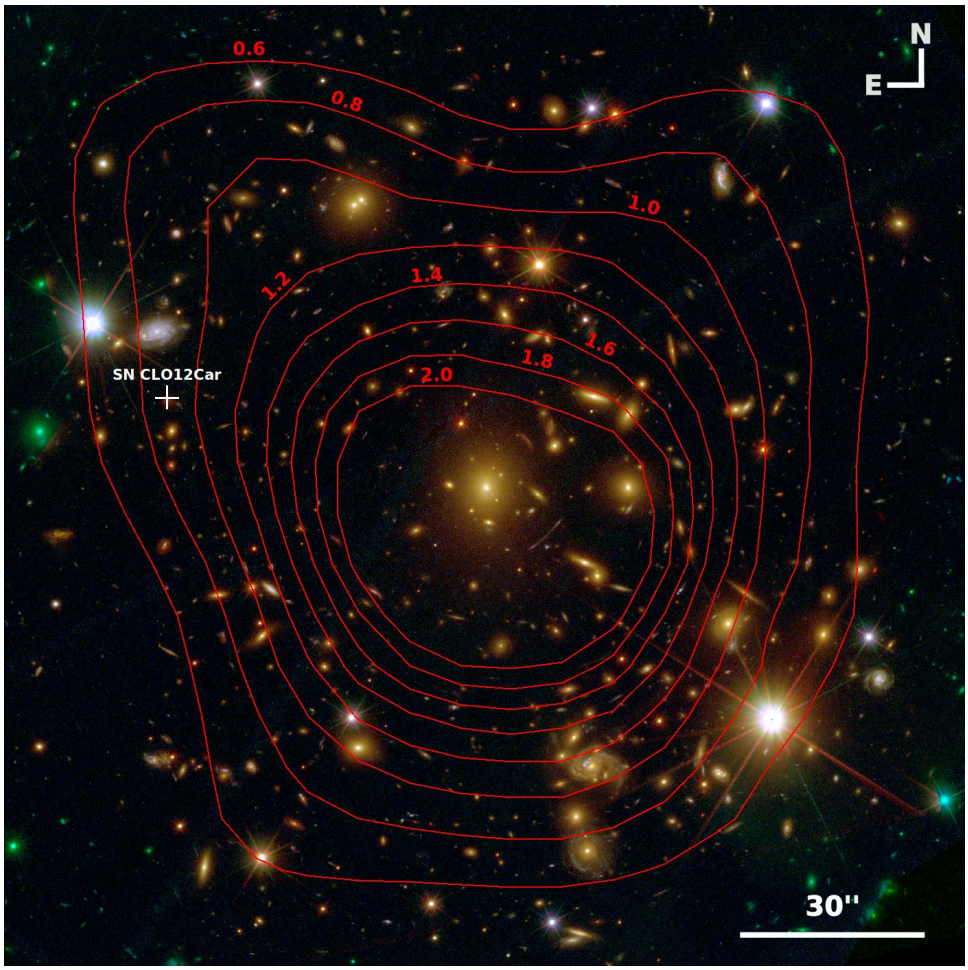

Figure 3.10 Magnification map for SN CLO12Car ($z = 1.281$) behind MACSJ1720.2+3536 ($z = 0.391$). The image shows an RGB false-color background based on 12-band *HST*/CLASH optical and near-IR images of the cluster field. The location of the SN is marked with a white cross. The contours show the magnitude increase induced by the lensing magnification ($\Delta m_\mu = 2.5 \log_{10} \mu$) of the cluster for a source at the SN redshift. The lensing magnification was derived from weak and strong lensing constraints jointly, and computed using the SaWLens lensing reconstruction algorithm (Merten et al. 2009, 2011). Multiple images used for the strong lensing constraints in this system will be presented by Zitrin et al. (in prep.).

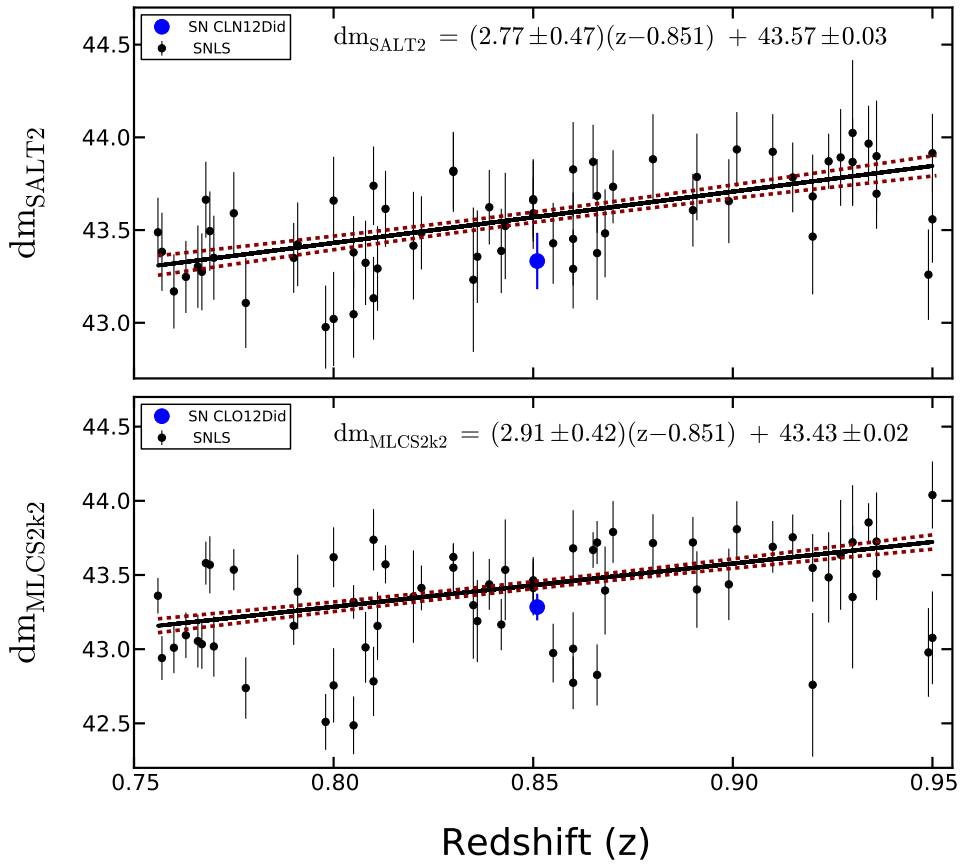

Figure 3.11 Hubble diagrams for SN CLN12Did. As in Figure 3.9, the top and bottom panels show SALT2 and MLCS2k2 fits, respectively. The field comparison sample consists of 63 SNe Ia from SNLS (Guy et al. 2010). Both light-curve fitters suggest slight (but insignificant) magnification for the SN, with $\Delta m_{\mu,\mathrm{SALT2}} = 0.24 \pm 0.15$ mag and $\Delta m_{\mu,\mathrm{MLCS2k2}} = 0.15 \pm 0.09$ mag.

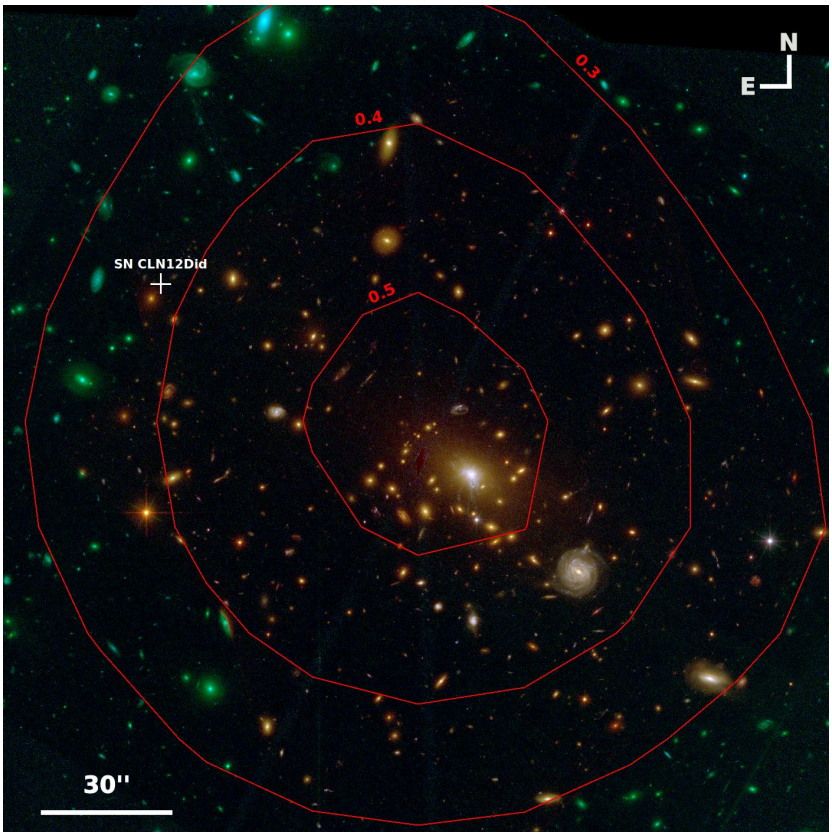

Figure 3.12 Magnification map for SN CLN12Did ($z = 0.851$) behind RXJ1532.9+3021 ($z = 0.345$). Similar to Figure 3.10, the color image is based on CLASH optical and near-IR images, with the SN location marked by a white cross and lensing magnification (Δm_μ, in mag units) shown with red contours. Because RX J1532 is a much weaker lensing cluster than either MACS J1720 or Abell 383, this map was derived using weak lensing constraints alone, computed with the SaWLens algorithm (Merten et al. 2009, 2011). The resolution of the reconstructed map from weak-lensing constraints is much poorer than for the other two clusters, so the displayed contours are heavily smoothed, and the Monte Carlo magnification estimate at the SN position is actually $\Delta m_\mu = 0.28 \pm 0.08$ mag.

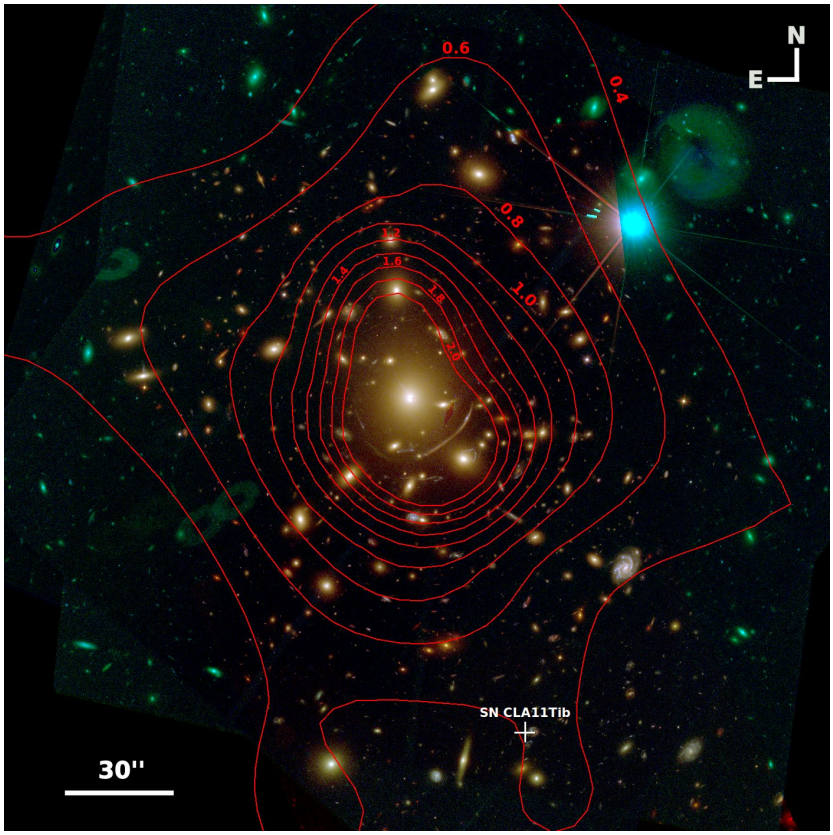

Figure 3.13 Magnification map for SN CLA11Tib ($z = 1.143$) behind Abell 383, similar to Figures 3.10 and 3.12, computed from the SaWLens algorithm (Merten et al. 2009, 2011) from strong and weak lensing constraints. The strong lens multiple images in this system were presented by Zitrin et al. (2011).

3.4.3 SN CLA11Tib

We were unable to classify SN CLA11Tib conclusively (see §3.3.3), so we take a slightly different approach to the analysis for this object. Figure 3.13 shows the predicted lensing magnification map for a source at the redshift of SN CLA11Tib ($z = 1.143$) behind Abell 383. From the map, we derive a lensing magnification for the SN of $\mu = 1.48 \pm 0.15$, which corresponds to $\Delta m_{\mu} = 0.43 \pm 0.11$ mag.

If we assume that SN CLA11Tib was a SN Ia, repeating the analysis above (as for SN CLO12Car and SN CLN12Did) yields magnification estimates for SN CLA11Tib of $\Delta m_{\mu,\mathrm{SALT2}} = 0.52 \pm 0.20$ mag and $\Delta m_{\mu,\mathrm{MLCS2k2}} = 0.64 \pm 0.15$ mag. However, as mentioned

in §3.3.3, the SALT2 light-curve fit is unacceptable, with $\chi^2/\nu = 57.8/14 = 4.13$, making the inferred distance unreliable. The MLCS2k2 light-curve fit ($\chi^2/\nu = 29.8/14 = 2.13$) is much better, and agrees well with the lensing map prediction (within 1σ). However, due to the discrepancy of the goodness of fit between MLCS2k2 and SALT2, we hesitate to definitively classify the SN as a SN Ia.

To compare both SN Ia and CC SN models in the lensing analysis for SN CLA11Tib, we show in Figure 3.14 the goodness-of-fit for both sets of models. The plot gives the best-fit SN Ia results as above, as well as SN II and SN Ib/c templates (restricted to those with $\chi^2/\nu < 5$). For the CC SN templates, STARDUST calculates a magnitude offset Δm (shown also in Figure 3.7) that is required for the best match of the template to the data, and we show this on the abscissa of Figure 3.14.

We found that the best-fitting CC SN models (albeit at $\chi^2/\nu > 3$) from STARDUST were the SN Ic SDSS-017548 and the SN IIP SDSS-018793. The SN Ic and SN IIP models had best-fit model $m_J = 23.52 \pm 0.08$ mag and $m_J = 23.48 \pm 0.08$ mag, respectively. The observed red color of SN CLA11Tib matches the SN Ic model with no relative extinction, but the SN II model requires $A_V = 0.7$ mag. Including this, we find the unextinguished absolute magnitudes of the models are $M_R = -19.34 \pm 0.08$ mag (SN Ic) or $M_R = -20.43 \pm 0.08$ mag (SN IIP). These are quite bright for CC SNe, though some of this could be a result of the lensing magnification. The peak M_R required by both models is much brighter than the original templates; the SN SDSS-017548 and SN SDSS-018793 spectral energy distributions have $M_R = -18.00$ mag and $M_R = -18.55$ mag, respectively. The offset between the template and data (Δm; Figures 3.7 and 3.14) is -1.16 mag for the SN Ic model and -1.18 mag for the SN IIP model. These would be our best estimates for the lensing magnification based on the SN light curve, but an abundance of caution is warranted, as these estimates assume that SN CLA11Tib had the same intrinsic luminosity as the best-fit template, a dubious proposition given the large luminosity scatter of CC SNe (Li et al. 2011b; Drout et al. 2011; Kiewe et al. 2012). Because of this, if we assume a CC SN fit, we cannot

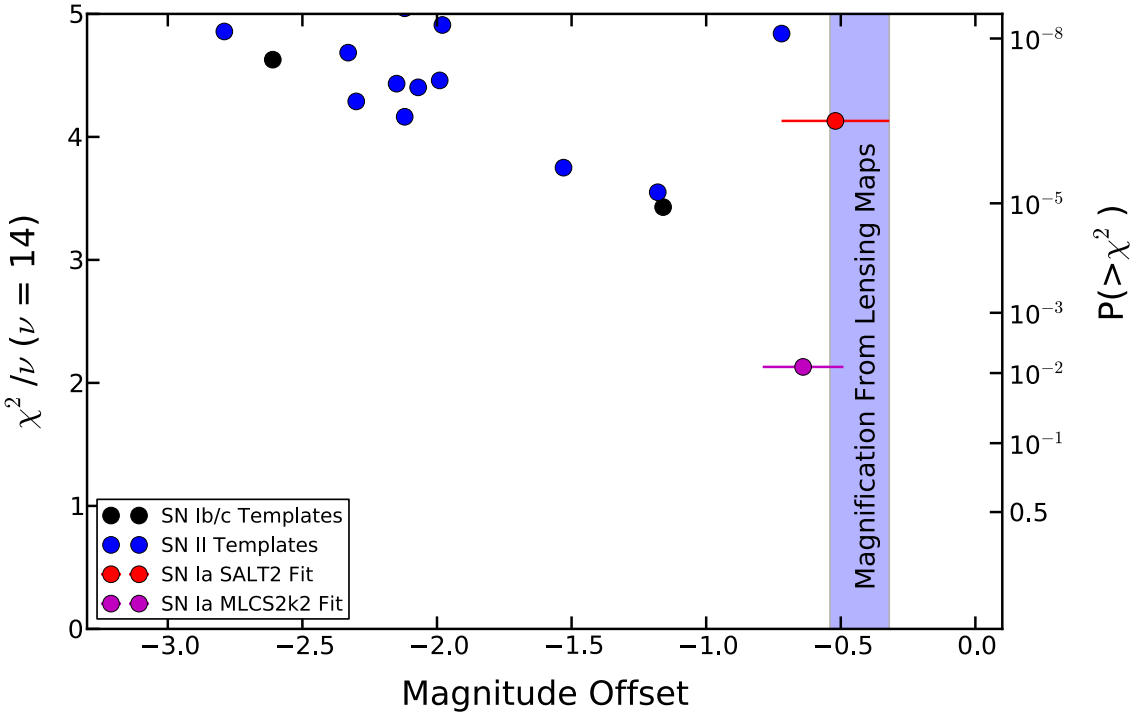

Figure 3.14 Reduced χ^2 (with 14 degrees of freedom) versus magnitude offset for SN CLA11Tib. The magnitude offset is a proxy for Δm_μ from the light-curve fit model, as described in the text. The cumulative probability for a given χ^2_ν value is displayed on the right-hand side. The blue shaded region corresponds to the 1σ range of Δm_μ derived from the lensing map in Figure 3.13. The black and blue points correspond to SN Ib/c and SN II models, respectively, while the red (SALT2) and magenta (MLCS2k2) points are the best-fit SN Ia models. Only the MLCS2k2 fit is consistent with both the SN light curve and the lensing map magnification prediction, but the CC SN templates do not span the full range of CC SN luminosities and light curves.

claim that there is any consistency or inconsistency between the lensing prediction for SN CLA11Tib and its brightness.

3.5 Discussion and Conclusion

SN CLO12Car clearly represents our most exciting result. We find that it is likely a SN Ia at $z = 1.281$, gravitationally magnified by $\sim 1.0 \pm 0.2$ mag. The magnification derived from two independent methods (the SN light curve and the cluster lensing maps), were consistent to within 1σ. SN CLO12Car is the first SN Ia which is both measurably magnified (i.e., with $\Delta m_\mu > 0$ at high significance) and for which the lensing magnification can be precisely and independently derived. SN CLN12Did is also a SN Ia with a consistent (but not significant) supernova-based and model-based lensing magnification, whereas the unclear classification of SN CLA11Tib does not allow for a test of the lens model prediction.

The lens models used here were constructed jointly with both strong-lensing constraints (multiple images) and weak-lensing constraints. In principle, the strong-lensing multiple images directly constrain the deflection field, which is the gradient of the potential, while the weak lensing ellipticity measurements further out constrain the (reduced) shear, a combination of second-order derivatives of the potential. As an alternative to the analysis presented here (where we independently tested the estimated magnifications), lensed standard candles like SNe Ia can play an important role as an additional *direct*, local constraint on the magnification (which is a function of the convergence κ, and the shear γ, both constructed from second-order derivatives of the potential) in the lens model (e.g., Riehm et al. 2011).

Gathering large samples of lensed SNe Ia is clearly of interest. Due to the magnification power of the foreground lenses, lensed SNe could be expected to be seen to higher redshifts than field SNe (for a given limiting magnitude), with applications to extending the redshift coverage of cosmological parameter measurements (if the lensing magnification can be estimated precisely and accurately enough, e.g., Zitrin et al. 2013b) or SN rate measurements to constrain progenitor models (e.g., Graur et al. 2014; Rodney et al. 2014). There is also

the exciting prospect of finding multiply-imaged SNe, with measured time-delays as a new cosmographic constraint (e.g., Holz 2001; Goobar et al. 2002; Oguri & Kawano 2003; Oguri et al. 2003).

SN Ia luminosity distances, combined with lens model magnification estimates (which depend on angular diameter distances to and between the lens and source) or time-delay distances from multiple SN images, could also open up new tests of general relativity (e.g., Daniel & Linder 2010; Jain & Khoury 2010; Schwab et al. 2010) or even fundamental cosmological assumptions, like the distance duality relation (e.g., Lampeitl et al. 2010; Liang et al. 2013).

Though the CLASH survey has ended, the three lensed SNe found behind CLASH clusters herald the promise of many more such discoveries in the near future, including from wide-field ground-based surveys like the Dark Energy Survey (Frieman & Dark Energy Survey Collaboration 2013; Bernstein et al. 2012), Pan-STARRS (Rest et al. 2014, and references therein), and ultimately LSST (LSST Science Collaboration et al. 2009); ground-based surveys that target massive galaxy clusters, such as CluLeSS (Jha et al., in prep.) or SIRCLS (Graham et al. 2013); and targeted space-based surveys like the *HST* Frontier Fields (PI M. Mountain; with SN follow-up observations in program GO-13396, PI S. Rodney). SNe Ia were the key to the discovery of the accelerating Universe; perhaps gravitationally lensed SNe Ia will play a starring role in further illuminating the dark Universe, probing not just dark energy, but dark matter as well.

We would like to thank Rick Kessler for invaluable assistance with SNANA. We are grateful to Jakob Nordin for helpful discussions, and Saul Perlmutter and the Supernova Cosmology Project for communication and coordination.

This research at Rutgers University was supported through NASA/*HST* grant GO-12099.14 and National Science Foundation (NSF) CAREER award AST-0847157 to S.W.J. Support for S.R. and A.Z. was provided by NASA through Hubble Fellowship grants HST-HF-51312.01 and HST-HF-51334.01, respectively, awarded by the Space Telescope Science

Institute, which is operated by the Association of Universities for Research in Astronomy, Inc., for NASA, under contract NAS 5-26555. L.I. thanks Basal/CATA CONICYT funding for support. This research was carried out in part at the Jet Propulsion Laboratory, California Institute of Technology, under a contract with NASA. Support for *HST* programs GO-12065 and GO-12099 was provided by NASA through a grant from the Space Telescope Science Institute, which is operated by the Association of Universities for Research in Astronomy, Incorporated, under NASA contract NAS5-26555. A.V.F. is also grateful for the support of NSF grant AST-1211916, the TABASGO Foundation, and the Christopher R. Redlich Fund. Support for M.N. was provided in part by grant PRIN-INAF 2010.

Some of the observations reported in this paper were obtained with the Southern African Large Telescope (SALT), through Rutgers University program 2011-3-RU-001 (PI C. McCully). This work was supported by a NASA Keck PI Data Award, administered by the NASA Exoplanet Science Institute. Data presented herein were obtained at the W. M. Keck Observatory from telescope time allocated to the National Aeronautics and Space Administration through the agency's scientific partnership with the California Institute of Technology and the University of California. The Observatory was made possible by the generous financial support of the W. M. Keck Foundation. The authors recognize and acknowledge the very significant cultural role and reverence that the summit of Mauna Kea has always had within the indigenous Hawaiian community, and we are most privileged to have the opportunity to explore the Universe from this mountain. This work is based in part on data collected at the Subaru telescope and obtained from the Subaru-Mitaka-Okayama-Kiso Archive, which is operated by the Astronomy Data Center, National Astronomical Observatory of Japan.

Additional data were obtained at the Gemini Observatory, which is operated by the Association of Universities for Research in Astronomy, Inc., under a cooperative agreement with the NSF on behalf of the Gemini partnership: the National Science Foundation

(United States), the National Research Council (Canada), CONICYT (Chile), the Australian Research Council (Australia), Ministério da Ciência, Tecnologia e Inovação (Brazil) and Ministerio de Ciencia, Tecnología e Innovación Productiva (Argentina). The data were taken as part of programs GN-2012A-Q-32 and GN-2013A-Q-25.

Table 3.1: SN CLO12Car Photometry

UT Date	MJD	Instrument	Filter	Exposure Time (s)	Magnitude
2012 May 05	56052.58	ACS	F850LP	991.0	> 25.546
2012 May 05	56052.64	WFC3/IR	F160W	1408.8	> 25.347
2012 May 09	56056.02	WFC3/IR	F105W	1408.8	> 26.016
2012 May 09	56056.04	WFC3/IR	F140W	1005.9	> 25.808
2012 May 22	56069.68	ACS	F814W	1007.0	> 26.666
2012 Jun. 17	56095.66	ACS	F850LP	1032.0	24.597 ± 0.130
2012 Jun. 17	56095.68	ACS	F814W	975.0	25.148 ± 0.082
2012 Jun. 17	56095.73	WFC3/IR	F160W	1408.8	23.451 ± 0.050
2012 Jun. 17	56095.75	WFC3/IR	F110W	1005.9	23.856 ± 0.024
2012 Jul. 02	56110.09	WFC3/IR	F105W	1005.9	23.750 ± 0.042
2012 Jul. 02	56110.15	WFC3/IR	F140W	1005.9	23.271 ± 0.025
2012 Jul. 16	56124.09	WFC3/IR	F105W	1005.9	23.791 ± 0.054
2012 Jul. 16	56124.15	WFC3/IR	F140W	1005.9	23.250 ± 0.025
2012 Jul. 23	56131.31	WFC3/IR	F160W	455.9	23.340 ± 0.063
2012 Jul. 23	56131.38	WFC3/IR	F105W	455.9	24.138 ± 0.056

All supernova photometry is reported in Vega magnitudes. The nondetections are reported as 3σ upper limits.

Table 3.2: SN CLN12Did Photometry

UT Date	MJD	Instrument	Filter	Exposure Time (s)	Magnitude
2012 Feb. 03	55960.64	ACS	F625W	1032.0	26.699 ± 0.171
2012 Feb. 03	55960.65	ACS	F850LP	1017.0	25.066 ± 0.150
2012 Feb. 18	55975.67	ACS	F775W	1032.0	23.041 ± 0.016
2012 Feb. 18	55975.69	ACS	F606W	998.0	24.186 ± 0.017

Table 3.2: SN CLN12Did Photometry

UT Date	MJD	Instrument	Filter	Exposure Time (s)	Magnitude
2012 Mar. 03	55989.84	ACS	F814W	1032.0	23.175 ± 0.015
2012 Mar. 03	55989.86	ACS	F435W	1018.0	> 28.560
2012 Mar. 03	55990.24	ACS	F625W	1032.0	24.182 ± 0.023
2012 Mar. 03	55990.25	ACS	F850LP	1017.0	22.929 ± 0.026
2012 Mar. 03	55990.31	ACS	F475W	1032.0	27.057 ± 0.138
2012 Mar. 03	55990.32	ACS	F775W	1013.0	23.034 ± 0.016
2012 Mar. 03	55990.37	WFC3/IR	F110W	1508.8	22.915 ± 0.013
2012 Mar. 03	55990.39	WFC3/IR	F160W	1005.9	23.041 ± 0.041
2012 Mar. 16	56002.61	ACS	F606W	1032.0	25.491 ± 0.038
2012 Mar. 16	56002.62	ACS	F814W	984.0	23.410 ± 0.018
2012 Mar. 16	56002.67	WFC3/IR	F105W	1305.9	23.138 ± 0.019
2012 Mar. 16	56002.69	WFC3/IR	F140W	1305.9	23.540 ± 0.034
2012 Mar. 18	56004.74	ACS	F475W	1032.0	> 28.924
2012 Mar. 18	56004.75	ACS	F850LP	1001.0	23.359 ± 0.037
2012 Mar. 29	56015.52	ACS	F435W	1032.0	> 28.625
2012 Mar. 29	56015.53	ACS	F814W	1017.0	24.148 ± 0.029
2012 Apr. 12	56029.62	ACS	F850LP	1032.0	24.448 ± 0.079
2012 Apr. 12	56029.63	ACS	F814W	985.0	25.072 ± 0.058
2012 Apr. 12	56029.68	WFC3/IR	F160W	1508.8	23.316 ± 0.038
2012 Apr. 12	56029.70	WFC3/IR	F110W	1005.9	23.853 ± 0.038

All SN photometry is reported in Vega magnitudes. The nondetections are listed as 3σ upper limits.

Table 3.3: SN CLA11Tib Photometry

UT Date	MJD	Instrument	Filter	Exposure Time (s)	Magnitude
2010 Nov. 18	55518.91	ACS	F625W	1032.0	> 27.206
2010 Nov. 18	55518.92	ACS	F850LP	1014.0	> 25.768
2010 Nov. 18	55518.99	ACS	F775W	1010.0	> 26.792
2010 Dec. 08	55538.41	ACS	F850LP	1032.0	> 25.802
2010 Dec. 08	55538.43	ACS	F814W	1060.0	> 26.872
2010 Dec. 28	55558.45	ACS	F435W	1032.0	> 27.385
2010 Dec. 28	55558.46	ACS	F814W	1092.0	24.699 ± 0.049
2011 Jan. 04	55565.97	ACS	F625W	1032.0	25.349 ± 0.074
2011 Jan. 04	55565.98	ACS	F850LP	1092.0	24.251 ± 0.091
2011 Jan. 18	55579.35	ACS	F606W	1032.0	26.364 ± 0.104
2011 Jan. 18	55579.36	ACS	F814W	1059.0	24.394 ± 0.038
2011 Jan. 22	55583.41	ACS	F775W	1032.0	24.762 ± 0.066
2011 Jan. 22	55583.43	ACS	F606W	1073.0	26.551 ± 0.127
2011 Jan. 24	55585.08	WFC3/IR	F105W	806.0	23.755 ± 0.037
2011 Jan. 24	55585.09	WFC3/IR	F125W	806.0	23.402 ± 0.036
2011 Jan. 24	55585.14	WFC3/IR	F160W	906.0	23.357 ± 0.059
2011 Feb. 07	55599.38	ACS	F814W	1032.0	25.082 ± 0.076
2011 Feb. 07	55599.40	ACS	F435W	1093.0	> 27.336
2011 Feb. 21	55613.16	ACS	F850LP	1994.0	25.247 ± 0.188
2011 Mar. 01	55621.43	ACS	F850LP	1076.0	> 25.677

All SN photometry is reported in Vega magnitudes. The nondetections are listed as 3σ upper limits. Dolphot was used to derive PSF photometry for the WFC3/IR observations (see text).

Table 3.4: Comparing SN Magnifications with Lensing Predictions

	Lensing from Light Curve Fits		
SN name	Δm_μ (SALT2)	Δm_μ (MLCS22k)	Δm_μ (Lensing Maps)
SN CLO12Car	0.91 ± 0.25	1.06 ± 0.17	0.83 ± 0.16
SN CLN12Did	0.24 ± 0.15	0.15 ± 0.09	0.28 ± 0.08
SN CLA11Tib	···	···	0.43 ± 0.11

Comparison of lensing predictions from light curve fits and lensing maps for the three SNe. All of the Δm_μ table entries have units of magnitudes. For both SN CLO12Car and SN CLN12Did, there is good agreement (within 1σ) between both lensing methods. The classification of SN CLA11Tib was inconclusive, making it difficult to determine a magnification from the light curve (see §3.4.3).

Chapter 4

Progress Towards A New Light-Curve Fitter

ABSTRACT

In Chapter 4, we discuss some of the systematics that plague current light curve-fitters. We present progress towards a new light curve fitter for SNe Ia, which we call Multicolor Light Curve Shapes 3 (MLCS3). The project has not been completed, but we discuss some of the features, and the expected improvements from MLCS3. With $\sim$ 1000 SNe Ia usable for cosmology, we are currently systematics, not statistics, limited for constraining the equation of state of dark energy. Adding more high redshift ($z \gtrsim 1$) SNe Ia will improve constraints, but these are the most difficult to find. MLCS3 will provide more accurate distance measurements for the SNe Ia using a variety of improvements that have been suggested in the literature. An improved light-curve fitter would help to alleviate the systematics associated with light-curve fitting, and provide better distance estimates for important SNe Ia.

4.1 Introduction

As discussed in §1.1.4, are not standard candles, but rather they are standardizable. Thus, light-curve fitters are essential tools for using SNe Ia as distance indicators. They were integral in the discovery of the accelerated expansion of the Universe (Riess et al. 1998; Perlmutter et al. 1999), and continue to play a central role in constraining dark energy (e.g., Riess et al. 2007; Suzuki et al. 2012; Scolnic et al. 2014a; Sullivan et al. 2011; Kessler et al. 2009a).

There are many light-curve fitters in use today; here, I will describe two widely used fitters, which the majority of the Chapter will focus on. The most ubiquitous fitter is the Spectral Adaptive Light Curve Template 2 (SALT2; Guy et al. 2007, 2010). This fitter is an improvement on the original stretch fitter introduced in Perlmutter et al. (1997). SALT2 uses two parameters, stretch (x_1; representing the width of the light-curve) and color (c; representing how blue or red the SN appears) to fit the full light-curve. Using the two parameters, the distance modulus to the SN can be calculated:

$$\mu = m_{\rm B}^{*} - M + \alpha x_1 - \beta c \tag{4.1}$$

where $m_{\rm B}^{*}$ is the peak observed magnitude in the B band, M is the nominal absolute magnitude, and α and β constants. The first three terms ($m_{\rm B}^{*}$, x_1, and c) are derived from the light-curve. The last three terms (M, α, and β) are determined by fitting a sample of SNe Ia and determining the best fit values.

Another important light-curve fitter is the Multicolor Light Curve Shapes 2 (MLCS2k2; Jha et al. 2007; Jha 2002). This fitter is an improvement on the original (Riess et al. 1996, 1999), which was used in the discovery of the accelerating expansion of the Universe (Riess et al. 1998). MLCS2k2 uses two parameters, delta (Δ representing the over-luminosity or under-luminosity of a SN Ia) and extinction (A_V; measuring the dust extinction to the SN). MLCS2k2 uses a training set to determine the relationship between the peak M_V and the two parameters, thus producing the distance to a SN directly from the fit.

However, systematic uncertainties plague all light-curve fitters, and must be accounted for to improve cosmological constraints (e.g., Scolnic et al. 2014a; Conley et al. 2011; Betoule et al. 2014). With the vast number of SNe Ia usable for cosmology, we are no longer statistics limited. There are two broad categories of systematic uncertainties: instrumental and astrophysical related systematics. In this Chapter, we will explore some of the astronomical systematics uncertainties (§4.2) related to using SNe Ia for cosmology. In the final section,

we comment on the possible solutions that will be incorporated into a new light-curve fitter, Multicolor Light Curve Shapes 3 (MLCS3).

4.2 Current Systematics Associated With Light-Curve Fitters

In this section, we go through a list of astronomical systematics associated with light-curve fitters. Throughout this section, we compare two fitters that are primarily used in SNe Ia analysis: MLCS2k2 and SALT2. While other fitters exist, they often share features of SALT2 or MLCS2k2.

4.2.1 SNe Ia Training Set

All fitters require a set of SNe Ia to base their light-curve corrections on. This training set is the backbone of the fitter, and are used to define light-curve parameters. Jha et al. (2007) required SNe Ia that were well sampled near time of maximum, t_0, with accurate values for the M_V. Moreover, the SNe Ia were required to have $z \gtrsim 0.008$, so that the peculiar velocities of the host galaxies were small compared to cosmological recession velocity. Finally, the host galaxies needed good extinction estimates. The resulting training set for MLCS2k2 included 37 SNe, covering UBVRI filters, which were low redshift ($z < 0.1$). To fit SNe Ia and determine distances, the light-curves needed to be transformed into these rest frame filters using K-corrections. This could be a difficult process (e.g., Kessler et al. 2009a; Hsiao et al. 2007).

In developing SALT2, Guy et al. (2007) also required the training SNe Ia to have well sampled light-curves near maximum (so as to measure t_0 and m_B^* accurately). However, SALT2 had an expanded set of SNe Ia to train on, including 173 SNe Ia that in the range $0.003 \leq z \leq 0.952$. Moreover, unlike MLCS2k2, SALT2 used a parameterized model of the SN Ia SED based on templates. This removed the need for K-corrections, instead using the warped SED at the redshift of the SN to match the observed filters. SALT2 was better suited to analyze modern surveys with lots of high redshift SNe Ia, as its training sample

was larger and covered a wider redshift range than MLCS2k2. For this reason, it has been used in the most recent SNe Ia cosmology publications over MLCS2k2 (i.e., Sullivan et al. 2011; Betoule et al. 2014; Rest et al. 2014).

However, SALT2 has several drawbacks (many of these are discussed in §4.2.2 and §4.2.3), including its wavelength coverage (the wavelength coverage is 2800 Å to 7000 Å). At a maximum wavelength of 7000 Å, SALT2 cannot fit the rest I band or longer wavelength fitters. We saw this problem in Chapter 3; we needed to extrapolate the Guy et al. (2010) SALT2 model to fit our observed data.

The wavelength coverage is particularly important on the high end, as SNe Ia are nearly standard candles in the near infrared (NIR) (Wood-Vasey et al. 2008). The light-curve fitter SNooPy (Burns et al. 2011) was recently developed by the The Carnegie Supernova Project (CSP). SNooPY uses two parameters to fit SNe Ia. The first is a Δm_{15} parameter, analogous to $\Delta m_{15}(B)$ from Phillips (1993), though calculated in a slightly different way. The second is A_V which accounts for dust extinction along the line of sight (which has the effect of reddening the SN). The derived distances for the SNe Ia comes directly from the light-curve fit. The fitter is unique in its ability to handle rest NIR filters. This will be a requirement of any complete fitter as we collect more data at these longer wavelengths.

At shorter wavelengths, the U band anomaly (see Krisciunas et al. 2013; Burns et al. 2014) is a problem that continues to plague SNe Ia. SNe Ia surveys have found that there is much more scatter in the Hubble diagrams for the U band as compared to optical and IR filters (e.g. Kessler et al. 2009a; Betoule et al. 2014). For this reason, most cosmological studies exclude U band data (e.g., Kessler et al. 2009a). There are several explanations for the U band issues. There is good evidence that the U band has not been calibrated well in older surveys, which could lead to the discrepancy (Kessler et al. 2009a; Krisciunas et al. 2013). MLCS2k2 struggles with fitting the U band more than SALT2 (Kessler et al. 2009a), which would be consistent with a calibration issue as MLCS2k2 is trained on 37 low redshift SNe Ia with U band data. SALT2 has less trouble with the U band as it is has

a larger training set with a wider redshift range. However, Burns et al. (2014) has found similar U band issues in the CSP data, which is an ongoing survey that has taken great pains to properly calibrate the U band. This would point to a intrinsic difference between low and high redshift SNe Ia spectra.

There is evidence that the UV spectra of SNe Ia evolve with redshift (Foley et al. 2012). Foley et al. (2012) compared the spectra of several nearby and intermediate redshift (at mean $z = 0.22$) SNe Ia. They found that the UV properties were different between the intermediate and low redshift SNe Ia that had similar optical properties. This would indicate that the two groups of SNe Ia are intrinsically different, or there is a selection effect. Other groups have confirmed the UV difference between low and intermediate redshifts (e.g., Maguire et al. 2012). However, Maguire et al. (2012) find, in contrast to Kessler et al. (2009a) and other cosmological studies, that the UV differences do not correlate with Hubble diagram residuals. Whatever the cause, there is great consensus that the U band must be handled in a better way by light-curve fitters (Kessler et al. 2009a; Scolnic et al. 2014a; Betoule et al. 2014).

4.2.2 SNe Ia Host Galaxy Properties

An important systematic discovered in recent years is the effect of host galaxy environment on SNe Ia absolute magnitudes (e.g., Sullivan et al. 2010; Lampeitl et al. 2010; Kelly et al. 2014a). Lampeitl et al. (2010) found that SNe Ia in early type galaxies (with low star formation rates) are brighter than those in star-forming galaxies by 0.09 mag across a redshift range. This difference was seen after SALT2 light-curve fitting, indicating that the α and β parameters may vary with the host-galaxy type. The cause of the discrepancy is unknown. Some have suggested that the metallicitiy or age of the progenitor population leads to the difference in absolute magnitudes (see Childress et al. 2014).

Although the difference in magnitude seems relatively small, the resulting uncertainties in cosmological fits are large (Sullivan et al. 2010). Modern SNe Ia surveys account for

this effect by having two host mass regimes with different absolute magnitude values (e.g., Sullivan et al. 2011; Betoule et al. 2014; Conley et al. 2011). Larger masses (stellar mass greater than $10^{10} M_{\odot}$) correspond to the passive galaxies, and smaller stellar masses to star-forming galaxies. This change has the desired effect of minimizing the systematic uncertainty produced from host galaxy mass. However, for some SNe Ia, we do not have information on the host. This is particularly true for high redshift SNe Ia, which may not have visible host galaxies. The correction in its current form cannot be applied to these SNe Ia.

4.2.3 SNe Ia Colors

The relationship between SNe Ia colors and luminosity is very important for light-curve fitters. MLCS2k2 and SALT2 take different approaches to addressing SNe Ia color. MLCS2k2 assumes that the color comes from two forms; the first is intrinsic scatter in luminosity in different filters (Jha et al. 2007). This scatter is not correlated with the absolute magnitude of SNe Ia. The second effect that changes observed colors of SNe Ia is dust extinction, and is represented in the model as $R_V = A_V/E(B\text{-}V)$. Thus, in the MLCS2k2 model, SNe Ia can be reddened by dust. However, blue SNe Ia are a result of intrinsic scatter. The R_V becomes the color-correlation $R_V = 3.1$ for Galactic dust. The value of R_V is fixed to 3.1 in the initial presentation of MLCS2k2 (Jha et al. 2007). Several studies showed that lower values of R_V were favored for MLCS2k2 (Kessler et al. 2009a; Hicken et al. 2009). This would imply that SNe Ia host galaxies had a different dust law than the Milky Way.

SALT2 approach to color is straight forward; the model does not distinguish intrinsic color from dust extinction (Tripp & Branch 1999). SALT2 uses a simple constant color-correction term β modifying the color term (Guy et al. 2007, 2010). The approach assumes that the Typical value recovered for β is ~ 3.1 (Guy et al. 2010; Conley et al. 2011). However, several studies noted that the value of β seemed to change at different redshifts (e.g., Kessler et al. 2009a; Guy et al. 2010). As stated earlier, SALT2 is the preferred fitter

and the evolution of this color term is typically added into the systematic error budget in cosmological studies.

Recently, the color term has been studied in depth by Scolnic et al. (2014b). They looked at a sample of blue and red SNe Ia taken from the SDSS, SNLS, and other low redshift surveys. They found that attributing the scatter in SNe Ia distances to color instead of luminosity, the data supported a value of $\beta = 4.1$ (which is consistent with a Milky Way extinction law of $R_V = 3.1$). This is shown visually in Figure 4.1, which is taken from Scolnic et al. (2014b). The three plots are Hubble residual diagrams vs color. The top panel shows the real SNe Ia data, with the distance modulus calculated using and $\beta = 3.1$. The plot indicates that the SNe Ia with c >0 (red line) and c<0 (blue line) have different best fit β values. This behavior is inconsistent with a constant β term, which is built into the SALT2 model. Moreover, a Milky Way dust approach, similar to how MLCS2k2 handles color, predicts a similar bifurcation (though, not exact) to what's observed in real SNe Ia data. The changing value of β has a significant effect on cosmological values derived from SNe Ia.

Scolnic et al. (2014b) demonstrates that a simple linear color parameter does not completely describe SNe Ia. We must separate out the intrinsic color variations from dust extinction to fully correct SNe Ia light-curves. While a Milky Way extinction law can correct for dust, intrinsic variations are harder to model. One recent development is the use of line velocities to categorize intrinsic color of SNe Ia (Wang et al. 2009b; Foley et al. 2011; Mandel et al. 2014). The line velocities can be measured from the spectra of SNe Ia; these spectra are readily available, as SN surveys spectroscopically confirm as many of their SNe Ia as possible. There seems to be a correlation between the velocity at maximum of the Si II line and the intrinsic color of SNe Ia; specifically, redder SNe Ia seem to have higher velocities of Si II Wang et al. (2009a); Foley et al. (2011). The correlation exists, but is less pronounced in other spectroscopic lines (Foley et al. 2012; Wang et al. 2009a; Mandel et al. 2014). Specifically, Foley et al. (2011) found that the B-V color of extinction

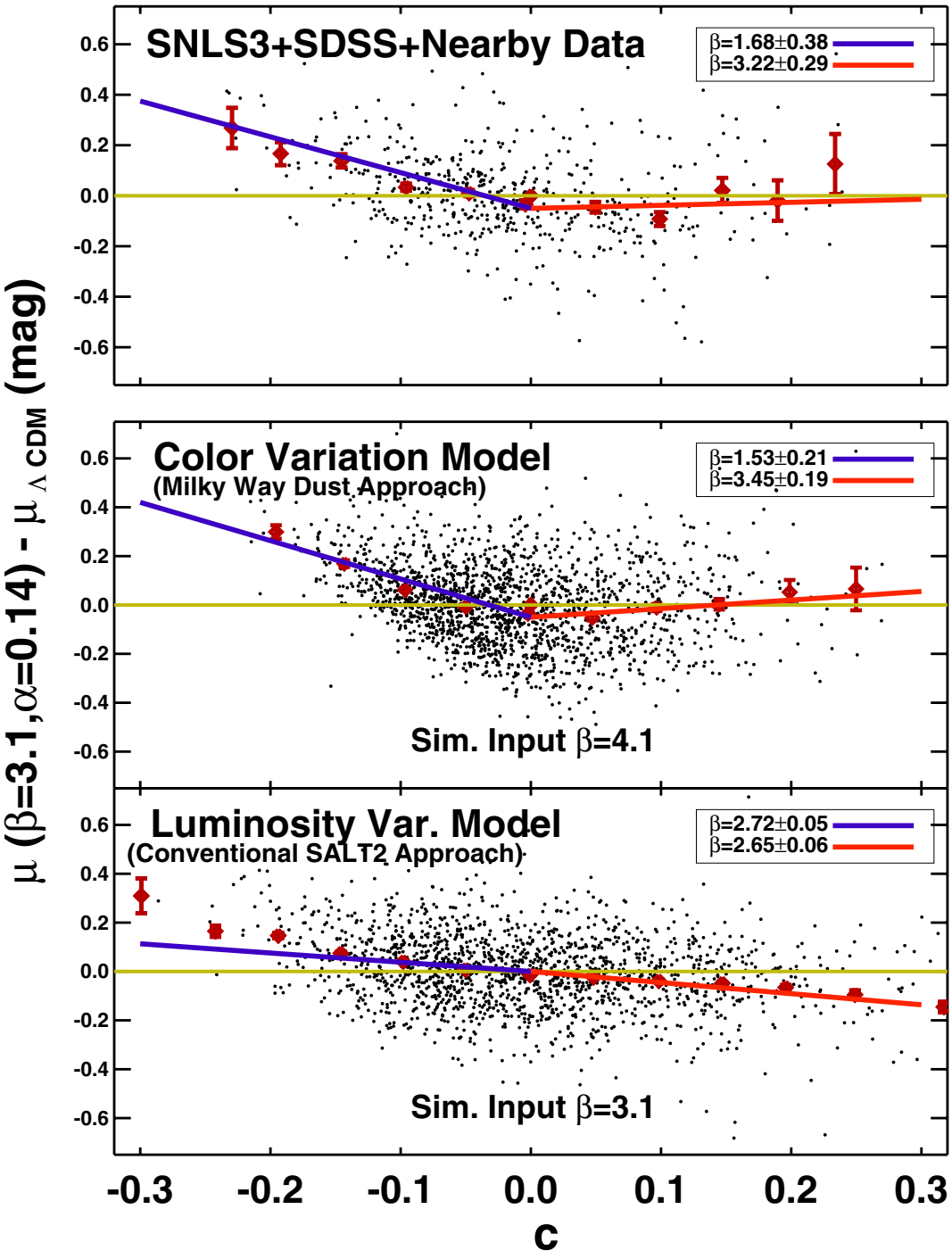

Figure 4.1 Figure from Scolnic et al. (2014b). The plots are of Hubble residual vs. color. The top panel shows real SNe Ia data, with the best fit β values for c$<$ 0 and c$>$0 SNe Ia. The middle and bottom plots show simulations from color and luminosity variation models. The color variation model is similar to the method used by MLCS2k2, where as the luminosity variation model represents the conventional SALT2 approach. Note, neither the MLCS2k2 or the SALT2 approach produce the slopes derived from the real data, but the MLCS2k2 approach is close.

corrected SNe Ia was linearly correlated with the velocity of the Si II line. Thus, given the spectral information, we can hope to correct for both dust and intrinsic color to produce more accurate distances.

4.3 Progress Towards A New Light-Curve Fitter: MLCS3

In this section, we discuss a new light-curve fitter we have be working on called MLCS3. The most important change from MLCS2k2 that will be incorporated into MLCS3 is a larger training sample. Figure 4.2 shows a histogram plot of 1055 SNe Ia that have light-curve fits with MLCS2k2. These SNe Ia will make up the training set. They span a wide range of A_V and Δ values, and are more representative of SNe Ia as a whole compared to the previous training sample. We have made some initial cuts to the sample, requiring 3 or more filters for each epoch and good coverage near maximum. The combination of these two cuts dropped the training sample to 423. Although many SNe Ia were cut, the sample is larger than the 203 SNe Ia used by Betoule et al. (2014) in the retraining of the SALT2 fitter for the joint SDSS/SNLS cosmology analysis. Also, Betoule et al. (2014) restricted their training sample to $z < 0.25$, where as we do not make any redshift cuts.

We have decided to use the SALT2 approach of creating a SN Ia SED rather than using model light curves. This is done by warping the Hsiao et al. (2007) SN Ia template to match an observed SN at each epoch of observations. First, the template is reddened using the A_V value from the MLCS2k2 fit. The output is then warped to match the input photometry from multiple filters for each epoch. We show a warped spectrum of SN 2007af at peak in Figure 4.3. We also plot the CSP photometry on the spectrum, which covers the near-UV to the near-IR in wavelength. The colored points and error bars represent the wavelength coverage of each filter.

Next, the SNe Ia are normalized; we chose to normalize the SEDs to so that the peak $M_V = -19.5$. At the end of the process, each SN produces an SED at each phase and the SEDs would be averaged together to form a ModelSED for light-curve fitting. The normalized

SNe Ia are diverse (see Figure 4.4), and are a good representation of SNe Ia in general. We are confident that they will provide a comprehensive ModelSED.

We may relax our requirements for the training sample later in the process when we test our results. Moreover, we will include additional SNe Ia to train on, which should expand our coverage of the near-UV and near-IR. The SNe Ia in the rest near-UV have photometry from *Swift* (Brown et al. 2010). The rest near-IR SNe Ia will come from various ground surveys (e.g, Wood-Vasey et al. 2008; Friedman et al. 2014; Foley et al. 2013).

We expect MLCS3 to be a major improvement over currently light-curve fitters. With the expanded training set, we should be able to minimize the effects of the U band issues suffered by MLCS2k2. The larger, more representative training sample should significantly improve cosmological results.

Moreover, we will incorporate the results of Scolnic et al. (2014b) into the MLCS3. The new fitter will have two color parameters: one to deal with dust and another to deal with intrinsic color variation. We will use a Milky Way extinction law to explain the dust reddening. We will also have a parameter correlating intrinsic color with line velocity.

We will also incorporate the host galaxy properties directly into the light-curve fitters. We will have a host galaxy parameter in MLCS3, so as to correct this systematic. We will also include a correlation between light-curve and host galaxy properties. This will allow us to correct the light-curves of SNe Ia without host galaxy information.

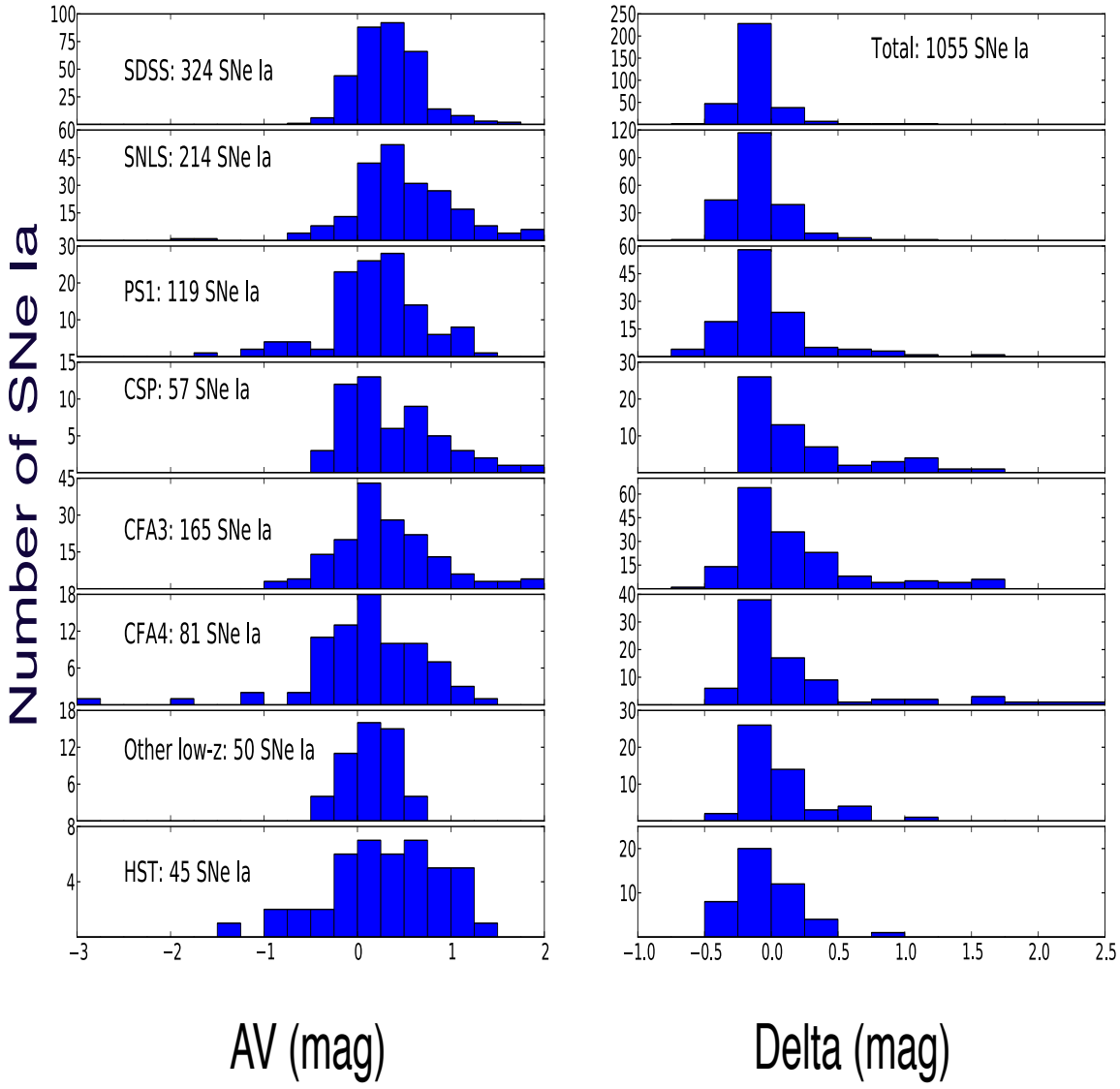

Figure 4.2 Histograms of color, represented by A_V and light-curve shape Δ for various SNe Ia surveys. These SNe Ia will be incorporated into training of MLCS3. The data come from SDSS (Sako et al. 2014), SNLS (Betoule et al. 2014), Pan-Stars (PS1 Rest et al. 2014), CSP (Stritzinger et al. 2011), CFA3 (Hicken et al. 2009), CFA4 (Hicken et al. 2012), other low-z SNe Ia (see Jha et al. 2007), and HST (Riess et al. 2007; Suzuki et al. 2012).

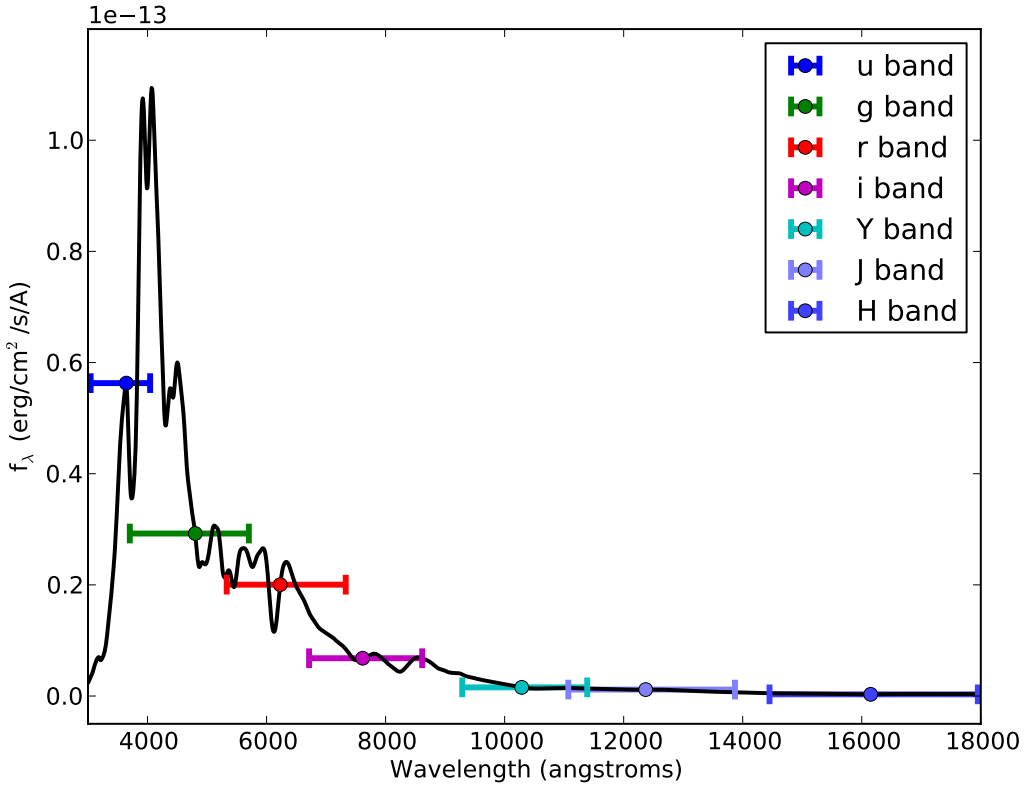

Figure 4.3 Warped spectrum of SN2007af at maximum (t=0). We over-plot the CSP photometry for the SN in the u, g, r, i, Y, J, and H bands. The colored points and error bars represent the wavelength coverage of each filter.

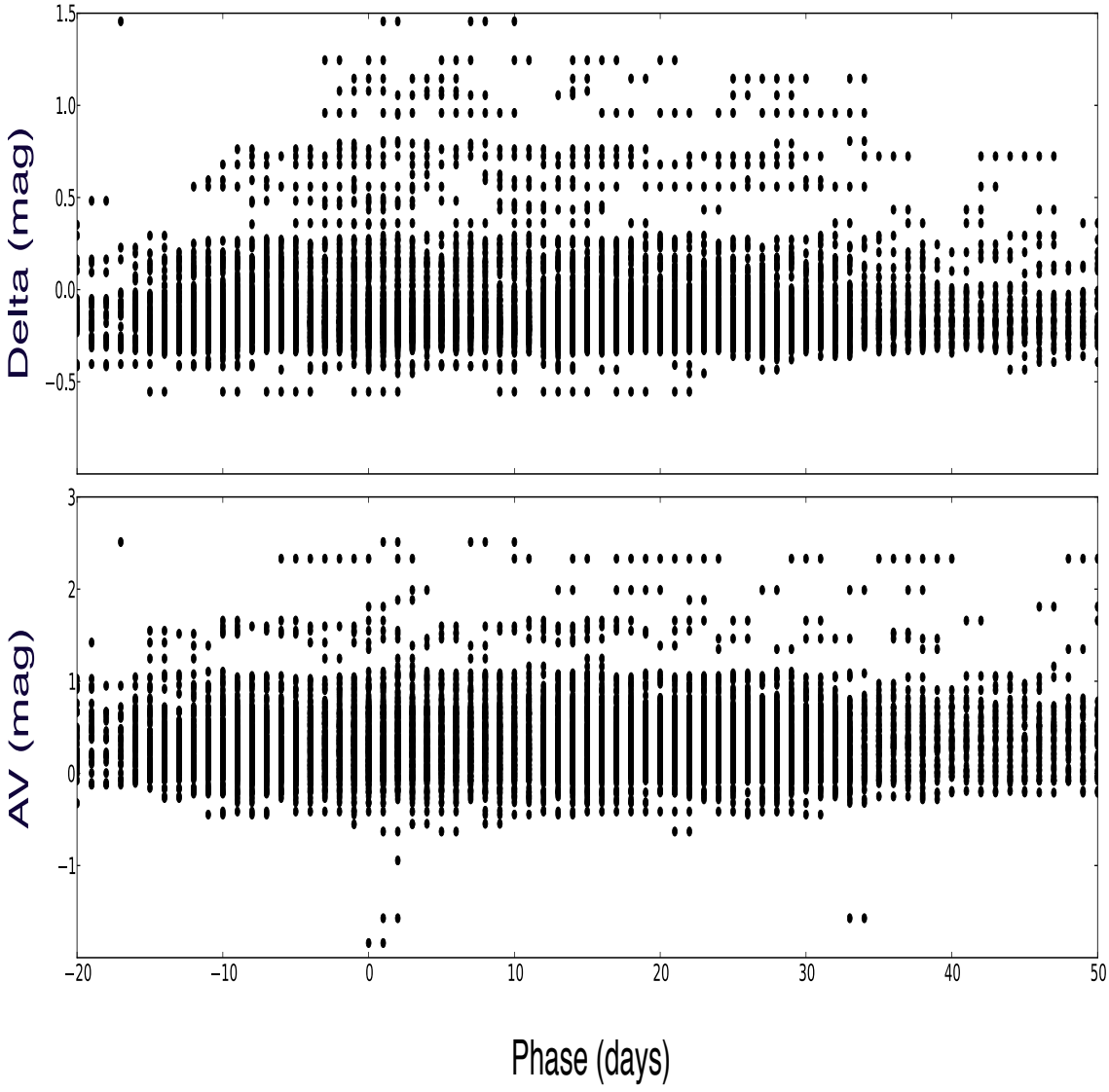

Figure 4.4 Figure of Δ and A_V vs. phase for the 423 normalized SNe Ia in our training sample. Each point represents an SN Ia SED at a particular phase.

Chapter 5

Summary and Current Work

This thesis presented a study of SNe Ia and their progenitors. The results of this work are summarized below. This chapter concludes with a discussion of a recently discovered lensed SNe from the Hubble Frontier Fields (HFF).

In Chapter 2, we explored an interesting SSS, r1-25. The source is located close to the center of M31 ($\sim 0.4'$), and has been well observed. Although mostly in a quiescent phase, there were four bright *Chandra* detections of r1-25. From these observations, we determined that the source started as an SSS, and was later detected as a QSSs. Quasisoft states in a source that has been observed as an SSS represent a newly-discovered phenomenon. We show how such state changers could prove to be examples of unusual black hole or neutron star accretors. However, we note that no WD models are consistent with the behavior of r1-25. We are confident that the source is not a NB WD; i.e., it is not a SNe Ia progenitor. This was an important discovery, as SSSs and QSSs are generally associated with WDs. In Patel et al. (2013) we showed that certain BH and NS models must be considered when analyzing these X-ray sources. Future observations of this and other state changers can provide the information needed to determine the nature(s) of these intriguing new sources.

In Chapter 3, we study three lensed SNe discovered behind galaxy clusters in CLASH. These objects, SN CLO12Car (z= 1.28), SN CLN12Did (z = 0.85), and SN CLA11Tib (z = 1.14), are located behind three different clusters, MACSJ1720.2+3536 (z = 0.391), RXJ1532.9+3021 (z = 0:345), and Abell 383 (z = 0.187), respectively. Based on photometric classification, we found that the first two were likely SNe Ia, while the classification of the last is inconclusive. Using light curve fits from two fitters, we determined a standardized SN

Ia luminosity distance for the two SNe Ia. SN CLO12Car was ~ 1.0 mag brighter than field SNe Ia at a similar redshift and ascribe this to gravitational lens magnification. Similarly, SN CLN12Did was magnified, but also consistent with no lensing ($\sim 0.2 \pm 0.2$ mag brighter than field SNe Ia). We compare these lensing results to those calculated using the CLASH lensing maps. We find that the two independent methods produce similar magnification estimates for the SNe Ia. The two SNe Ia provide a new test of the cluster lens model predictions, and open the door for similar analysis of other lensed SNe Ia.

Finally, in Chapter 4 we discuss systematics that plague current light curve-fitters. We present progress towards a new light curve fitter for SNe Ia, which we call Multicolor Light Curve Shapes 3 (MLCS3). The project has not been completed, but we discuss some of the features, and the expected improvements from MLCS3. With ~ 1000 SNe Ia usable for cosmology, we are currently systematics, not statistics, limited for constraining cosmology. Adding more high redshift ($z \gtrsim 1$) SNe Ia will improve constraints, but these are the most difficult to find. Moreover, not all are suitable for cosmology, as some will be lensed by a significant amount. MLCS3 will provide more accurate distance measurements for SNe Ia using a variety of improvements that have been suggested in the literature. The biggest improvement will be an increased sample of SNe Ia to train the fitter. The training process is vital for the fitter to derive accurate distances. For comparison, MLCS2k2 was trained on 37 low redshift SNe Ia, where as MLCS3 will have hundreds of SNe Ia with arbitrary redshifts.

5.1 Distances to High Redshift SNe Ia

Chapter 4 focused on the need of a new light-curve fitter to beat down systematic uncertainties for cosmological fits. However, there are other uses of fitters, such as providing accurate distances to important SNe Ia. As discussed in Chapter 3, gravitationaly lensed SNe Ia are of particular interest. With so few discovered, providing accurate distances to individual lensed SNe Ia is vital for testing the lensing models.

Moreover, nearby SNe Ia are also important (see §1.1.2 for a discussion of nearby SN 2011fe). SN 2014J was the closest SNe Ia in decades. Located in M82, SN 2014J was a normal SN Ia (Goobar et al. 2014). However, as the SN is very red ($A_V = 1.85$; Amanullah et al. 2014) and has lots of NIR imaging, SALT2 could not provide a light-curve fit. The distance estimates and light-curve parameters were derived using SNooPy. Although not particularly useful for constraining dark energy, nearby SNe Ia are important. When combined with Cepheids, they provide an means of measuring H_0.

Additionally, high redshift SNe Ia ($z \gtrsim 1$) require accurate distances. SNe Ia are systematics limited, but not above z of 1. These SNe Ia are difficult to find, and we do not have the luxury to discard them. Table 5.1 (adapted from Suzuki et al. (2012)) shows the constraints on $w(z) = w_0 + w_a/(1+z)$ (note, w_0 = -1 and $w_a = 0$ transforms this equation to standard ΛCDM cosmology) from SNe Ia at different redshift bins. The constraints come from a combination of SNe Ia and other astronomical measurements (from the CMB and BAO galaxies). At $z < 0.5$, w(z) is very well constrained. However, for $1.0 < z < 1.6$, w(z) can take on a range of values. Although the constraints are worse when considering systematics, the statistical uncertainties on this bin are quite large. This is due to lack of SNe Ia available to constrain the equation of state. Adding just 30 well measured SNe Ia at $z > 1$ will improve the uncertainty by ∼20% (Salzano et al. 2013).

An example of these high redshfit SNe Ia is SN UDS10Wil (Jones et al. 2013), discovered in the Cosmic Assembly Near-infrared Deep Extragalactic Legacy Survey (CANDELS). SN UDS10Wil was the the most disant SN Ia ever discovered at z= 1.914. Figure 5.1, taken from Jones et al. (2013), shows the light-curve fit for the SN, along with a Hubble residual plot. Note, there are only two other confirmed SNe Ia above z = 1.5; the other two are at z=1.71 (Rubin et al. 2013), and z=1.55 (Rodney et al. 2012).

The light-curve parameters for SN UDS10Wil are typical of SNe Ia; we derive values of $x_1 = -1.50 \pm 0.51$ and $C = -0.071 \pm 0.11$. However, due to uncertainty with the light-curve fitter, we also fit the light-curve with MLCS2k2. We found that both fitters produced similar

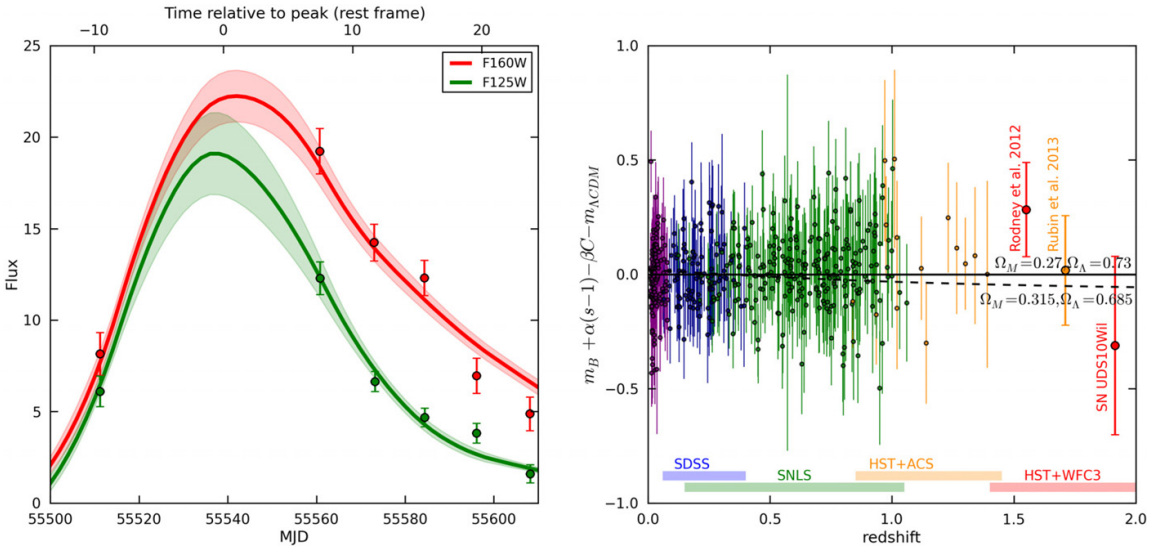

Figure 5.1 Figure from Jones et al. (2013). On the left, the SALT2 light-curve fit to SN UDS10Wil. SALT2 gives a normal set of light-curve parameters along with a corrected magnitude of 26.15 ± 0.39 (consistent with ΛCDM) and a reduced χ^2 of 1.5. On the right, we place SN UDS10Wil on the Hubble residual diagram using cosmological parameters from Sullivan et al. (2011) and $H_0 = 71.6\,\mathrm{km\,s^{-1}\,Mpc^{-1}}$. For comparison, we also show the compilation of $\sim$ 500 SNe from Conley et al. (2011). Lastly, using Sullivan et al. (2011) values for α and β, we include the other two SNe Ia with spectroscopic evidence for classification discovered at a redshift greater than 1.5 (Rodney et al. 2012; Rubin et al. 2013). The dotted line indicates the difference in $m_{\Lambda CDM}$ when using the recent cosmological parameters from the Planck collaboration ($\Omega_\Lambda = 0.685$, $\Omega_M = 0.315$; Planck Collaboration et al. 2014).

distances, with SALT2 providing a slightly larger distance modulus. The distances, as can be seen in Figure 5.1, are consistent with ΛCDM cosmology, though a slightly lower. After a thorough lensing analysis for the SN, we found that the SN was magnified by a min imal amount ($0.030^{+0.024}_{-0.013}$ mag). We are confident in the distance measurements from SALT2 and MLCS2k2. However, the hope would be that MLCS3, with an expanded training set, would provide more reliable distances to high redshift SNe Ia like SN UDS10Wil.

5.2 Recent SNe Discoveries from HFF

Table 5.1: Constraints On w At Various Redshifts

		z < 0.5	0.5 < z < 1.0	1.0 < z < 1.6
w(z)	Stat Only:	$-1.013^{+0.067}_{-0.069}$	$-0.78^{+0.58}_{-0.68}$	$-3.7^{+2.2}_{-4.4}$
	w/ Sys:	$-1.006^{+0.110}_{-0.113}$	$-0.69^{+0.80}_{-0.98}$	$-3.9^{+3.2}_{-8.2}$

Table adapted from Suzuki et al. (2012).

After the success of the CLASH survey, a follow up *HST* survey was approved: HFF. HFF is a multi-cycle program that will image as many as six galaxy clusters. Each galaxy cluster will be observed for 140 orbits: 70 orbits with ACS (in the F435W, F606W, and F814W filters) and 70 with WFC3 (in the F140W, F160W, F125W, F105W filters). The observations will be taken between 2013-2015. With more orbits than CLASH, and fewer filters and galaxy clusters to observe, HFF will go deeper and make many new exciting discoveries.

SN HFF14tom

One such discovery is a lensed SN Ia, SN HFF14tom (Rodney et al., in prep). We approach the analysis of SN HFF14tom in a similar fashion we did the three lensed CLASH SNe (see Chapter 3). SN Tomas was found behind the Abell 2744 cluster in May 2014, and is located about 35″from the bright central galaxy of the cluster. This puts the SN in the strong lensing regime (see Figure 5.2).

We obtained photometry of the SN in 5 *HST* bands (F606W, F814W, F105W, F125W, and F160W). We also obtained *HST* ACS G800L grism data, and analyzed the spectrum. From the spectrum, we determined the SN type (SN Ia) and redshift (z = 1.33 ± 0.02). Note, this redshift is very similar to SN CLO12Car (z=1.281 ± 0.001). We then used SALT2 and MLCS2k2 to fit the light-curve (see Figure 5.3, showing the MLCS2k2 fit). The two fitters produce consistent results, with A_V = 0.033 ± 0.049 and Δ = -0.075 ± 0.098, and x1 = 0.283 ± 0.205 and c = -0.104 ± 0.025. However, MLCS2k2 fit the data better, with

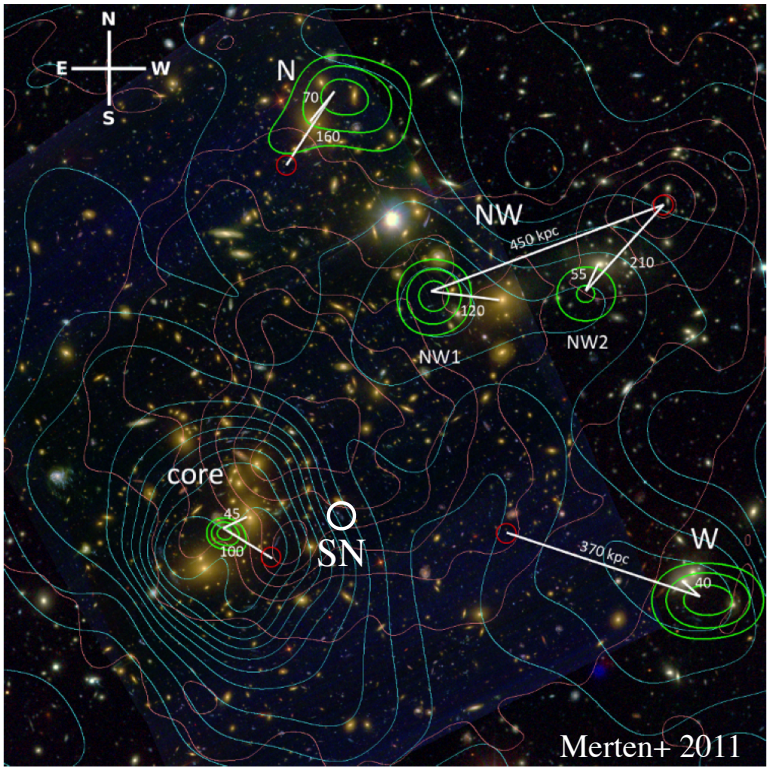

Figure 5.2 Figure taken from Merten et al. (2011). The false color image is a combination of *HST* and ground data (from the VLT and Subaru telescopes) of Abell 2744. The figure demonstrates the gravitational lensing surrounding the galaxy cluster. The location of the SN is marked with a white circle. The surface mass density contours most concentrated in the core area are overlaid in cyan. The magenta contours represent the the more evenly distributed X-ray luminosity. The green contours represent the peak positions of the core, N, NW and W clumps.

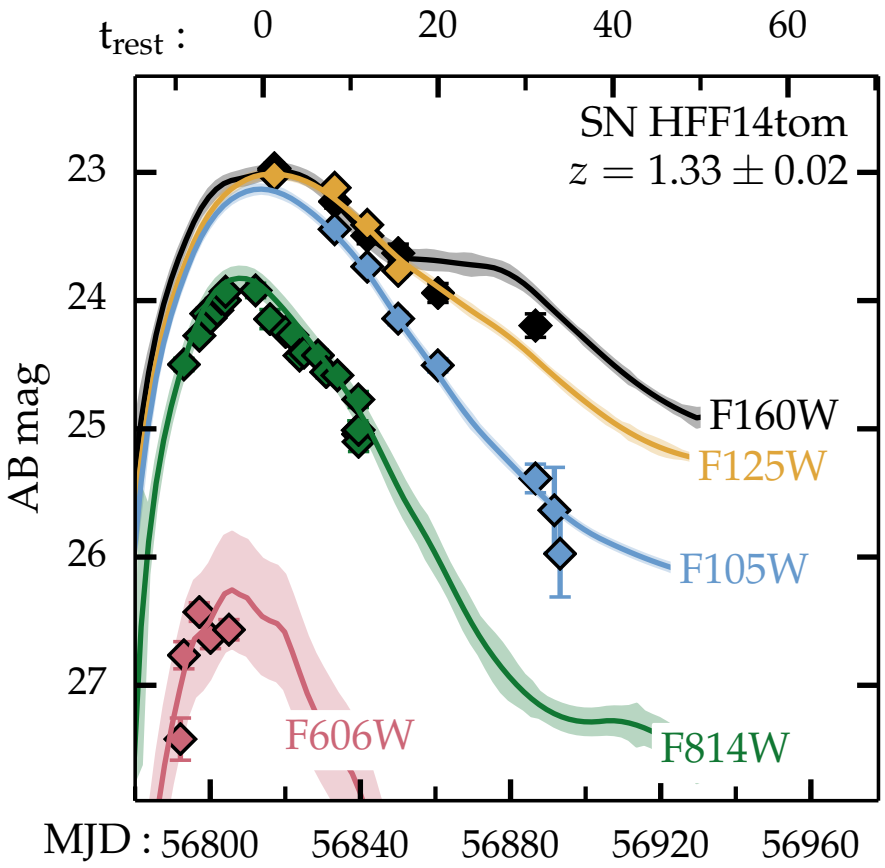

Figure 5.3 MLCS2k2 light-curve fit for SN HFF14tom. The data are well matched by the model, with $\chi^2/\nu = 0.75$

$\chi^2/\nu = 0.75$ (for SALT2, $\chi^2/\nu = 1.49$). They also produced similar distance moduli, with $\mathrm{dm}_{\mathrm{MLCS2k2}} = 44.14 \pm 0.11$ and $\mathrm{dm}_{\mathrm{SALT2}} = 44.13 \pm 0.16$.

Following the approach from Chapter 3, we used field SNe Ia to determine the magnification for SN HFF14tom. We used 18 field SNe from Riess et al. (2007) and Suzuki et al. (2012) to derive the lensing results (these are the same field SNe Ia used in the analysis of SN CLO12Car in Chapter 3). In Figure 5.4, we display two Hubble diagrams for the SN. At z = 1.33, we find that the typical field SN Ia has $\mathrm{dm}_{\mathrm{MLCS2k2}} = 44.85 \pm 0.05$ and $\mathrm{dm}_{\mathrm{SALT2}} = 44.80 \pm 0.08$. Thus, $\Delta m_{\mu,\mathrm{MLCS2k2}} = 0.71 \pm 0.12$ mag and $\Delta m_{\mu,\mathrm{SALT2}} = 0.67 \pm 0.21$ mag. The SN lensing results produced by SALT2 and MLCS2k2 are nearly *identical*

(which was not the case for the two lensed CLASH SNe Ia, see Table 3.4)!

We now turn to the gravitational lensing models for Abel 2744 to provide an independent estimate of the magnification of SN HFF14tom. Since the SN was located near strong lensing features (see Figure 5.2), more lensing models were available to use than for the CLASH SNe Ia. Figure 5.5 shows the lensing results from eight different models. The 8 models produce similar, but not identical, magnification predictions. Each of the horizontal lines represents the 1σ uncertainty range on the magnification prediction from one of the models. The dots represent the median value of the magnification prediction for each model. The position of the 'x's represent the magnification that is most favored by each model. The black line indicates the magnification results from the MLCS2k2 fits, with the grey shaded area representing the 1σ uncertainty. Three models (the models from Merten, Williams, and Zitrin-NFW) are consistent with the magnification derived from the light-curve fit at the 1σ level. However, the lensing models are systematically high compared to the light-curve fits.

There are two explanations for this discrepancy. It may be that the SN Ia derived magnification is correct, and only three of the eight models match the magnification at the 1σ level. We stress that this is not an indictment on the other five models as a whole; it would simply mean that at this particular position (and redshift), the models do not predict the correct magnification. As mentioned in §1.1.5, the purpose of searching for lensed SNe Ia is to improve the gravitational lensing models.

Alternatively, the light-curve derived magnification could be incorrect. If the distances derived from the SALT2 and MLCS2k2 light-curve fits of SN HFF14tom were off by $\sim$0.5 mag, the discrepancy shown in Figure 5.5 would disappear. In that case, the light-curve derived magnification would be consistent with all eight lensing models at the 1σ level. As mentioned in Chapter 4, there are some systematics associated with SNe Ia which could lead to incorrect distance estimates. An improved light-curve fitter, like MLCS3, that properly accounted for the various systematics could resolve the discrepancy one way or another.

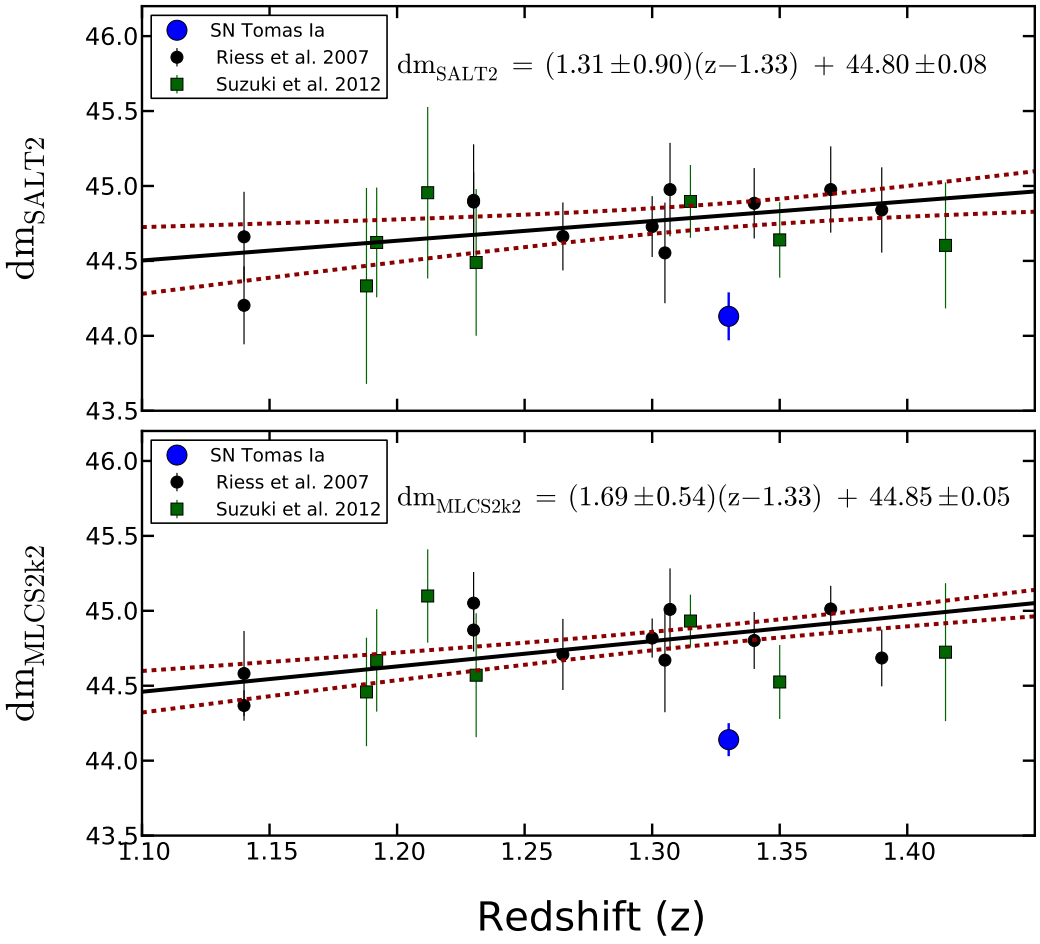

Figure 5.4 Hubble diagrams for SN HFF14tom. The top panel shows SN Ia distances fit with SALT2 and the bottom panel has MLCS2k2 fits. The plots contain 18 field SNe Ia from Riess et al. (2007, in black) and Suzuki et al. (2012, in green) as a comparison sample. Both light-curve fitters show that the SN (the large blue point) was significantly brighter than typical SNe Ia at similar redshifts. The solid black lines with the displayed equations give the best-fit linear model to the comparison sample, with the red dashed lines representing the 1σ uncertainties. From the data, we predict a typical unlensed SN Ia at z=1.33 would have $\mathrm{dm_{MLCS2k2}} = 44.85 \pm 0.05$ and $\mathrm{dm_{SALT2}} = 44.80 \pm 0.08$. Compared to the inferred distance modulus for SN HFF14tom, we find that it was magnified by $\Delta m_{\mu,\mathrm{MLCS2k2}} = 0.71 \pm 0.12$ mag (corresponding to $\mu = 1.92 \pm 0.21$) and $\Delta m_{\mu,\mathrm{SALT2}} = 0.67 \pm 0.21$ mag (corresponding to $\mu = 1.85 \pm 0.34$). The magnifications are remarkably consistent for the two fitters, and show a significant magnification.

That is, if the new light-curve fitter produced similar results to MLCS2k2 and SALT2 for SN HFF14tom, we would have more certainty that the lensing models needed to be adjusted.

SN Refsdal

A second SN was recently found behind the MACS J1149.6+2223 cluster (Kelly et al. 2014b). This SN, nicknamed SN Refsdal, is the first multiply imaged SN discovered behind a galaxy cluster (see Figure 5.6). This represents an exciting discovery that will allow us to test gravational lensing models, and may provide an estimate of H_0 from the time-delays of images (Refsdal 1964; Massey et al. 2010).

5.3 Future SN Ia Surveys

We hope for more exciting SNe Ia discoveries in the near future from HFF and other surveys. HFF, along with another *HST* program *See Change* (PI:Perlmutter), should significantly expand our sample of lensed SNe Ia. In 3 years, we hope that the *James Webb Space Telescope* (JWST) successfully launches into space. JWST should significantly expand our sample of high redshift SNe Ia, and help us test standard ΛCDM cosmology.

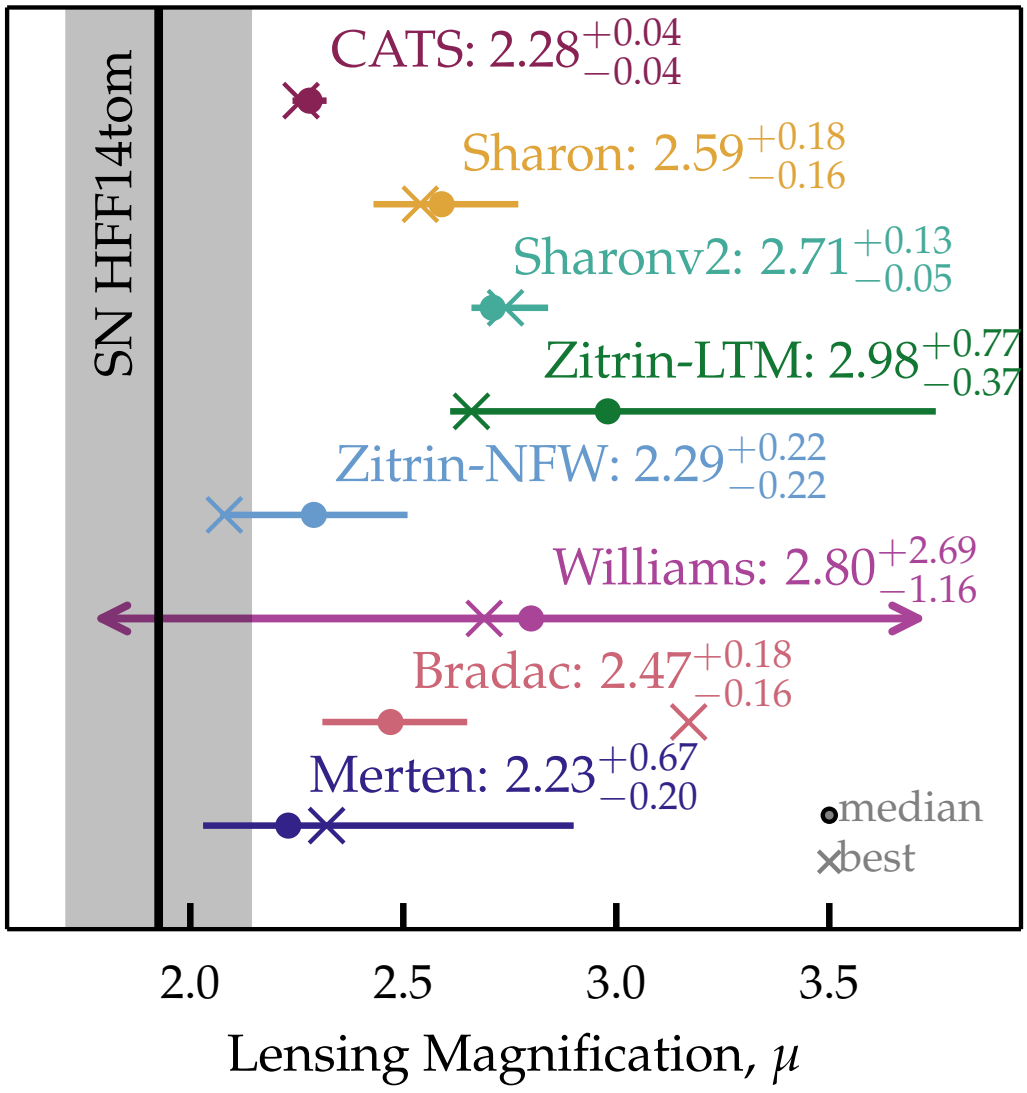

Figure 5.5 Comparison of lensing predictions from various lensing models and the prediction from the SN Ia analysis. The models are from Jauzac et al. (2014, CATS), Bradač et al. (2009, Bradac), Merten et al. (2011, Merten), Zitrin et al. (2013a, Zitrin-NFW), Zitrin et al. (2009, Zitrin-LTM), Grillo et al. (2014, Williams), Jullo et al. (2007, Sharon), Johnson et al. (2014, Sharonv2). Each of the horizontal lines represents the 1σ uncertainty range on the magnification prediction from one of the models. The dots represent the median value of the magnification prediction for each model. The positions of the 'x's represent the magnification that is most favored by each model. The black line indicates the magnification results from the MLCS2k2 fits, with the grey shaded area representing the 1σ uncertainty. Three lensing models (by Merten, Zitrin-NFW, and Williams) are consistent with the magnification derived from the light-curve fit.

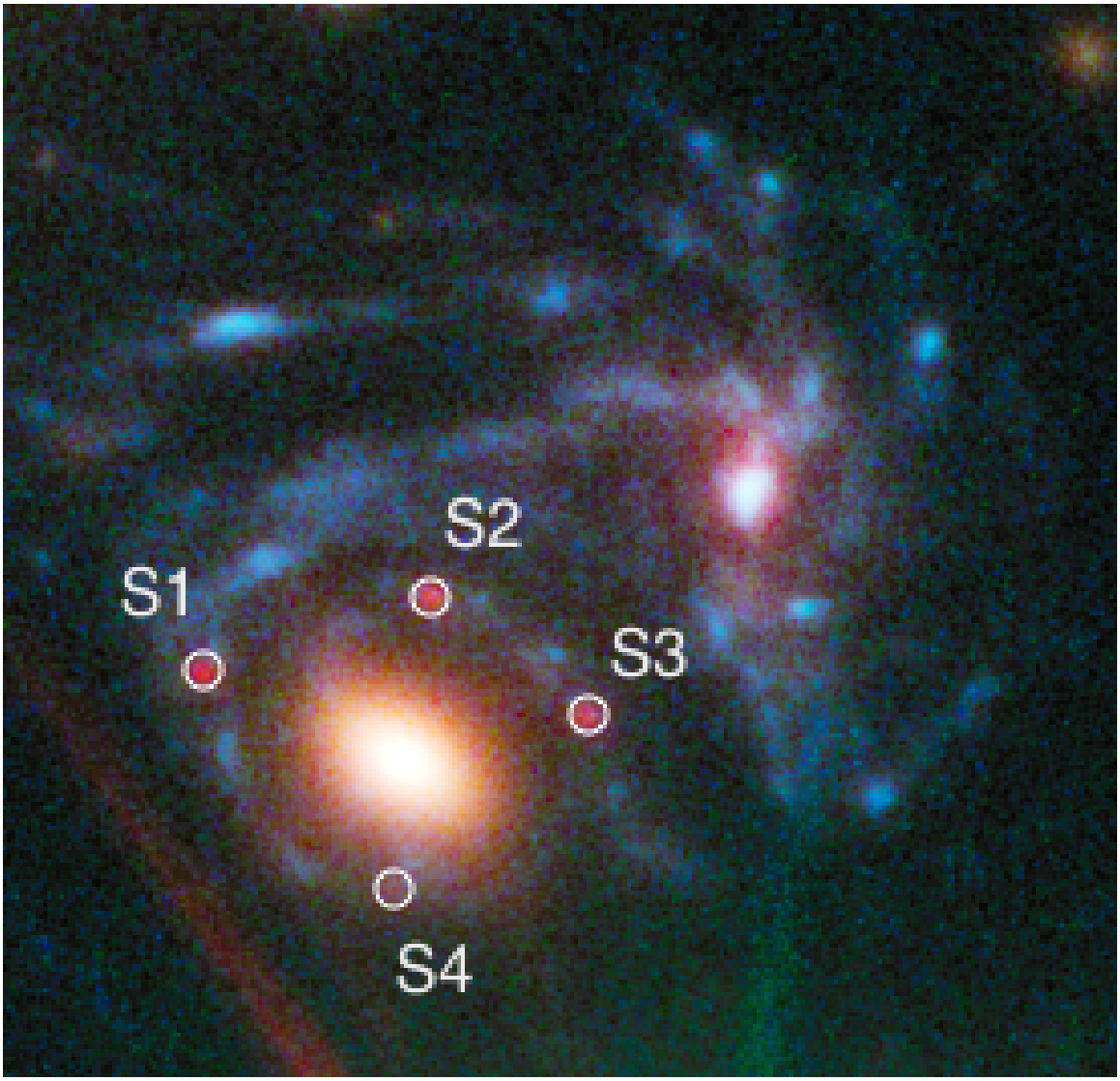

Figure 5.6 Color image showing the location of the multiply imaged SN Refsdal. Four images of the SN have been found, marked S1 through S4 in white circles.

Bibliography

Abazajian, K. N., Adelman-McCarthy, J. K., Agüeros, M. A., Allam, S. S., Allende Prieto, C., An, D., Anderson, K. S. J., Anderson, S. F., Annis, J., Bahcall, N. A., & et al. 2009, ApJS, 182, 543

Abell, G. O., Corwin, Jr., H. G., & Olowin, R. P. 1989, ApJS, 70, 1

Amanullah, R., Goobar, A., Clément, B., Cuby, J.-G., Dahle, H., Dahlén, T., Hjorth, J., Fabbro, S., Jönsson, J., Kneib, J.-P., Lidman, C., Limousin, M., Milvang-Jensen, B., Mörtsell, E., Nordin, J., Paech, K., Richard, J., Riehm, T., Stanishev, V., & Watson, D. 2011, ApJ, 742, L7

Amanullah, R., Goobar, A., Johansson, J., Banerjee, D. P. K., Venkataraman, V., Joshi, V., Ashok, N. M., Cao, Y., Kasliwal, M. M., Kulkarni, S. R., Nugent, P. E., Petrushevska, T., & Stanishev, V. 2014, ApJ, 788, L21

Arnaud, K. A. 1996, in Astronomical Society of the Pacific Conference Series, Vol. 101, Astronomical Data Analysis Software and Systems V, ed. G. H. Jacoby & J. Barnes, 17

Arnett, D. 1996, Supernovae and Nucleosynthesis

Balestra, I., Vanzella, E., Rosati, P., Monna, A., Grillo, C., Nonino, M., Mercurio, A., Biviano, A., Bradley, L., Coe, D., Fritz, A., Postman, M., Seitz, S., Scodeggio, M., Tozzi, P., Zheng, W., Ziegler, B., Zitrin, A., Annunziatella, M., Bartelmann, M., Benitez, N., Broadhurst, T., Bouwens, R., Czoske, O., Donahue, M., Ford, H., Girardi, M., Infante, L., Jouvel, S., Kelson, D., Koekemoer, A., Kuchner, U., Lemze, D., Lombardi, M., Maier, C., Medezinski, E., Melchior, P., Meneghetti, M., Merten, J., Molino, A., Moustakas, L., Presotto, V., Smit, R., & Umetsu, K. 2013, A&A, 559, L9

Bartelmann, M. 2010, Classical and Quantum Gravity, 27, 233001

Bazin, G., Palanque-Delabrouille, N., Rich, J., Ruhlmann-Kleider, V., Aubourg, E., Le Guillou, L., Astier, P., Balland, C., Basa, S., Carlberg, R. G., Conley, A., Fouchez, D., Guy, J., Hardin, D., Hook, I. M., Howell, D. A., Pain, R., Perrett, K., Pritchet, C. J., Regnault, N., Sullivan, M., Antilogus, P., Arsenijevic, V., Baumont, S., Fabbro, S., Le Du, J., Lidman, C., Mouchet, M., Mourão, A., & Walker, E. S. 2009, A&A, 499, 653

Benítez, N., Riess, A., Nugent, P., Dickinson, M., Chornock, R., & Filippenko, A. V. 2002, ApJ, 577, L1

Bernstein, J. P., Kessler, R., Kuhlmann, S., Biswas, R., Kovacs, E., Aldering, G., Crane, I., D'Andrea, C. B., Finley, D. A., Frieman, J. A., Hufford, T., Jarvis, M. J., Kim, A. G., Marriner, J., Mukherjee, P., Nichol, R. C., Nugent, P., Parkinson, D., Reis, R. R. R., Sako, M., Spinka, H., & Sullivan, M. 2012, ApJ, 753, 152

Betoule, M., Kessler, R., Guy, J., Mosher, J., Hardin, D., Biswas, R., Astier, P., El-Hage, P., Konig, M., Kuhlmann, S., Marriner, J., Pain, R., Regnault, N., Balland, C., Bassett, B. A., Brown, P. J., Campbell, H., Carlberg, R. G., Cellier-Holzem, F., Cinabro, D., Conley, A., D'Andrea, C. B., DePoy, D. L., Doi, M., Ellis, R. S., Fabbro, S., Filippenko, A. V., Foley, R. J., Frieman, J. A., Fouchez, D., Galbany, L., Goobar, A., Gupta, R. R., Hill, G. J., Hlozek, R., Hogan, C. J., Hook, I. M., Howell, D. A., Jha, S. W., Le Guillou, L., Leloudas, G., Lidman, C., Marshall, J. L., Möller, A., Mourão, A. M., Neveu, J., Nichol, R., Olmstead, M. D., Palanque-Delabrouille, N., Perlmutter, S., Prieto, J. L., Pritchet, C. J., Richmond, M., Riess, A. G., Ruhlmann-Kleider, V., Sako, M., Schahmaneche, K., Schneider, D. P., Smith, M., Sollerman, J., Sullivan, M., Walton, N. A., & Wheeler, C. J. 2014, A&A, 568, A22

Blondin, S., Matheson, T., Kirshner, R. P., Mandel, K. S., Berlind, P., Calkins, M., Challis, P., Garnavich, P. M., Jha, S. W., Modjaz, M., Riess, A. G., & Schmidt, B. P. 2012, AJ, 143, 126

Bloom, J. S., Kasen, D., Shen, K. J., Nugent, P. E., Butler, N. R., Graham, M. L., Howell, D. A., Kolb, U., Holmes, S., Haswell, C. A., Burwitz, V., Rodriguez, J., & Sullivan, M. 2012, ApJ, 744, L17

Botticella, M. T., Smartt, S. J., Kennicutt, R. C., Cappellaro, E., Sereno, M., & Lee, J. C. 2012, A&A, 537, A132

Bradač, M., Treu, T., Applegate, D., Gonzalez, A. H., Clowe, D., Forman, W., Jones, C., Marshall, P., Schneider, P., & Zaritsky, D. 2009, ApJ, 706, 1201

Brown, P. J., Roming, P. W. A., Milne, P., Bufano, F., Ciardullo, R., Elias-Rosa, N., Filippenko, A. V., Foley, R. J., Gehrels, N., Gronwall, C., Hicken, M., Holland, S. T., Hoversten, E. A., Immler, S., Kirshner, R. P., Li, W., Mazzali, P., Phillips, M. M., Pritchard, T., Still, M., Turatto, M., & Vanden Berk, D. 2010, ApJ, 721, 1608

Burns, C. R., Stritzinger, M., Phillips, M. M., Hsiao, E. Y., Contreras, C., Persson, S. E., Folatelli, G., Boldt, L., Campillay, A., Castellón, S., Freedman, W. L., Madore, B. F., Morrell, N., Salgado, F., & Suntzeff, N. B. 2014, ApJ, 789, 32

Burns, C. R., Stritzinger, M., Phillips, M. M., Kattner, S., Persson, S. E., Madore, B. F., Freedman, W. L., Boldt, L., Campillay, A., Contreras, C., Folatelli, G., Gonzalez, S., Krzeminski, W., Morrell, N., Salgado, F., & Suntzeff, N. B. 2011, AJ, 141, 19

Cappellaro, E., Evans, R., & Turatto, M. 1999, A&A, 351, 459

Carroll, B. W., & Ostlie, D. A. 2006, An introduction to modern astrophysics and cosmology

Carroll, S. M. 2004, Spacetime and geometry. An introduction to general relativity

Cash, W. 1979, ApJ, 228, 939

Childress, M. J., Wolf, C., & Zahid, H. J. 2014, MNRAS, 445, 1898

Chornock, R., Berger, E., Rest, A., Milisavljevic, D., Lunnan, R., Foley, R. J., Soderberg, A. M., Smartt, S. J., Burgasser, A. J., Challis, P., Chomiuk, L., Czekala, I., Drout, M., Fong, W., Huber, M. E., Kirshner, R. P., Leibler, C., McLeod, B., Marion, G. H.,

Narayan, G., Riess, A. G., Roth, K. C., Sanders, N. E., Scolnic, D., Smith, K., Stubbs, C. W., Tonry, J. L., Valenti, S., Burgett, W. S., Chambers, K. C., Hodapp, K. W., Kaiser, N., Kudritzki, R.-P., Magnier, E. A., & Price, P. A. 2013, ApJ, 767, 162

Conley, A., Guy, J., Sullivan, M., Regnault, N., Astier, P., Balland, C., Basa, S., Carlberg, R. G., Fouchez, D., Hardin, D., Hook, I. M., Howell, D. A., Pain, R., Palanque-Delabrouille, N., Perrett, K. M., Pritchet, C. J., Rich, J., Ruhlmann-Kleider, V., Balam, D., Baumont, S., Ellis, R. S., Fabbro, S., Fakhouri, H. K., Fourmanoit, N., González-Gaitán, S., Graham, M. L., Hudson, M. J., Hsiao, E., Kronborg, T., Lidman, C., Mourao, A. M., Neill, J. D., Perlmutter, S., Ripoche, P., Suzuki, N., & Walker, E. S. 2011, ApJS, 192, 1

Conley, A., Sullivan, M., Hsiao, E. Y., Guy, J., Astier, P., Balam, D., Balland, C., Basa, S., Carlberg, R. G., Fouchez, D., Hardin, D., Howell, D. A., Hook, I. M., Pain, R., Perrett, K., Pritchet, C. J., & Regnault, N. 2008, ApJ, 681, 482

Cooke, J., Sullivan, M., Gal-Yam, A., Barton, E. J., Carlberg, R. G., Ryan-Weber, E. V., Horst, C., Omori, Y., & Díaz, C. G. 2012, Nature, 491, 228

Cowley, A. P., Schmidtke, P. C., Crampton, D., & Hutchings, J. B. 1990, ApJ, 350, 288

Crawford, S. M., Still, M., Schellart, P., Balona, L., Buckley, D. A. H., Dugmore, G., Gulbis, A. A. S., Kniazev, A., Kotze, M., Loaring, N., Nordsieck, K. H., Pickering, T. E., Potter, S., Romero Colmenero, E., Vaisanen, P., Williams, T., & Zietsman, E. 2010, in Society of Photo-Optical Instrumentation Engineers (SPIE) Conference Series, Vol. 7737, Society of Photo-Optical Instrumentation Engineers (SPIE) Conference Series

Dahlen, T., Strolger, L.-G., Riess, A. G., Mobasher, B., Chary, R.-R., Conselice, C. J., Ferguson, H. C., Fruchter, A. S., Giavalisco, M., Livio, M., Madau, P., Panagia, N., & Tonry, J. L. 2004, ApJ, 613, 189

Daniel, S. F., & Linder, E. V. 2010, Phys. Rev. D, 82, 103523

Di Stefano, R. 2010a, ApJ, 712, 728

—. 2010b, ApJ, 719, 474

Di Stefano, R., Friedman, R., Kundu, A., & Kong, A. K. H. 2003a, ArXiv Astrophysics e-prints

Di Stefano, R., Kong, A., & Primini, F. A. 2006, ArXiv Astrophysics e-prints

—. 2010a, NewAR, 54, 72

Di Stefano, R., & Kong, A. K. H. 2003, ArXiv Astrophysics e-prints

—. 2004, ApJ, 609, 710

Di Stefano, R., Kong, A. K. H., Greiner, J., Primini, F. A., Garcia, M. R., Barmby, P., Massey, P., Hodge, P. W., Williams, B. F., Murray, S. S., Curry, S., & Russo, T. A. 2004a, ApJ, 610, 247

Di Stefano, R., Kong, A. K. H., VanDalfsen, M. L., Harris, W. E., Murray, S. S., & Delain, K. M. 2003b, ApJ, 599, 1067

Di Stefano, R., & Nelson, L. A. 1996, in Lecture Notes in Physics, Berlin Springer Verlag, Vol. 472, Supersoft X-Ray Sources, ed. J. Greiner, 3

Di Stefano, R., Primini, F. A., Kong, A. K. H., & Russo, T. 2004b, ArXiv Astrophysics e-prints

Di Stefano, R., Primini, F. A., Liu, J., Kong, A., & Patel, B. 2010b, Astronomische Nachrichten, 331, 205

Di Stefano, R., Voss, R., & Claeys, J. S. W. 2011, ApJ, 738, L1

Dilday, B., Bassett, B., Becker, A., Bender, R., Castander, F., Cinabro, D., Frieman, J. A., Galbany, L., Garnavich, P., Goobar, A., Hopp, U., Ihara, Y., Jha, S. W., Kessler, R., Lampeitl, H., Marriner, J., Miquel, R., Mollá, M., Nichol, R. C., Nordin, J., Riess, A. G., Sako, M., Schneider, D. P., Smith, M., Sollerman, J., Wheeler, J. C., Östman, L., Bizyaev, D., Brewington, H., Malanushenko, E., Malanushenko, V., Oravetz, D., Pan, K., Simmons, A., & Snedden, S. 2010, ApJ, 715, 1021

Dilday, B., Howell, D. A., Cenko, S. B., Silverman, J. M., Nugent, P. E., Sullivan, M., Ben-Ami, S., Bildsten, L., Bolte, M., Endl, M., Filippenko, A. V., Gnat, O., Horesh, A., Hsiao, E., Kasliwal, M. M., Kirkman, D., Maguire, K., Marcy, G. W., Moore, K., Pan, Y., Parrent, J. T., Podsiadlowski, P., Quimby, R. M., Sternberg, A., Suzuki, N., Tytler, D. R., Xu, D., Bloom, J. S., Gal-Yam, A., Hook, I. M., Kulkarni, S. R., Law, N. M., Ofek, E. O., Polishook, D., & Poznanski, D. 2012, Science, 337, 942

Dolphin, A. E. 2000, PASP, 112, 1383

Dressel, L. 2012, Wide Field Camera 3 Instrument Handbook for Cycle 21 v. 5.0

Drout, M. R., Soderberg, A. M., Gal-Yam, A., Cenko, S. B., Fox, D. B., Leonard, D. C., Sand, D. J., Moon, D.-S., Arcavi, I., & Green, Y. 2011, ApJ, 741, 97

Ebeling, H., Edge, A. C., Bohringer, H., Allen, S. W., Crawford, C. S., Fabian, A. C., Voges, W., & Huchra, J. P. 1998, MNRAS, 301, 881

Ebeling, H., Edge, A. C., Mantz, A., Barrett, E., Henry, J. P., Ma, C. J., & van Speybroeck, L. 2010, MNRAS, 407, 83

Faber, S. M., Phillips, A. C., Kibrick, R. I., Alcott, B., Allen, S. L., Burrous, J., Cantrall, T., Clarke, D., Coil, A. L., Cowley, D. J., Davis, M., Deich, W. T. S., Dietsch, K., Gilmore, D. K., Harper, C. A., Hilyard, D. F., Lewis, J. P., McVeigh, M., Newman, J., Osborne, J., Schiavon, R., Stover, R. J., Tucker, D., Wallace, V., Wei, M., Wirth, G., & Wright, C. A. 2003, in Society of Photo-Optical Instrumentation Engineers (SPIE) Conference Series, Vol. 4841, Instrument Design and Performance for Optical/Infrared Ground-based Telescopes, ed. M. Iye & A. F. M. Moorwood, 1657–1669

Falco, E. E., Gorenstein, M. V., & Shapiro, I. I. 1985, ApJ, 289, L1

Filippenko, A. V. 1997, ARA&A, 35, 309

Foley, R., Kirshner, R., Challis, P., Rest, A., Chornock, R., Riess, A., Scolnic, D., & Stubbs, C. 2013, RAISIN: Tracers of Cosmic Expansion with SN Ia in the IR, NOAO Proposal

Foley, R. J., Filippenko, A. V., Kessler, R., Bassett, B., Frieman, J. A., Garnavich, P. M., Jha, S. W., Konishi, K., Lampeitl, H., Riess, A. G., Sako, M., Schneider, D. P., Sollerman, J., & Smith, M. 2012, AJ, 143, 113

Foley, R. J., & Mandel, K. 2013, ApJ, 778, 167

Foley, R. J., Sanders, N. E., & Kirshner, R. P. 2011, ApJ, 742, 89

Freeman, P. E., Kashyap, V., Rosner, R., & Lamb, D. Q. 2002, ApJS, 138, 185

Friedman, A. S., Wood-Vasey, W. M., Marion, G. H., Challis, P., Mandel, K. S., Bloom, J. S., Modjaz, M., Narayan, G., Hicken, M., Foley, R., Klein, C. R., Starr, D. L., Morgan, A., Rest, A., Blake, C. H., Miller, A. A., Falco, E. E., Wyatt, W. F., Mink, J., Skrutskie, M. F., & Kirshner, R. P. 2014, ArXiv e-prints

Frieman, J., & Dark Energy Survey Collaboration. 2013, in American Astronomical Society Meeting Abstracts, Vol. 221, American Astronomical Society Meeting Abstracts, #335.01

Fruchter, A., & et al. 2009, HST MultiDrizzle Handbook

Fruscione, A., McDowell, J. C., Allen, G. E., Brickhouse, N. S., Burke, D. J., Davis, J. E., Durham, N., Elvis, M., Galle, E. C., Harris, D. E., Huenemoerder, D. P., Houck, J. C., Ishibashi, B., Karovska, M., Nicastro, F., Noble, M. S., Nowak, M. A., Primini, F. A., Siemiginowska, A., Smith, R. K., & Wise, M. 2006, in Society of Photo-Optical Instrumentation Engineers (SPIE) Conference Series, Vol. 6270, Society of Photo-Optical Instrumentation Engineers (SPIE) Conference Series, 1

Fujimoto, M. Y. 1982, ApJ, 257, 767

Gilfanov, M., & Bogdán, Á. 2010, Nature, 463, 924

Gilliland, R. L., Nugent, P. E., & Phillips, M. M. 1999, ApJ, 521, 30

Goobar, A., Johansson, J., Amanullah, R., Cao, Y., Perley, D. A., Kasliwal, M. M., Ferretti, R., Nugent, P. E., Harris, C., Gal-Yam, A., Ofek, E. O., Tendulkar, S. P., Dennefeld, M., Valenti, S., Arcavi, I., Banerjee, D. P. K., Venkataraman, V., Joshi, V., Ashok, N. M., Cenko, S. B., Diaz, R. F., Fremling, C., Horesh, A., Howell, D. A., Kulkarni, S. R., Papadogiannakis, S., Petrushevska, T., Sand, D., Sollerman, J., Stanishev, V., Bloom, J. S., Surace, J., Dupuy, T. J., & Liu, M. C. 2014, ApJ, 784, L12

Goobar, A., Mörtsell, E., Amanullah, R., & Nugent, P. 2002, A&A, 393, 25

Goobar, A., Paech, K., Stanishev, V., Amanullah, R., Dahlén, T., Jönsson, J., Kneib, J. P., Lidman, C., Limousin, M., Mörtsell, E., Nobili, S., Richard, J., Riehm, T., & von Strauss, M. 2009, A&A, 507, 71

Graham, M. L., Pritchet, C. J., Sullivan, M., Gwyn, S. D. J., Neill, J. D., Hsiao, E. Y., Astier, P., Balam, D., Balland, C., Basa, S., Carlberg, R. G., Conley, A., Fouchez, D., Guy, J., Hardin, D., Hook, I. M., Howell, D. A., Pain, R., Perrett, K., Regnault, N., Baumont, S., LeDu, J., Lidman, C., Perlmutter, S., Ripoche, P., Suzuki, N., Walker, E. S., & Zhang, T. 2008, AJ, 135, 1343

Graham, M. L., Sand, D. J., Pritchet, C. J., Richard, J., Zaritsky, D., Hoekstra, H., Bildfell, C. J., Gladders, M., Ebeling, H., Kneib, J. P., Kezwer, J., Fabbro, S., Gavazzi, R., Limousin, M., Jullo, E., & Parrent, J. 2013, The Astronomer's Telegram, 5017, 1

Graur, O., Rodney, S. A., Maoz, D., Riess, A. G., Jha, S. W., Postman, M., Dahlen, T., Holoien, T. W.-S., McCully, C., Patel, B., Strolger, L.-G., Benítez, N., Coe, D., Jouvel, S., Medezinski, E., Molino, A., Nonino, M., Bradley, L., Koekemoer, A., Balestra, I., Cenko, S. B., Clubb, K. I., Dickinson, M. E., Filippenko, A. V., Frederiksen, T. F., Garnavich, P., Hjorth, J., Jones, D. O., Leibundgut, B., Matheson, T., Mobasher, B., Rosati, P., Silverman, J. M., U, V., Jedruszczuk, K., Li, C., Lin, K., Mirmelstein, M., Neustadt, J., Ovadia, A., & Rogers, E. H. 2014, ApJ, 783, 28

Greiner, J. 2000, ArXiv Astrophysics e-prints, 5, 137

Greiner, J., Di Stefano, R., Kong, A., & Primini, F. 2004, ApJ, 610, 261

Grillo, C., Suyu, S. H., Rosati, P., Mercurio, A., Balestra, I., Munari, E., Nonino, M., Caminha, G. B., Lombardi, M., De Lucia, G., Borgani, S., Gobat, R., Biviano, A., Girardi, M., Umetsu, K., Coe, D., Koekemoer, A. M., Postman, M., Zitrin, A., Halkola, A., Broadhurst, T., Sartoris, B., Presotto, V., Annunziatella, M., Maier, C., Fritz, A., Vanzella, E., & Frye, B. 2014, ArXiv e-prints

Grupe, D., Komossa, S., Leighly, K. M., & Page, K. L. 2010, ApJS, 187, 64

Guy, J., Astier, P., Baumont, S., Hardin, D., Pain, R., Regnault, N., Basa, S., Carlberg, R. G., Conley, A., Fabbro, S., Fouchez, D., Hook, I. M., Howell, D. A., Perrett, K., Pritchet, C. J., Rich, J., Sullivan, M., Antilogus, P., Aubourg, E., Bazin, G., Bronder, J., Filiol, M., Palanque-Delabrouille, N., Ripoche, P., & Ruhlmann-Kleider, V. 2007, A&A, 466, 11

Guy, J., Sullivan, M., Conley, A., Regnault, N., Astier, P., Balland, C., Basa, S., Carlberg, R. G., Fouchez, D., Hardin, D., Hook, I. M., Howell, D. A., Pain, R., Palanque-Delabrouille, N., Perrett, K. M., Pritchet, C. J., Rich, J., Ruhlmann-Kleider, V., Balam, D., Baumont, S., Ellis, R. S., Fabbro, S., Fakhouri, H. K., Fourmanoit, N., González-Gaitán, S., Graham, M. L., Hsiao, E., Kronborg, T., Lidman, C., Mourao, A. M., Perlmutter, S., Ripoche, P., Suzuki, N., & Walker, E. S. 2010, A&A, 523, A7

Haberl, F. 2007, Ap&SS, 308, 181

Hachisu, I., Kato, M., & Nomoto, K. 1996, ApJ, 470, L97

Hicken, M., Challis, P., Kirshner, R. P., Rest, A., Cramer, C. E., Wood-Vasey, W. M., Bakos, G., Berlind, P., Brown, W. R., Caldwell, N., Calkins, M., Currie, T., de Kleer, K., Esquerdo, G., Everett, M., Falco, E., Fernandez, J., Friedman, A. S., Groner, T., Hartman, J., Holman, M. J., Hutchins, R., Keys, S., Kipping, D., Latham, D., Marion, G. H., Narayan, G., Pahre, M., Pal, A., Peters, W., Perumpilly, G., Ripman, B., Sipocz, B., Szentgyorgyi, A., Tang, S., Torres, M. A. P., Vaz, A., Wolk, S., & Zezas, A. 2012, ApJS, 200, 12

Hicken, M., Wood-Vasey, W. M., Blondin, S., Challis, P., Jha, S., Kelly, P. L., Rest, A., & Kirshner, R. P. 2009, ApJ, 700, 1097

Holland, S. 1998, AJ, 115, 1916

Holtzman, J. A., Marriner, J., Kessler, R., Sako, M., Dilday, B., Frieman, J. A., Schneider, D. P., Bassett, B., Becker, A., Cinabro, D., DeJongh, F., Depoy, D. L., Doi, M., Garnavich, P. M., Hogan, C. J., Jha, S., Konishi, K., Lampeitl, H., Marshall, J. L., McGinnis, D., Miknaitis, G., Nichol, R. C., Prieto, J. L., Riess, A. G., Richmond, M. W., Romani, R., Smith, M., Takanashi, N., Tokita, K., van der Heyden, K., Yasuda, N., & Zheng, C. 2008, AJ, 136, 2306

Holz, D. E. 2001, ApJ, 556, L71

Holz, D. E., & Linder, E. V. 2005, ApJ, 631, 678

Hook, I. M., Jørgensen, I., Allington-Smith, J. R., Davies, R. L., Metcalfe, N., Murowinski, R. G., & Crampton, D. 2004, PASP, 116, 425

Hsiao, E. Y., Conley, A., Howell, D. A., Sullivan, M., Pritchet, C. J., Carlberg, R. G., Nugent, P. E., & Phillips, M. M. 2007, ApJ, 663, 1187

Hughes, J. P. 1994, ApJ, 427, L25

Iben, Jr., I. 1982, ApJ, 259, 244

Iben, Jr., I., & Tutukov, A. V. 1984, ApJS, 54, 335

Jain, B., & Khoury, J. 2010, Annals of Physics, 325, 1479

Jauzac, M., Clément, B., Limousin, M., Richard, J., Jullo, E., Ebeling, H., Atek, H., Kneib, J.-P., Knowles, K., Natarajan, P., Eckert, D., Egami, E., Massey, R., & Rexroth, M. 2014, MNRAS, 443, 1549

Jha, S. 2002, PhD thesis, HARVARD UNIVERSITY

Jha, S., Riess, A. G., & Kirshner, R. P. 2007, ApJ, 659, 122

Johnson, T. L., Sharon, K., Bayliss, M. B., Gladders, M. D., Coe, D., & Ebeling, H. 2014, ApJ, 797, 48

Jones, D. O., Rodney, S. A., Riess, A. G., Mobasher, B., Dahlen, T., McCully, C., Frederiksen, T. F., Casertano, S., Hjorth, J., Keeton, C. R., Koekemoer, A., Strolger, L.-G., Wiklind, T. G., Challis, P., Graur, O., Hayden, B., Patel, B., Weiner, B. J., Filippenko, A. V., Garnavich, P., Jha, S. W., Kirshner, R. P., Ferguson, H. C., Grogin, N. A., & Kocevski, D. 2013, ApJ, 768, 166

Jönsson, J., Sullivan, M., Hook, I., Basa, S., Carlberg, R., Conley, A., Fouchez, D., Howell, D. A., Perrett, K., & Pritchet, C. 2010, MNRAS, 405, 535

Jouvel, S., Host, O., Lahav, O., Seitz, S., Molino, A., Coe, D., Postman, M., Moustakas, L., Benìtez, N., Rosati, P., Balestra, I., Grillo, C., Bradley, L., Fritz, A., Kelson, D., Koekemoer, A. M., Lemze, D., Medezinski, E., Mercurio, A., Moustakas, J., Nonino, M., Scodeggio, M., Zheng, W., Zitrin, A., Bartelmann, M., Bouwens, R., Broadhurst, T., Donahue, M., Ford, H., Graves, G., Infante, L., Jimenez-Teja, Y., Lazkoz, R., Melchior, P., Meneghetti, M., Merten, J., Ogaz, S., & Umetsu, K. 2014, A&A, 562, A86

Jullo, E., Kneib, J.-P., Limousin, M., Elíasdóttir, Á., Marshall, P. J., & Verdugo, T. 2007, New Journal of Physics, 9, 447

Kaaret, P. 2002, ApJ, 578, 114

Karpenka, N. V., March, M. C., Feroz, F., & Hobson, M. P. 2013, MNRAS, 433, 2693

Kashyap, V., Primini, F. A., Glotfelty, K. J., Anderson, C. S., Bonaventura, N. R., Chen, J. C., Davis, J. E., Doe, S. M., Evans, I. N., Evans, J. D., Fabbiano, G., Galle, E., Gibbs, D. G., Grier, J. D., Hain, R., Hall, D. M., Harbo, P. N., He, X., Houck, J. C., Karovska, M., Lauer, J., McCollough, M. L., McDowell, J. C., Miller, J. B., Mitschang, A. W., Morgan, D. L., Nichols, J. S., Nowak, M. A., Plummer, D. A., Refsdal, B. L., Rots, A. H., Siemiginowska, A. L., Sundheim, B. A., Tibbetts, M. S., Van Stone, D. W., Winkelman, S. L., & Zografou, P. 2009, in Bulletin of the American Astronomical Society, Vol. 41, American Astronomical Society Meeting Abstracts #213, 472.09

Kelly, P. L., Filippenko, A. V., Modjaz, M., & Kocevski, D. 2014a, ApJ, 789, 23

Kelly, P. L., Rodney, S. A., Treu, T., Foley, R. J., Brammer, G., Schmidt, K. B., Zitrin, A., Sonnenfeld, A., Strolger, L.-G., Graur, O., Filippenko, A. V., Jha, S. W., Riess, A. G., Bradac, M., Weiner, B. J., Scolnic, D., Malkan, M. A., von der Linden, A., Trenti, M., Hjorth, J., Gavazzi, R., Fontana, A., Merten, J., McCully, C., Jones, T., Postman, M., Dressler, A., Patel, B., Cenko, S. B., Graham, M. L., & Tucker, B. E. 2014b, ArXiv e-prints

Kessler, R., Bassett, B., Belov, P., Bhatnagar, V., Campbell, H., Conley, A., Frieman, J. A., Glazov, A., González-Gaitán, S., Hlozek, R., Jha, S., Kuhlmann, S., Kunz, M., Lampeitl, H., Mahabal, A., Newling, J., Nichol, R. C., Parkinson, D., Philip, N. S., Poznanski, D., Richards, J. W., Rodney, S. A., Sako, M., Schneider, D. P., Smith, M., Stritzinger, M., & Varughese, M. 2010, PASP, 122, 1415

Kessler, R., Becker, A. C., Cinabro, D., Vanderplas, J., Frieman, J. A., Marriner, J., Davis, T. M., Dilday, B., Holtzman, J., Jha, S. W., Lampeitl, H., Sako, M., Smith, M., Zheng, C., Nichol, R. C., Bassett, B., Bender, R., Depoy, D. L., Doi, M., Elson, E., Filippenko, A. V., Foley, R. J., Garnavich, P. M., Hopp, U., Ihara, Y., Ketzeback, W., Kollatschny, W., Konishi, K., Marshall, J. L., McMillan, R. J., Miknaitis, G., Morokuma, T., Mörtsell, E., Pan, K., Prieto, J. L., Richmond, M. W., Riess, A. G., Romani, R., Schneider, D. P., Sollerman, J., Takanashi, N., Tokita, K., van der Heyden, K., Wheeler, J. C., Yasuda, N., & York, D. 2009a, ApJS, 185, 32

Kessler, R., Bernstein, J. P., Cinabro, D., Dilday, B., Frieman, J. A., Jha, S., Kuhlmann, S., Miknaitis, G., Sako, M., Taylor, M., & Vanderplas, J. 2009b, PASP, 121, 1028

Kiewe, M., Gal-Yam, A., Arcavi, I., Leonard, D. C., Emilio Enriquez, J., Cenko, S. B., Fox, D. B., Moon, D.-S., Sand, D. J., Soderberg, A. M., & CCCP, T. 2012, ApJ, 744, 10

Kilic, M., Thorstensen, J. R., Kowalski, P. M., & Andrews, J. 2012, MNRAS, 423, L132

Kneib, J.-P., Ellis, R. S., Santos, M. R., & Richard, J. 2004, ApJ, 607, 697

Kolatt, T. S., & Bartelmann, M. 1998, MNRAS, 296, 763

Kong, A. K. H., & Di Stefano, R. 2003, ApJ, 590, L13

—. 2005, ApJ, 632, L107

Kong, A. K. H., Di Stefano, R., & Yuan, F. 2004, ApJ, 617, L49

Kong, A. K. H., Garcia, M. R., Primini, F. A., Murray, S. S., Di Stefano, R., & McClintock, J. E. 2002, ApJ, 577, 738

Krisciunas, K., Bastola, D., Espinoza, J., Gonzalez, D., Gonzalez, L., Gonzalez, S., Hamuy, M., Hsiao, E. Y., Morrell, N., Phillips, M. M., & Suntzeff, N. B. 2013, AJ, 145, 11

Kronborg, T., Hardin, D., Guy, J., Astier, P., Balland, C., Basa, S., Carlberg, R. G., Conley, A., Fouchez, D., Hook, I. M., Howell, D. A., Jönsson, J., Pain, R., Pedersen, K., Perrett, K., Pritchet, C. J., Regnault, N., Rich, J., Sullivan, M., Palanque-Delabrouille, N., & Ruhlmann-Kleider, V. 2010, A&A, 514, A44

Kylafis, N. D., & Xilouris, E. M. 1993, A&A, 278, L43

Lampeitl, H., Nichol, R. C., Seo, H.-J., Giannantonio, T., Shapiro, C., Bassett, B., Percival, W. J., Davis, T. M., Dilday, B., Frieman, J., Garnavich, P., Sako, M., Smith, M., Sollerman, J., Becker, A. C., Cinabro, D., Filippenko, A. V., Foley, R. J., Hogan, C. J., Holtzman, J. A., Jha, S. W., Konishi, K., Marriner, J., Richmond, M. W., Riess, A. G., Schneider, D. P., Stritzinger, M., van der Heyden, K. J., Vanderplas, J. T., Wheeler, J. C., & Zheng, C. 2010, MNRAS, 401, 2331

Le Fèvre, O., Saisse, M., Mancini, D., Brau-Nogue, S., Caputi, O., Castinel, L., D'Odorico, S., Garilli, B., Kissler-Patig, M., Lucuix, C., Mancini, G., Pauget, A., Sciarretta, G., Scodeggio, M., Tresse, L., & Vettolani, G. 2003, in Society of Photo-Optical Instrumentation Engineers (SPIE) Conference Series, Vol. 4841, Instrument Design and Performance for Optical/Infrared Ground-based Telescopes, ed. M. Iye & A. F. M. Moorwood, 1670–1681

Lewin, W. H. G., van Paradijs, J., & Taam, R. E. 1993, SSRv, 62, 223

Li, W., Bloom, J. S., Podsiadlowski, P., Miller, A. A., Cenko, S. B., Jha, S. W., Sullivan, M., Howell, D. A., Nugent, P. E., Butler, N. R., Ofek, E. O., Kasliwal, M. M., Richards, J. W., Stockton, A., Shih, H.-Y., Bildsten, L., Shara, M. M., Bibby, J., Filippenko, A. V., Ganeshalingam, M., Silverman, J. M., Kulkarni, S. R., Law, N. M., Poznanski, D., Quimby, R. M., McCully, C., Patel, B., Maguire, K., & Shen, K. J. 2011a, Nature, 480, 348

Li, W., Leaman, J., Chornock, R., Filippenko, A. V., Poznanski, D., Ganeshalingam, M., Wang, X., Modjaz, M., Jha, S., Foley, R. J., & Smith, N. 2011b, MNRAS, 412, 1441

Liang, N., Li, Z., Wu, P., Cao, S., Liao, K., & Zhu, Z.-H. 2013, MNRAS, 436, 1017

Liu, J. 2011, ApJS, 192, 10

Liu, J., & Di Stefano, R. 2008, ApJ, 674, L73

Long, K. S., Helfand, D. J., & Grabelsky, D. A. 1981, ApJ, 248, 925

LSST Science Collaboration, Abell, P. A., Allison, J., Anderson, S. F., Andrew, J. R., Angel, J. R. P., Armus, L., Arnett, D., Asztalos, S. J., Axelrod, T. S., & et al. 2009, ArXiv e-prints

Maguire, K., Sullivan, M., Ellis, R. S., Nugent, P. E., Howell, D. A., Gal-Yam, A., Cooke, J., Mazzali, P., Pan, Y.-C., Dilday, B., Thomas, R. C., Arcavi, I., Ben-Ami, S., Bersier, D., Bianco, F. B., Fulton, B. J., Hook, I., Horesh, A., Hsiao, E., James, P. A., Podsiadlowski, P., Walker, E. S., Yaron, O., Kasliwal, M. M., Laher, R. R., Law, N. M., Ofek, E. O., Poznanski, D., & Surace, J. 2012, MNRAS, 426, 2359

Mandel, K. S., Foley, R. J., & Kirshner, R. P. 2014, ApJ, 797, 75

Mannucci, F. 2005, in Astronomical Society of the Pacific Conference Series, Vol. 342, 1604-2004: Supernovae as Cosmological Lighthouses, ed. M. Turatto, S. Benetti, L. Zampieri, & W. Shea, 140

Maoz, D., Mannucci, F., & Nelemans, G. 2014, ARA&A, 52, 107

Martel, H., & Premadi, P. 2008, ApJ, 673, 657

Massey, P., Olsen, K. A. G., Hodge, P. W., Strong, S. B., Jacoby, G. H., Schlingman, W., & Smith, R. C. 2006, AJ, 131, 2478

Massey, R., Kitching, T., & Richard, J. 2010, Reports on Progress in Physics, 73, 086901

Maybhate, A. 2010, ACS Instrument Handbook, Version 9.0 (Baltimore, MD: STScI)

Medezinski, E., Umetsu, K., Nonino, M., Merten, J., Zitrin, A., Broadhurst, T., Donahue, M., Sayers, J., Waizmann, J.-C., Koekemoer, A., Coe, D., Molino, A., Melchior, P., Mroczkowski, T., Czakon, N., Postman, M., Meneghetti, M., Lemze, D., Ford, H., Grillo, C., Kelson, D., Bradley, L., Moustakas, J., Bartelmann, M., Benítez, N., Biviano, A., Bouwens, R., Golwala, S., Graves, G., Infante, L., Jiménez-Teja, Y., Jouvel, S., Lahav, O., Moustakas, L., Ogaz, S., Rosati, P., Seitz, S., & Zheng, W. 2013, ApJ, 777, 43

Meneghetti, M., Rasia, E., Merten, J., Bellagamba, F., Ettori, S., Mazzotta, P., Dolag, K., & Marri, S. 2010, A&A, 514, A93

Merten, J., Cacciato, M., Meneghetti, M., Mignone, C., & Bartelmann, M. 2009, A&A, 500, 681

Merten, J., Coe, D., Dupke, R., Massey, R., Zitrin, A., Cypriano, E. S., Okabe, N., Frye, B., Braglia, F. G., Jiménez-Teja, Y., Benítez, N., Broadhurst, T., Rhodes, J., Meneghetti, M., Moustakas, L. A., Sodré, Jr., L., Krick, J., & Bregman, J. N. 2011, MNRAS, 417, 333

Minkowski, R. 1941, PASP, 53, 224

Morrison, R., & McCammon, D. 1983, ApJ, 270, 119

Mukai, K. 1993, Legacy, vol. 3, p.21-31, 3, 21

Mukai, K., Still, M., Corbet, R. H. D., Kuntz, K. D., & Barnard, R. 2005, ApJ, 634, 1085

Nielsen, M. T. B., Dominik, C., Nelemans, G., & Voss, R. 2013, A&A, 549, A32

Nomoto, K. 1982, ApJ, 253, 798

Nordsieck, K. 2012, in American Institute of Physics Conference Series, Vol. 1429, American Institute of Physics Conference Series, ed. J. L. Hoffman, J. Bjorkman, & B. Whitney, 248–251

Nugent, P. E., Sullivan, M., Cenko, S. B., Thomas, R. C., Kasen, D., Howell, D. A., Bersier, D., Bloom, J. S., Kulkarni, S. R., Kandrashoff, M. T., Filippenko, A. V., Silverman, J. M., Marcy, G. W., Howard, A. W., Isaacson, H. T., Maguire, K., Suzuki, N., Tarlton, J. E., Pan, Y.-C., Bildsten, L., Fulton, B. J., Parrent, J. T., Sand, D., Podsiadlowski, P., Bianco, F. B., Dilday, B., Graham, M. L., Lyman, J., James, P., Kasliwal, M. M., Law, N. M., Quimby, R. M., Hook, I. M., Walker, E. S., Mazzali, P., Pian, E., Ofek, E. O., Gal-Yam, A., & Poznanski, D. 2011, Nature, 480, 344

Oguri, M., & Kawano, Y. 2003, MNRAS, 338, L25

Oguri, M., & Marshall, P. J. 2010, MNRAS, 405, 2579

Oguri, M., Suto, Y., & Turner, E. L. 2003, ApJ, 583, 584

Orio, M., Nelson, T., Bianchini, A., Di Mille, F., & Harbeck, D. 2010, ApJ, 717, 739

Orio, M., Zezas, A., Munari, U., Siviero, A., & Tepedelenlioglu, E. 2007, ApJ, 661, 1105

Östman, L., Nordin, J., Goobar, A., Amanullah, R., Smith, M., Sollerman, J., Stanishev, V., Stritzinger, M. D., Bassett, B. A., Davis, T. M., Edmondson, E., Frieman, J. A., Garnavich, P. M., Lampeitl, H., Leloudas, G., Marriner, J., Nichol, R. C., Romer, K., Sako, M., Schneider, D. P., & Zheng, C. 2011, A&A, 526, A28

Ostriker, J. P., & Davidson, K. 1973, in IAU Symposium, Vol. 55, X- and Gamma-Ray Astronomy, ed. H. Bradt & R. Giacconi, 143

Patel, B., Di Stefano, R., Nelson, T., Primini, F. A., Liu, J., & Scoles, S. 2013, ApJ, 771, 6

Patel, B., McCully, C., Jha, S. W., Rodney, S. A., Jones, D. O., Graur, O., Merten, J., Zitrin, A., Riess, A. G., Matheson, T., Sako, M., Holoien, T. W.-S., Postman, M., Coe, D., Bartelmann, M., Balestra, I., Benítez, N., Bouwens, R., Bradley, L., Broadhurst, T., Cenko, S. B., Donahue, M., Filippenko, A. V., Ford, H., Garnavich, P., Grillo, C., Infante, L., Jouvel, S., Kelson, D., Koekemoer, A., Lahav, O., Lemze, D., Maoz, D., Medezinski, E., Melchior, P., Meneghetti, M., Molino, A., Moustakas, J., Moustakas, L. A., Nonino, M., Rosati, P., Seitz, S., Strolger, L. G., Umetsu, K., & Zheng, W. 2014, ApJ, 786, 9

Patterson, J., & Raymond, J. C. 1985, ApJ, 292, 550

Perlmutter, S., Aldering, G., Goldhaber, G., Knop, R. A., Nugent, P., Castro, P. G., Deustua, S., Fabbro, S., Goobar, A., Groom, D. E., Hook, I. M., Kim, A. G., Kim, M. Y., Lee, J. C., Nunes, N. J., Pain, R., Pennypacker, C. R., Quimby, R., Lidman, C., Ellis, R. S., Irwin, M., McMahon, R. G., Ruiz-Lapuente, P., Walton, N., Schaefer, B., Boyle, B. J., Filippenko, A. V., Matheson, T., Fruchter, A. S., Panagia, N., Newberg, H. J. M., Couch, W. J., & Supernova Cosmology Project. 1999, ApJ, 517, 565

Perlmutter, S., Gabi, S., Goldhaber, G., Goobar, A., Groom, D. E., Hook, I. M., Kim, A. G., Kim, M. Y., Lee, J. C., Pain, R., Pennypacker, C. R., Small, I. A., Ellis, R. S., McMahon, R. G., Boyle, B. J., Bunclark, P. S., Carter, D., Irwin, M. J., Glazebrook, K.,

Newberg, H. J. M., Filippenko, A. V., Matheson, T., Dopita, M., & Couch, W. J. 1997, ApJ, 483, 565

Phillips, M. M. 1993, ApJ, 413, L105

Phillips, M. M., Lira, P., Suntzeff, N. B., Schommer, R. A., Hamuy, M., & Maza, J. 1999, AJ, 118, 1766

Pietsch, W., Fliri, J., Freyberg, M. J., Greiner, J., Haberl, F., Riffeser, A., & Sala, G. 2005, A&A, 442, 879

Pietsch, W., Haberl, F., Sala, G., Stiele, H., Hornoch, K., Riffeser, A., Fliri, J., Bender, R., Bühler, S., Burwitz, V., Greiner, J., & Seitz, S. 2007, A&A, 465, 375

Pires, A. M., Motch, C., Turolla, R., Treves, A., & Popov, S. B. 2009, A&A, 498, 233

Planck Collaboration, Ade, P. A. R., Aghanim, N., Armitage-Caplan, C., Arnaud, M., Ashdown, M., Atrio-Barandela, F., Aumont, J., Baccigalupi, C., Banday, A. J., & et al. 2014, A&A, 571, A16

Pogge, R. W., Atwood, B., Brewer, D. F., Byard, P. L., Derwent, M. A., Gonzalez, R., Martini, P., Mason, J. A., O'Brien, T. P., Osmer, P. S., Pappalardo, D. P., Steinbrecher, D. P., Teiga, E. J., & Zhelem, R. 2010, in Society of Photo-Optical Instrumentation Engineers (SPIE) Conference Series, Vol. 7735, Society of Photo-Optical Instrumentation Engineers (SPIE) Conference Series

Popham, R., & Narayan, R. 1995, ApJ, 442, 337

Postman, M., Coe, D., Benítez, N., Bradley, L., Broadhurst, T., Donahue, M., Ford, H., Graur, O., Graves, G., Jouvel, S., Koekemoer, A., Lemze, D., Medezinski, E., Molino, A., Moustakas, L., Ogaz, S., Riess, A., Rodney, S., Rosati, P., Umetsu, K., Zheng, W., Zitrin, A., Bartelmann, M., Bouwens, R., Czakon, N., Golwala, S., Host, O., Infante, L., Jha, S., Jimenez-Teja, Y., Kelson, D., Lahav, O., Lazkoz, R., Maoz, D., McCully, C., Melchior, P., Meneghetti, M., Merten, J., Moustakas, J., Nonino, M., Patel, B., Regös, E., Sayers, J., Seitz, S., & Van der Wel, A. 2012, ApJS, 199, 25

Quimby, R. M., Werner, M. C., Oguri, M., More, S., More, A., Tanaka, M., Nomoto, K., Moriya, T. J., Folatelli, G., Maeda, K., & Bersten, M. 2013, ApJ, 768, L20

Rappaport, S., Di Stefano, R., & Smith, J. D. 1994, ApJ, 426, 692

Refsdal, S. 1964, MNRAS, 128, 307

Remillard, R. A., & McClintock, J. E. 2006, ARA&A, 44, 49

Rest, A., Scolnic, D., Foley, R. J., Huber, M. E., Chornock, R., Narayan, G., Tonry, J. L., Berger, E., Soderberg, A. M., Stubbs, C. W., Riess, A., Kirshner, R. P., Smartt, S. J., Schlafly, E., Rodney, S., Botticella, M. T., Brout, D., Challis, P., Czekala, I., Drout, M., Hudson, M. J., Kotak, R., Leibler, C., Lunnan, R., Marion, G. H., McCrum, M., Milisavljevic, D., Pastorello, A., Sanders, N. E., Smith, K., Stafford, E., Thilker, D., Valenti, S., Wood-Vasey, W. M., Zheng, Z., Burgett, W. S., Chambers, K. C., Denneau, L., Draper, P. W., Flewelling, H., Hodapp, K. W., Kaiser, N., Kudritzki, R.-P., Magnier, E. A., Metcalfe, N., Price, P. A., Sweeney, W., Wainscoat, R., & Waters, C. 2014, ApJ, 795, 44

Riehm, T., Mörtsell, E., Goobar, A., Amanullah, R., Dahlén, T., Jönsson, J., Limousin, M., Paech, K., & Richard, J. 2011, A&A, 536, A94

Riess, A. G., Filippenko, A. V., Challis, P., Clocchiatti, A., Diercks, A., Garnavich, P. M., Gilliland, R. L., Hogan, C. J., Jha, S., Kirshner, R. P., Leibundgut, B., Phillips, M. M., Reiss, D., Schmidt, B. P., Schommer, R. A., Smith, R. C., Spyromilio, J., Stubbs, C., Suntzeff, N. B., & Tonry, J. 1998, AJ, 116, 1009

Riess, A. G., Filippenko, A. V., Li, W., Treffers, R. R., Schmidt, B. P., Qiu, Y., Hu, J., Armstrong, M., Faranda, C., Thouvenot, E., & Buil, C. 1999, AJ, 118, 2675

Riess, A. G., Nugent, P. E., Gilliland, R. L., Schmidt, B. P., Tonry, J., Dickinson, M., Thompson, R. I., Budavári, T., Casertano, S., Evans, A. S., Filippenko, A. V., Livio, M., Sanders, D. B., Shapley, A. E., Spinrad, H., Steidel, C. C., Stern, D., Surace, J., & Veilleux, S. 2001, ApJ, 560, 49

Riess, A. G., Press, W. H., & Kirshner, R. P. 1996, ApJ, 473, 88

Riess, A. G., Strolger, L.-G., Casertano, S., Ferguson, H. C., Mobasher, B., Gold, B., Challis, P. J., Filippenko, A. V., Jha, S., Li, W., Tonry, J., Foley, R., Kirshner, R. P., Dickinson, M., MacDonald, E., Eisenstein, D., Livio, M., Younger, J., Xu, C., Dahlén, T., & Stern, D. 2007, ApJ, 659, 98

Rodney, S. A., Riess, A. G., Dahlen, T., Strolger, L.-G., Ferguson, H. C., Hjorth, J., Frederiksen, T. F., Weiner, B. J., Mobasher, B., Casertano, S., Jones, D. O., Challis, P., Faber, S. M., Filippenko, A. V., Garnavich, P., Graur, O., Grogin, N. A., Hayden, B., Jha, S. W., Kirshner, R. P., Kocevski, D., Koekemoer, A., McCully, C., Patel, B., Rajan, A., & Scarlata, C. 2012, ApJ, 746, 5

Rodney, S. A., Riess, A. G., Strolger, L.-G., Dahlen, T., Graur, O., Casertano, S., Dickinson, M. E., Ferguson, H. C., Garnavich, P., Hayden, B., Jha, S. W., Jones, D. O., Kirshner, R. P., Koekemoer, A. M., McCully, C., Mobasher, B., Patel, B., Weiner, B. J., Cenko, S. B., Clubb, K. I., Cooper, M., Filippenko, A. V., Frederiksen, T. F., Hjorth, J., Leibundgut, B., Matheson, T., Nayyeri, H., Penner, K., Trump, J., Silverman, J. M., U, V., Azalee Bostroem, K., Challis, P., Rajan, A., Wolff, S., Faber, S. M., Grogin, N. A., & Kocevski, D. 2014, AJ, 148, 13

Rubin, D., Knop, R. A., Rykoff, E., Aldering, G., Amanullah, R., Barbary, K., Burns, M. S., Conley, A., Connolly, N., Deustua, S., Fadeyev, V., Fakhouri, H. K., Fruchter, A. S., Gibbons, R. A., Goldhaber, G., Goobar, A., Hsiao, E. Y., Huang, X., Kowalski, M., Lidman, C., Meyers, J., Nordin, J., Perlmutter, S., Saunders, C., Spadafora, A. L., Stanishev, V., Suzuki, N., Wang, L., & Supernova Cosmology Project, T. 2013, ApJ, 763, 35

Sako, M., Bassett, B., Becker, A., Cinabro, D., DeJongh, F., Depoy, D. L., Dilday, B., Doi, M., Frieman, J. A., Garnavich, P. M., Hogan, C. J., Holtzman, J., Jha, S., Kessler, R., Konishi, K., Lampeitl, H., Marriner, J., Miknaitis, G., Nichol, R. C., Prieto, J. L., Riess, A. G., Richmond, M. W., Romani, R., Schneider, D. P., Smith, M., Subba Rao, M., Takanashi, N., Tokita, K., van der Heyden, K., Yasuda, N., Zheng, C., Barentine, J., Brewington, H., Choi, C., Dembicky, J., Harnavek, M., Ihara, Y., Im, M., Ketzeback, W., Kleinman, S. J., Krzesiński, J., Long, D. C., Malanushenko, E., Malanushenko, V.,

McMillan, R. J., Morokuma, T., Nitta, A., Pan, K., Saurage, G., & Snedden, S. A. 2008, AJ, 135, 348

Sako, M., Bassett, B., Becker, A. C., Brown, P. J., Campbell, H., Cane, R., Cinabro, D., D'Andrea, C. B., Dawson, K. S., DeJongh, F., Depoy, D. L., Dilday, B., Doi, M., Filippenko, A. V., Fischer, J. A., Foley, R. J., Frieman, J. A., Galbany, L., Garnavich, P. M., Goobar, A., Gupta, R. R., Hill, G. J., Hayden, B. T., Hlozek, R., Holtzman, J. A., Hopp, U., Jha, S. W., Kessler, R., Kollatschny, W., Leloudas, G., Marriner, J., Marshall, J. L., Miquel, R., Morokuma, T., Mosher, J., Nichol, R. C., Nordin, J., Olmstead, M. D., Ostman, L., Prieto, J. L., Richmond, M., Romani, R. W., Sollerman, J., Stritzinger, M., Schneider, D. P., Smith, M., Wheeler, J. C., Yasuda, N., & Zheng, C. 2014, ArXiv e-prints

Sako, M., Bassett, B., Connolly, B., Dilday, B., Cambell, H., Frieman, J. A., Gladney, L., Kessler, R., Lampeitl, H., Marriner, J., Miquel, R., Nichol, R. C., Schneider, D. P., Smith, M., & Sollerman, J. 2011, ApJ, 738, 162

Sala, G., & Hernanz, M. 2005, A&A, 439, 1061

Sala, G., Hernanz, M., Ferri, C., & Greiner, J. 2010, Astronomische Nachrichten, 331, 201

Salzano, V., Rodney, S. A., Sendra, I., Lazkoz, R., Riess, A. G., Postman, M., Broadhurst, T., & Coe, D. 2013, A&A, 557, A64

Schaefer, B. E., & Pagnotta, A. 2012, Nature, 481, 164

Schlegel, D. J., Finkbeiner, D. P., & Davis, M. 1998, ApJ, 500, 525

Schneider, P., & Sluse, D. 2013, A&A, 559, A37

Schwab, J., Bolton, A. S., & Rappaport, S. A. 2010, ApJ, 708, 750

Scolnic, D., Rest, A., Riess, A., Huber, M. E., Foley, R. J., Brout, D., Chornock, R., Narayan, G., Tonry, J. L., Berger, E., Soderberg, A. M., Stubbs, C. W., Kirshner, R. P., Rodney, S., Smartt, S. J., Schlafly, E., Botticella, M. T., Challis, P., Czekala, I., Drout, M., Hudson, M. J., Kotak, R., Leibler, C., Lunnan, R., Marion, G. H., McCrum, M., Milisavljevic, D., Pastorello, A., Sanders, N. E., Smith, K., Stafford, E., Thilker, D., Valenti, S., Wood-Vasey, W. M., Zheng, Z., Burgett, W. S., Chambers, K. C., Denneau, L., Draper, P. W., Flewelling, H., Hodapp, K. W., Kaiser, N., Kudritzki, R.-P., Magnier, E. A., Metcalfe, N., Price, P. A., Sweeney, W., Wainscoat, R., & Waters, C. 2014a, ApJ, 795, 45

Scolnic, D. M., Riess, A. G., Foley, R. J., Rest, A., Rodney, S. A., Brout, D. J., & Jones, D. O. 2014b, ApJ, 780, 37

Shen, K. J., & Bildsten, L. 2008, ApJ, 678, 1530

Smith, M., Bacon, D. J., Nichol, R. C., Campbell, H., Clarkson, C., Maartens, R., D'Andrea, C. B., Bassett, B. A., Cinabro, D., Finley, D. A., Frieman, J. A., Galbany, L., Garnavich, P. M., Olmstead, M. D., Schneider, D. P., Shapiro, C., & Sollerman, J. 2014, ApJ, 780, 24

Stanishev, V., Goobar, A., Paech, K., Amanullah, R., Dahlén, T., Jönsson, J., Kneib, J. P., Lidman, C., Limousin, M., Mörtsell, E., Nobili, S., Richard, J., Riehm, T., & von Strauss, M. 2009, A&A, 507, 61

Stetson, P. B., Davis, L. E., & Crabtree, D. R. 1990, in Astronomical Society of the Pacific Conference Series, Vol. 8, CCDs in astronomy, ed. G. H. Jacoby, 289–304

Stiele, H., Pietsch, W., Haberl, F., Burwitz, V., Hatzidimitriou, D., & Greiner, J. 2010, Astronomische Nachrichten, 331, 212

Stiele, H., Pietsch, W., Haberl, F., & Freyberg, M. 2008, A&A, 480, 599

Stritzinger, M. D., Phillips, M. M., Boldt, L. N., Burns, C., Campillay, A., Contreras, C., Gonzalez, S., Folatelli, G., Morrell, N., Krzeminski, W., Roth, M., Salgado, F., DePoy, D. L., Hamuy, M., Freedman, W. L., Madore, B. F., Marshall, J. L., Persson, S. E., Rheault, J.-P., Suntzeff, N. B., Villanueva, S., Li, W., & Filippenko, A. V. 2011, AJ, 142, 156

Sullivan, M., Conley, A., Howell, D. A., Neill, J. D., Astier, P., Balland, C., Basa, S., Carlberg, R. G., Fouchez, D., Guy, J., Hardin, D., Hook, I. M., Pain, R., Palanque-Delabrouille, N., Perrett, K. M., Pritchet, C. J., Regnault, N., Rich, J., Ruhlmann-Kleider, V., Baumont, S., Hsiao, E., Kronborg, T., Lidman, C., Perlmutter, S., & Walker, E. S. 2010, MNRAS, 406, 782

Sullivan, M., Ellis, R., Nugent, P., Smail, I., & Madau, P. 2000, MNRAS, 319, 549

Sullivan, M., Guy, J., Conley, A., Regnault, N., Astier, P., Balland, C., Basa, S., Carlberg, R. G., Fouchez, D., Hardin, D., Hook, I. M., Howell, D. A., Pain, R., Palanque-Delabrouille, N., Perrett, K. M., Pritchet, C. J., Rich, J., Ruhlmann-Kleider, V., Balam, D., Baumont, S., Ellis, R. S., Fabbro, S., Fakhouri, H. K., Fourmanoit, N., González-Gaitán, S., Graham, M. L., Hudson, M. J., Hsiao, E., Kronborg, T., Lidman, C., Mourao, A. M., Neill, J. D., Perlmutter, S., Ripoche, P., Suzuki, N., & Walker, E. S. 2011, ApJ, 737, 102

Suzuki, N., Rubin, D., Lidman, C., Aldering, G., Amanullah, R., Barbary, K., Barrientos, L. F., Botyanszki, J., Brodwin, M., Connolly, N., Dawson, K. S., Dey, A., Doi, M., Donahue, M., Deustua, S., Eisenhardt, P., Ellingson, E., Faccioli, L., Fadeyev, V., Fakhouri, H. K., Fruchter, A. S., Gilbank, D. G., Gladders, M. D., Goldhaber, G., Gonzalez, A. H., Goobar, A., Gude, A., Hattori, T., Hoekstra, H., Hsiao, E., Huang, X., Ihara, Y., Jee, M. J., Johnston, D., Kashikawa, N., Koester, B., Konishi, K., Kowalski, M., Linder, E. V., Lubin, L., Melbourne, J., Meyers, J., Morokuma, T., Munshi, F., Mullis, C., Oda, T., Panagia, N., Perlmutter, S., Postman, M., Pritchard, T., Rhodes, J., Ripoche, P., Rosati, P., Schlegel, D. J., Spadafora, A., Stanford, S. A., Stanishev, V., Stern, D., Strovink, M., Takanashi, N., Tokita, K., Wagner, M., Wang, L., Yasuda, N., Yee, H. K. C., & Supernova Cosmology Project, T. 2012, ApJ, 746, 85

Treu, T. 2010, ARA&A, 48, 87

Tripp, R., & Branch, D. 1999, ApJ, 525, 209

Umetsu, K., Medezinski, E., Nonino, M., Merten, J., Zitrin, A., Molino, A., Grillo, C., Carrasco, M., Donahue, M., Mahdavi, A., Coe, D., Postman, M., Koekemoer, A., Czakon,

N., Sayers, J., Mroczkowski, T., Golwala, S., Koch, P. M., Lin, K.-Y., Molnar, S. M., Rosati, P., Balestra, I., Mercurio, A., Scodeggio, M., Biviano, A., Anguita, T., Infante, L., Seidel, G., Sendra, I., Jouvel, S., Host, O., Lemze, D., Broadhurst, T., Meneghetti, M., Moustakas, L., Bartelmann, M., Benítez, N., Bouwens, R., Bradley, L., Ford, H., Jiménez-Teja, Y., Kelson, D., Lahav, O., Melchior, P., Moustakas, J., Ogaz, S., Seitz, S., & Zheng, W. 2012, ApJ, 755, 56

van den Heuvel, E. P. J., Bhattacharya, D., Nomoto, K., & Rappaport, S. A. 1992, A&A, 262, 97

van Dyk, S. D. 1992, AJ, 103, 1788

Voss, R., & Gilfanov, M. 2007, A&A, 468, 49

Wang, B., Meng, X., Chen, X., & Han, Z. 2009a, MNRAS, 395, 847

Wang, X., Filippenko, A. V., Ganeshalingam, M., Li, W., Silverman, J. M., Wang, L., Chornock, R., Foley, R. J., Gates, E. L., Macomber, B., Serduke, F. J. D., Steele, T. N., & Wong, D. S. 2009b, ApJ, 699, L139

Webbink, R. F. 1984, ApJ, 277, 355

Wheeler, J. C. 2012, ApJ, 758, 123

Wheeler, J. C., & Harkness, R. P. 1990, Reports on Progress in Physics, 53, 1467

Wheeler, J. C., & Pooley, D. 2013, ApJ, 762, 75

Whelan, J., & Iben, Jr., I. 1973, ApJ, 186, 1007

Williams, B. F., Garcia, M. R., Kong, A. K. H., Primini, F. A., King, A. R., Di Stefano, R., & Murray, S. S. 2004, ApJ, 609, 735

Wood-Vasey, W. M., Friedman, A. S., Bloom, J. S., Hicken, M., Modjaz, M., Kirshner, R. P., Starr, D. L., Blake, C. H., Falco, E. E., Szentgyorgyi, A. H., Challis, P., Blondin, S., Mandel, K. S., & Rest, A. 2008, ApJ, 689, 377

Wood-Vasey, W. M., Miknaitis, G., Stubbs, C. W., Jha, S., Riess, A. G., Garnavich, P. M., Kirshner, R. P., Aguilera, C., Becker, A. C., Blackman, J. W., Blondin, S., Challis, P., Clocchiatti, A., Conley, A., Covarrubias, R., Davis, T. M., Filippenko, A. V., Foley, R. J., Garg, A., Hicken, M., Krisciunas, K., Leibundgut, B., Li, W., Matheson, T., Miceli, A., Narayan, G., Pignata, G., Prieto, J. L., Rest, A., Salvo, M. E., Schmidt, B. P., Smith, R. C., Sollerman, J., Spyromilio, J., Tonry, J. L., Suntzeff, N. B., & Zenteno, A. 2007a, ApJ, 666, 694

—. 2007b, ApJ, 666, 694

Yoon, S.-C., & Langer, N. 2003, A&A, 412, L53

Zhelezniakov, V. V. 1981, Ap&SS, 77, 279

Zitrin, A., Broadhurst, T., Coe, D., Umetsu, K., Postman, M., Benítez, N., Meneghetti, M., Medezinski, E., Jouvel, S., Bradley, L., Koekemoer, A., Zheng, W., Ford, H., Merten, J., Kelson, D., Lahav, O., Lemze, D., Molino, A., Nonino, M., Donahue, M., Rosati, P., Van der Wel, A., Bartelmann, M., Bouwens, R., Graur, O., Graves, G., Host, O., Infante, L., Jha, S., Jimenez-Teja, Y., Lazkoz, R., Maoz, D., McCully, C., Melchior, P., Moustakas, L. A., Ogaz, S., Patel, B., Regoes, E., Riess, A., Rodney, S., & Seitz, S. 2011, ApJ, 742, 117

Zitrin, A., Broadhurst, T., Umetsu, K., Coe, D., Benítez, N., Ascaso, B., Bradley, L., Ford, H., Jee, J., Medezinski, E., Rephaeli, Y., & Zheng, W. 2009, MNRAS, 396, 1985

Zitrin, A., Meneghetti, M., Umetsu, K., Broadhurst, T., Bartelmann, M., Bouwens, R., Bradley, L., Carrasco, M., Coe, D., Ford, H., Kelson, D., Koekemoer, A. M., Medezinski, E., Moustakas, J., Moustakas, L. A., Nonino, M., Postman, M., Rosati, P., Seidel, G., Seitz, S., Sendra, I., Shu, X., Vega, J., & Zheng, W. 2013a, ApJ, 762, L30

Zitrin, A., Redlich, M., & Broadhurst, T. 2013b, ArXiv e-prints